A new platform for atom-light interactions on the nano-scale

HAMLYN, WILLIAM,JOSEPH

A new platform for atom-light interactions on the nano-scale

William J. Hamlyn

A thesis presented for the degree of

Doctor of Philosophy

Quantum Light and Matter Group

The University of Durham

United Kingdom

16th May 2020

A new platform for atom-light interactions on the nano-scale

William J. Hamlyn

Abstract

We present the design, fabrication, and operation of a new generation of thermal alkali vapour nano-cells. The nano-cells include internal structures with length scales $200 - 2000\,\mathrm{nm}$ created by laser lithography and reactive ion etching. The assembly process adopts optical contact bonding and glassblowing, avoiding the requirement for any bonding agents or adhesives. We demonstrate a novel method for characterising the size of the internal vapour nano-channels. The design allows for greater optical access and compatibility with high numerical aperture (NA=0.7) optics; we demonstrate this with total internal reflection fluorescence spectroscopy and high resolution imaging of the nano-channels. Additionally, we report for the first time on the photon statistics of light from a thin atomic ensemble. Finally, we discuss the diffusion of atoms inside confined geometries with a number of detection methods, and investigate options for controlling and manipulating the atomic density and its diffusion. In total, we present our new nano-cell design as a significant advancement of the field and propose its use in scalable atomic and quantum optics applications and technologies.

Supervisors: C. S. Adams and V. Sandoghdar

Acknowledgements

First and foremost my gratitude goes to Prof. Charles Adams and Prof. Vahid Sandoghdar, the PIs of the project. Most in the community would consider it a privilege to work with either one of these academics yet I had both. Through technical, pastoral, and financial support everything in this thesis is only possible because of you two. Thank you.

Next my thanks go to Prof. Ifan Hughes, whos warmth, enthusiasm, and encouragement were the driving force for me to start a PhD in the first place. Ifan supervised my summer internship in 2014 and it was during this 6 week placement that I became hooked and decided I wanted more, a PhD. I left that summer with a personally messaged and signed copy of his now infamous book "Measurements and their Uncertainties", and it will remain a prized possession of mine. My only regret is to have not been able to work more closely with Ifan during my PhD.

Jan Renger deserves individual recognition for advice and support in all forms and notably in micro-fabrication as noted in the thesis where necessary.

I was also fortunate to be surrounded by post-docs, who despite not being assigned to my experiment, offered me guidance and help whenever called upon. James, Dan, Dani, Josh, Andrew, Sofia, Chris, Teddy, and many others besides. I am ever so grateful to you all for helping to patch the holes in my knowledge.

To my fellow PhD students who are too numerous to name, you helped me stay sane (mostly) and I thank you for not only helping me to work, but also

helping me stop.

To my predecessor Kate Whittaker, I thank you for a great introduction to the project and it is from atop your shoulders I was able to achieve all that is here. And to my successor Tom Cutler, who brought a much needed fresh pair of eyes onto the project for my closing months and became a great sounding board for me to clarify final thesis ideas before writing.

Outside of work I was fortunate to have a great support network of friends, family, and fellow masochists in the rowing club. I owe great thanks to Grey College Rowing Club, as a member I endured countless hours of gruelling physical workouts which no doubt strengthened my mental resolve and served me well during the harder stages of my studies.

And, of course, my parents Anna and Nigel, who showed unlimited enthusiasm, love and support for me, despite being utterly unable to understand what on Earth I was actually doing.

Contents

Declaration

The work in this thesis is based on research carried out in the Quantum Light and Matter group, Department of Physics, University of Durham, England. No part of this thesis has been submitted elsewhere for any other degree or qualification, and it is the sole work of the author unless referenced to the contrary in the text.

List of Figures

Chapter 1

Introduction

Atomic physics is a field of study with both a long history and long future, perhaps due to the wide reaching umbrella term itself. There are numerous specialisations within the field and we explore three varied topics in this thesis, namely: spectroscopy, temporal correlations, and diffusion. The purpose of this thesis is to introduce a new design of alkali vapour nano-cell and demonstrate how it advances the study of atomic physics in multiple directions.

Atoms in confined spaces or near surfaces behave differently to those in bulk and effects like Dicke narrowing [1] and the Casimir-Polder force [2] have been documented long ago. Despite the age of the field, thermal vapours continue to be of interest with modern advanced modelling [3–5] allowing new technologies to emerge [6].

Micro-fabrication of alkali vapour cells is of interest to miniaturisation of atomic clocks [7, 8], definition of SI constants [9], and bio-medical applications like magnetoencephalography [10–12], and optical magnetometry [13] generally.

Further reduction in the length scales of confined vapours is of key import-

ance to this thesis and we claim that our design of nano-cells goes further than other examples [14–16]. The nano-cells produced in this thesis are an extension of a previous design from our group [17].

Modern atomic physics is often dominated by interest in the study of quantum physics and the production of quantum technologies. Numerous protocols have been proposed for quantum networks [18–20] and optical storage and quantum memories [21–25]. All these applications are predicated on the use of photons for transfer of information but with interactions mediated by atomic systems due to the atom-light coupling e.g. [26–30]. Of particular interest is the production of single photon sources from atomic systems, which has been demonstrated from collective excitation in hot [31] and cold [32] atoms. We will explore the quantum nature of light produced by atoms in our nano-cells, offering a new potential for a controllable single emitter array. Ongoing theoretical study in arrays of atomic dipoles [33–35] may be realised in our design of nano-cell.

Prior to the starting of this work, the state-of-the art in nano-cell technology belonged to the NAS in Armenia [15, 36]. Our early vapour experiments used Armenian nano-cells [37, 38], and inherited designs continue to be of use today [39]. The Armenian nano-cells began the study of nano-layer atomic vapours and still hold scientific value in the fact that the length scale can be varied down to effectively 0 nm, a feature that inspires new designs [16]. However, the fabrication method limits the versatility of the Armenian nano-cells particularly with respect to internal structure.

We propose that atomic vapour confined in nanometer scale structures, or near surfaces, offer further novel control of the atom-light interaction. Vapours in nano-cells have already been shown to demonstrate phenomena

not present in bulk vapours such as velocity selection [1, 40], energy level shifts [41–43], and possibly bound states [44]. Coupling of atoms to nano structures is ongoing in both cold atoms near optical nano-fibers [45–48] and in hollow core photonic crystal fibers [49], but also thermal vapours coupled to waveguides [50–54]. Devices have also been demonstrated with periodic structuring of atomic vapour by etched patterns in the containing walls [55]. We proceed further in this direction and explore the effect of novel internal geometry in our own design of alkali vapour nano-cells.

We use rubidium as our atom of choice in this thesis. The choice is largely historical and existing lasers of the correct wavelength ($\lambda = 780\,\mathrm{nm}$ for the D2 line) make changing species difficult. However, this old decision is a good one. In chapter 2 we shall see that the internal energy level structure contains convenient wavelengths for optical control. Rubidium also has a strong optical coupling on certain transitions and provides a significant vapour density at easily accessible temperatures in the lab. To quantify such claims we recall the scattering rate for a single atom:

$$\gamma = \frac{\Gamma}{2}\frac{S_0}{1 + S_0 + 4\Delta^2/\Gamma^2}, \tag{1.1}$$

where $S_0 = I/I_{\mathrm{sat}}$, Δ is the laser detuning, and $\Gamma \approx 2\pi \cdot 6\,\mathrm{MHz}$ [56] is the natural decay rate of the transition being probed. Thus at saturation intensity with a resonant laser a single atom may scatter more than a million photons per second, which is readily recorded by a photon counter with even a modest collection and detection efficiency. Additionally, for the rubidium D2 line $I_{sat} \approx 2\,\mathrm{mW\,cm^{-2}}$ and is easily achieved with low power lasers and modest focusing. It is promising then to use rubidium in the pursuit of isolating a single atom inside a nano-cell, one of the long term goals of this project. Additionally, the scattering rate of the rubidium D2 line enables laser locking

schemes to be realised with low power in room temperature bulk vapour cells (discussed in detail in the appendices).

Rubidium acts as a proof of principle atom in the studies presented in this work and changes of the atomic species or building materials of the nano-cells are discussed later. Throughout this work we will compare our findings to other similar experiments that operate with different alkali species and dielectric materials, but the fundamentals are universal and many phenomena are common across all alkali species.

Figure 1.1 shows the vapour pressure vs. temperature curve for rubidium. We see that the vapour density varies by many orders of magnitude over a modest range of temperatures. By extension, the number of atoms in a fixed volume can then also be tuned over a wide range by control of the temperature. In this thesis we argue the case that we can produce a sufficiently small internal geometry in our vapour cell that we may isolate a single atom of rubidium in the vapour phase. Additionally, we see that the mean inter-atomic spacing can be varied to be greater than or less than the probe wavelength (780 nm in most cases) which can cause the appearance of collective effects [57].

Rubidium has a melting point of 39 °C, although the phase change of condensed rubidium from solid to liquid is typically not noticed as we study the vapour phase. However, chapter 3 discusses an instance where the liquid form of rubidium is necessary for loading the nano-cell reservoir.

The study of the mechanical motion of atoms on, and near, surfaces is also of long historical interest [59]. The processes by which atoms spontaneously diffuse inside confined geometries [60–62] is of great interest for loading [63] and curing* [64]. Precise control over the diffusion process and of desorption

*Once an alkali vapour cell is manufactured, it is typical that a waiting time is needed

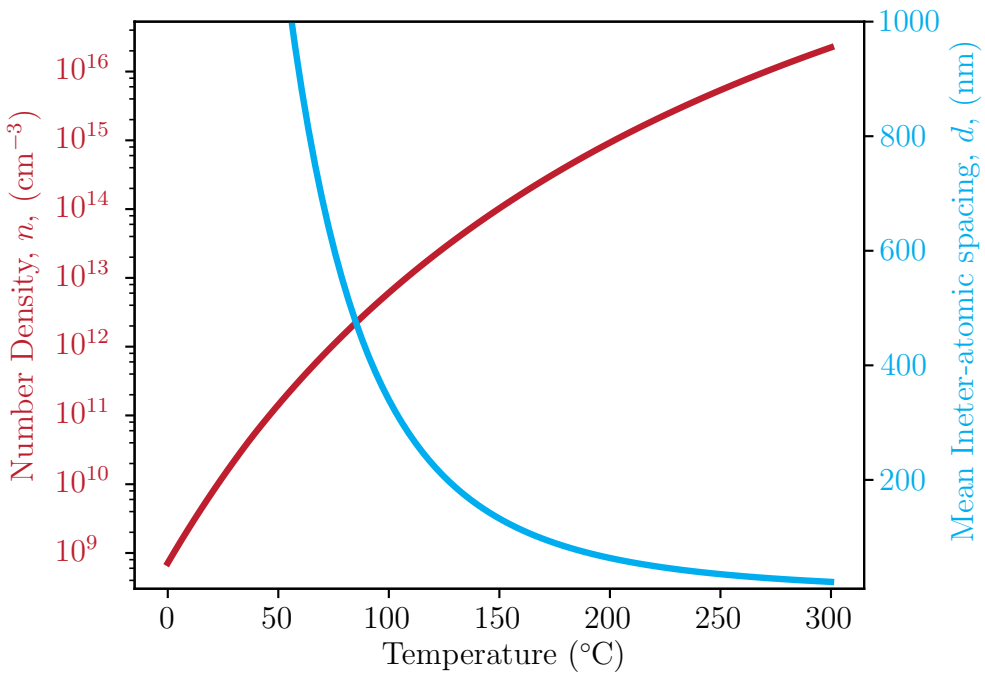

Figure 1.1: Rubidium number density [58] (red line) and the mean inter-atomic spacing (cyan line) as a function of the vapour temperature. Inter-atomic spacing is calculated as the radius of the mean spherical volume per particle, $d = (4\pi n/3)^{-1/3}$, where n is the number density. Note: the vapour pressure curve shown here assumes an equilibrated system in the steady state.

of atoms from surfaces has been made possible with light induced atomic desorption (LIAD). Quantitative LIAD studies [65] demonstrate that sufficient yields could replace the need for heating in thermal vapour based technologies. A working optical isolator based on this principle is shown by Talker et al. [66].

1.1 Thesis structure

The remainder of this thesis will have the following structure:

to equally coat the internal surfaces of the vapour cell and to reach equilibrium with the vapour phase. Often this process is accelerated by heating.

- Chapter 2 introduces some foundation theory and justifies the choice of atomic species. As the experimental studies in this thesis are diverse, more specific theory topics are introduced in the relevant chapters as needed.
- Chapter 3 discusses in detail the design, fabrication, and operation of the nano-cells used in this thesis. We also consider possible future enhancements to the nano-cell design.
- Chapter 4 explores the spectral response of atoms in the nano-cell using the method of total internal reflection fluorescence. We investigate the angular dependence of the spectra and demonstrate our enhanced sensitivity to atom-surface effects.
- Chapter 5 looks at the temporal correlations of light scattered by atomic ensembles within the nano-cell.
- Chapter 6 contains theoretical modelling and experimental results of the diffusion of atoms within nanometer-scale cavities. We also include a preliminary look at the control and exploitation of the atomic density using light induced atomic desorption.
- Chapter 7 concludes this thesis and proposes new directions for each of the themes explored in earlier chapters. Additionally, we propose a combination of all methods of this thesis to create a switchable array of single atoms in thermal vapour.

1.2 Publications arising from this work

The following publications are currently in preparation:

- *High NA imaging of atoms in a nano-structured cavity*, William J. Hamlyn, Tom Cutler, Danielle Pizzey, Ifan Hughes, Jan Renger, Vahid Sandoghdar and Charles Adams (in preparation)

- *Photon statistics of atomic fluorescence emitted by a nano-scale vapour layer*, Sofia Ribeiro, William J. Hamlyn, Tom Cutler, Simon Gardiner, Danielle Pizzey, Ifan Hughes, Jan Renger, Vahid Sandoghdar and Charles Adams (in preparation)

Chapter 2

Atom-light interaction in confined geometries

The primary purpose of this thesis is to demonstrate the multiple different phenomena available for study due to our nano-cell design. As such, the physics explored in this work is varied and plentiful. We present chapters on spectroscopy, photon statistics, and atomic diffusion. Each investigation proves the versatility of our nano-cell design by the very nature of their being distinct. Because of this, the theoretical framework needed to interpret each result varies depending on the containing chapter. Thus we will use this chapter to introduce only the common themes through this thesis, the rubidium atom and some considerations specific to nano-cells, and leave the relevant more specialised theory work to each chapter as it is needed.

2.1 Particle or wave?

We will begin by getting one thing out of the way, or rather avoiding it all together. Light can be well described by electromagnetic waves in many

instances. However, the picture of discrete light quanta, termed photons, is very much required for a correct quantum mechanical description of light. In this thesis we will see varied experiments, data, and models where the choice of the wave nature or particle nature of light changes depending on the setting. We do not address the controversy directly nor seek to conclude that one model is superior to another. Mostly, the choice is made for convenience and clarity for the reader. Do not be alarmed to discover that one chapter discusses laser fields and waves and the next discusses photon counting.

The same can very well be said for the electron of the atom which is the quantum system we probe with our light. The electron can be described as a particle, or by its quantum mechanical wavefunction. Although not strictly equivalent as the wavefunction is a probability distribution, the properties of wave mechanics can also apply to the electron. However, the case is simplified here as the atoms are never (intentionally) ionised and so the atom as a whole is considered as a system with internal states that are driven by an external light field (or incident photon).

2.2 Ideal quantum systems

In general the 'ideal' case is sought by experimentalists of all disciplines. We use the term to describe a system that is free from the complexities of true reality*. Understandably, using ideal models to represent real systems often leads to disparity. However, progress in understanding can be made by exploring the areas of parameter space in which they do not agree. We begin with a most simple model, add layers of known and tested extra complexity

*multiple competing effects, imperfect equipment, limitations in time, energy, or funds, and always noise.

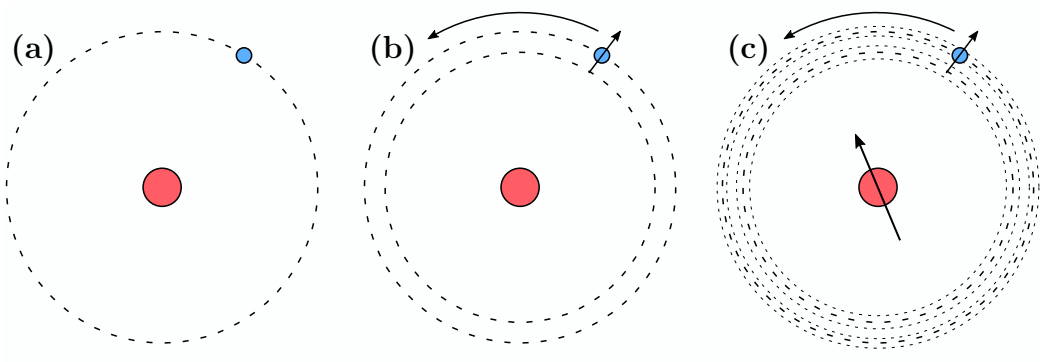

Figure 2.1: Schematic depictions of the hydrogen atom to symbolise the energy level structure as more considerations are added. **(a)** So called gross structure, an electron (blue circle) in 'orbit' around a proton (red circle). **(b)** Inclusion of relativity, spin-orbit coupling, and the Darwin term creates fine structure in the energy levels. **(c)** Inclusion of the nuclear magnetic moment produces hyperfine structure.

until we have a model that correctly explains all known phenomena. If this model disagrees with our data we know where to scrutinise our knowledge, or lack thereof. The iterative process of collecting data and modelling it to make further predictions drives the direction of investigation.

2.2.1 Multi-level atoms

We will now construct a theoretical atom from tried and tested theory that is routinely used in atomic physics experiments and simulations. We will introduce in turn the relevant quantum numbers required to describe the internal energy level structure of rubidium. However, for ease, we start with the most basic atom; hydrogen.

Figure 2.1 shows a schematic depiction of the idealised hydrogen atom as extra terms and considerations are added to the mathematical solution. One must abandon classical electromagnetism even in the first case (figure 2.1a) as stable solution for a charged particle to orbit another exists. We will also

dispense with the term 'orbit' as it is misleading. Instead it is more correct to say that the electron is in a bound state somewhere in the vicinity of the nucleus*. Sadly, the adopted convention in the community is to refer to these bound states as orbitals although I think we can blame the chemists for that, and the author (and most other physicists) will avoid the term where possible.

Where classical electromagnetism fails to correctly predict stationary states for the electron-proton system, we can instead use the time independent Schrödinger equation:

$$\hat{H}\left|\Psi\right\rangle = E\left|\Psi\right\rangle, \tag{2.1}$$

where $|\Psi\rangle$ is the electron wavefunction, E is the energy of the bound state, and $\hat{H}$ is the Hamiltonian of the form:

$$\hat{H} = \frac{\hat{p}^2}{2m} + V(r). \tag{2.2}$$

The Hamiltonian consists of two terms that describe the kinetic and potential energy of the electron respectively. Given the spherical symmetry of the potential, solving the Schrödinger equation in spherical polar coordinates produces mathematically convenient and separable differential equations.

A detailed derivation exists in any respectable quantum mechanics textbook (e.g. [67]) and for the sake of the trees it will not be reproduced here. The main conclusion is that the solutions are discrete stationary states of finite energy which follow:

$$E_n = \frac{-Z^2}{2n^2}E_h, \qquad n = 1, 2, 3, ... \tag{2.3}$$

where Z is the atomic number (hence eZ is the nuclear charge) and E_h is the atomic unit of energy:

$$E_h = m_e\left[\frac{e^2}{4\pi\epsilon_0\hbar}\right]^2, \tag{2.4}$$

*Probably.

with: m_e electron mass, e elementary charge, ϵ_0 permittivity of free space. We have now encountered our first quantum number n which is termed the principle quantum number*. These discrete levels form the gross structure of the atoms energy level landscape.

The azimuthal quantum number, L, describes the orbital angular momentum of the electron wavefuntion and is obtained from higher degree spherical harmonic solutions to the Schrödinger equation (for a spherical potential). L can take the value of any positive integer including 0 with the first few values, $L = 0, 1, 2, 3, ...$ denoting the familiar electron orbitals s, p, d, f, ... respectively.

The intrinsic properties of the electron provides another quantum number, S, the spin angular momentum. Coupling of the spin and orbital angular momentum we obtain the total angular momentum number, $J = L + S$. Where J can take any value in the set,

$$J \in \Big[\ |L - S|,\ |L - S| + 1,\ ...,\ |L + S| - 1,\ |L + S|\ \Big]. \tag{2.5}$$

Additionally, relativistic corrections for the kinetic energy of the electron and the Darwin term (positional uncertainty from the Heisenberg principle), must be included. The result is that the gross structure levels are split into sublevels known as fine structure, each labelled by the possible values for J.

Lastly, the fine structure levels are further divided by considering the magnetic moment of the nucleus, which arises due to the nuclear spin. We denote the nuclear spin I. The nuclear spin couples to the total angular momentum

*The quantum number n should not be confused with n the atomic vapour density also used in this thesis. The use of these numbers is totally different and so context should make obvious which is being talked about. However, do be aware that n appears more than once in this thesis.

of the electron J to make the quantum number F, again an integer, where:

$$|I - J| \leq F \leq |I + J|. \tag{2.6}$$

The multiple values of F label the hyperfine levels.

Within the hyperfine levels there exist multiple magnetic sub-levels each denoted by the integer m_f where:

$$-F \leq m_f \leq F. \tag{2.7}$$

The separate m_f levels (also called Zeeman sub-levels) are degenerate for each value of F in the absence of a magnetic field as is the case for the entirety of this thesis. However, acknowledging the existence of these levels is necessary to explain the process of optical pumping used to stabilise our laser systems. This is explored in more detail in appendix A.

With these quantum numbers we can uniquely identify all of the internal states of the atom, using the term symbol:

$$n\ ^{(2S+1)}L_J. \tag{2.8}$$

The $(2S + 1)$ term is usually omitted in monovalent atomic systems as it is implicit from the spin $1/2$ electron and the orbital quantum number L. The F number is then listed after, hence an example term symbol would be: $5P_{3/2}$, $F = 2$.

2.2.2 Rubidium

The quantum picture of the atom described in the previous section is general to all atoms, and having endorsed the benefits of simplicity one might ask: why not use hydrogen for these experiments? However, there are many reasons to opt for rubidium as the atom of choice in our experiments generally.

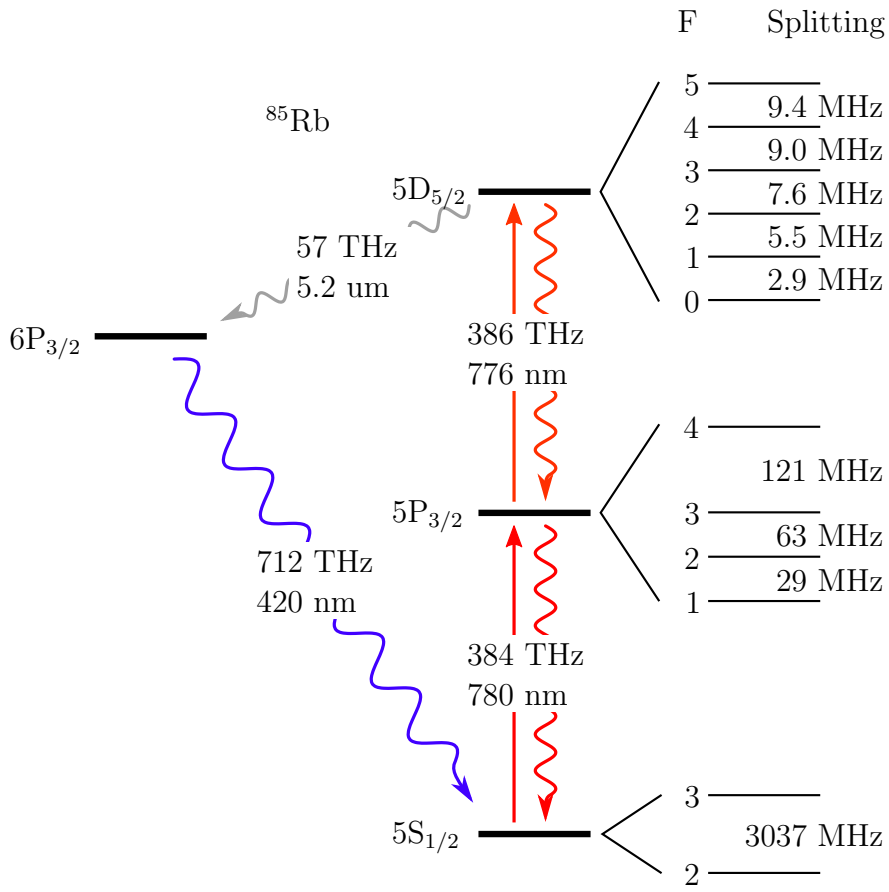

Figure 2.2: Partial energy level diagram for ^{85}Rb showing the relevant transitions used in this thesis. Splittings and frequencies courtesy of [3, 69].

Rubidium naturally exists as a monatomic gas. The ground state transition (780 nm) is a wavelength easily produced by cheap laser technology* and manipulated by common optical components. The high vapour pressure at room temperature combined with a strong transition strength make detection (and laser locking etc.) easy. The fine, hyperfine, and Zeeman level structure make optical pumping, cooling, and trapping available. It is no surprise then that with such great optical control, rubidium became the first atomic species with which a BEC was realised [68].

Figures 2.2 & 2.3 show the relevant portion of the energy level structure of

*CD players operate at 780 nm.

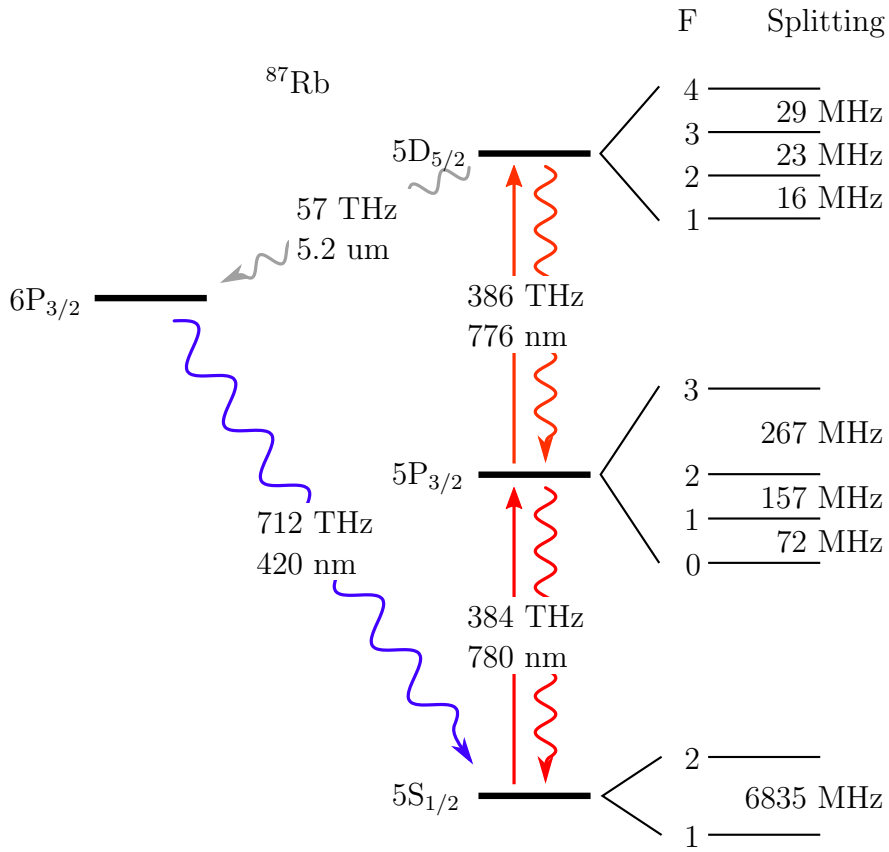

Figure 2.3: Partial energy level diagram for ^{87}Rb showing the relevant transitions used in this thesis. Splittings and frequencies found in ref. [3, 69]. The lower nuclear spin of ^{87}Rb (I=3/2) results in fewer hyperfine levels in the $5D_{5/2}$ state. There is also an isotope shift that displaces the weighted centre of the $5P_{3/2}$ state by -77 MHz [3] and the $5D_{5/2}$ state by -163 MHz [70] relative to ^{85}Rb.

rubidium 85 and 87 respectively, as used in this thesis. We have two sets of energy levels to represent the two isotopes of rubidium that make up the naturally occurring mixture (72% ^{85}Rb, 28% ^{87}Rb) with which our nano-cells are filled. It is the differing nuclear spin of the two isotopes ($I = 5/2$ for ^{85}Rb, and $I = 3/2$ for ^{87}Rb), that creates the two unique energy level structures.

2.3 Lineshapes

So far, our derivation of the energy level structure of the rubidium atom suggests that the levels exist at well defined discrete energies. However, attempting to observe these spectral lines one will soon discover a finite linewidth. The profile of the resonance line can tell a great deal about the atomic system. The finite lifetime of an excited state introduces an exponential decay term in the time domain. By Fourier transform, this becomes a Lorentzian lineshape often called the 'natural' lineshape with analytic form:

$$L(\Delta) = \frac{1}{2\pi} \frac{\Gamma}{\Delta^2 + (1/2\ \Gamma)^2}. \tag{2.9}$$

Where Δ is the detuning from resonance, and Γ is the decay rate of the transition, and also is the full width half maximum (FWHM) of the Lorentzian lineshape. For rubidium 5P state $\Gamma_{5\mathrm{P}} = 2\pi \cdot 6\,\mathrm{MHz}$ [56], and for the 5D state $\Gamma_{5\mathrm{D}} \approx 2\pi \cdot 0.6\,\mathrm{MHz}$ [71]. One might expect to easily resolve the lines individually with a narrow line laser, however, Doppler broadening makes this non-trivial.

The Doppler effect plays a significant role in the overall lineshape when probing a thermal ensemble of atoms. Figure 2.4 shows how the Voigt lineshape emerges as the overall spectral profile for a thermal ensemble of atoms. For each atom, the transition line centre is shifted due to its velocity relative to the laser field. Integrating over all atom velocities, the result is a broadened lineshape that in the limit of large atom number tends towards the Voigt function given by the convolution of a Lorentzian and a Gaussian:

$$\begin{aligned} V(\omega, \Gamma, \sigma) &= \int_{-\infty}^{\infty} L(\omega - \omega', \Gamma) G(\omega', \sigma)\ d\omega' \\ &\equiv L(\omega, \Gamma) * G(\omega, \sigma). \end{aligned} \tag{2.10}$$

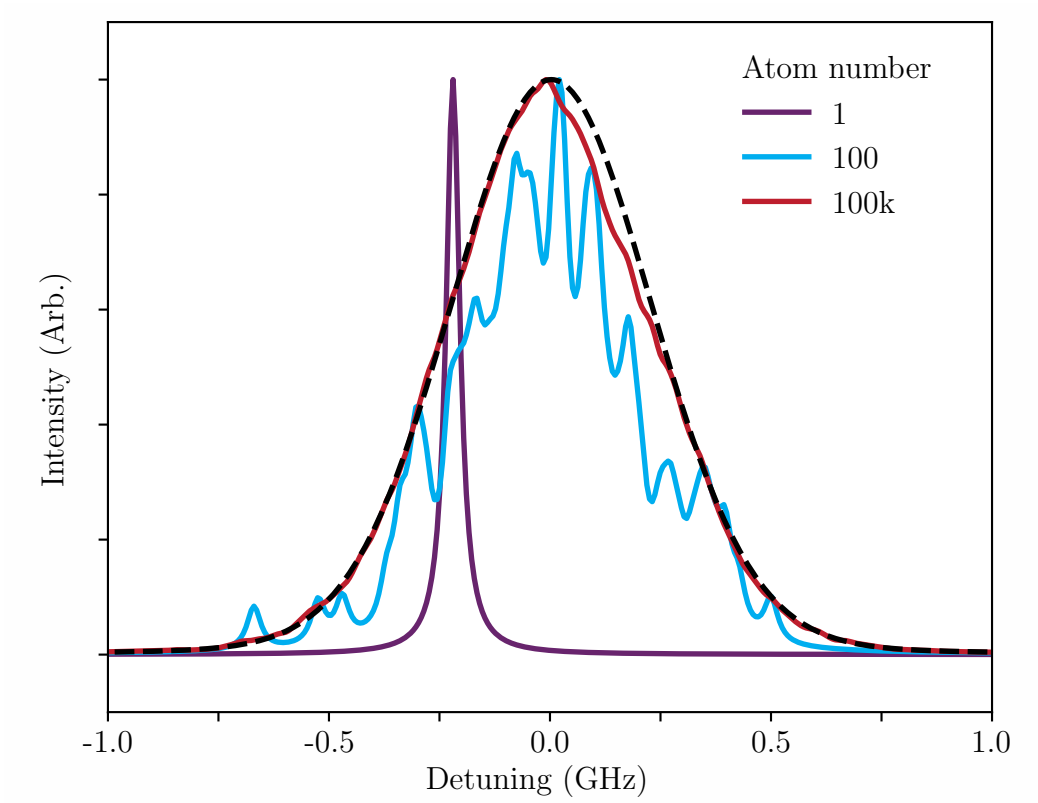

Figure 2.4: Simulation showing the emergence of the Voigt lineshape in a thermal ensemble of atoms. A single atom (purple line) has a Lorentzian lineshape with line centre shifted due to the Doppler effect. A sum of 100 (cyan line) and 100,000 (red line) atoms each with a velocity randomly taken from a Maxwell-Boltzmann distribution, tends towards a Voigt profile (black dashed line).

ω' is the Doppler shift for a particular velocity class of atoms, hence the Gaussian velocity distribution of atoms is represented in the frequency basis. Note that we calculate the Doppler shift of each atom, i, in the simulation by:

$$\omega'_i = \frac{-v_i\ \omega_0}{c}, \tag{2.11}$$

where v_i is the velocity of the atom in the direction of the light field k-vector, c the speed of light, and ω_0 the centre frequency of the transition being probed.

Using the convolution is more accurate and faster than a Monte-Carlo approach, the depiction here was made to provide an intuitive explanation.

Furthermore, additional broadening effects can be included into the Voigt profile by modifying the parameters Γ and σ. Increases in the Lorentzian and Gaussian widths are caused by homogeneous and inhomogeneous broadening mechanisms respectively.

Alternatively, one can describe the Doppler broadening of an ensemble by considering the temperature. The temperature is a measure of the average kinetic energy of the atoms and hence the velocity distribution tells us of the Doppler width, $\Delta f_{\text{Doppler}}$, of the ensemble by:

$$\Delta f_{\text{Doppler}} = \frac{2\ f_0}{c}\sqrt{2\ \ln 2\ \frac{k_{\text{B}}T}{m}}, \tag{2.12}$$

Where f_0 is the centre frequency of the optical transition, T is the temperature, and m is the mass of the atoms.

The temperature ranges explored in this thesis ($20 - 200\,°\text{C}$) result in a Doppler width of $\Delta_{\text{Doppler}} = 500 - 650\,\text{MHz}$ and hence the hyperfine splitting of the ground state is well resolved, but the excited states are not (see for example figure A.2, or 4.2). The splitting of the $5\text{P}_{3/2}$ hyperfine states being less than the Doppler width causes the appearance of the cross-over resonances in saturated absorption spectroscopy (see appendix A).

2.4 Single atoms

The goal of this thesis is to demonstrate that our unique nano-cell design represents a significant step forward in the study of fundamental physics and the creation of applied devices. One branch of this tree is to isolate a single atom and to have control over the interactions of that atom with external light fields (optical coupling). A single atom is a common goal of many

atomic physics experiments and has been realised numerous times in cold atom experiments. The reason a single atom is of interest is that it is a single quantum emitter that is capable of coupling to a single photon and preserving encoded quantum information carried by that photon. Single atoms can also act as single photon sources. When an atom decays from an excited state it releases a single quantum unit of light. This is different from a mean photon number of 1 and has important consequences when the photon is used in quantum information processing operations. This topic is covered in more detail in chapter 5 where the quantum picture of light and atoms is required to understand the experimental data.

2.5 Many atoms

When many atoms are addressed simultaneously the physics can change in non-linear ways. That is to say that the response of N atoms is not simply the same response as a single atom made N times stronger. Collective effects mean that the atoms can now interact with one another via the dipole-dipole interaction which opens a channel of behaviour that is not available to a lone atom. The density of an ensemble means that atom-atom collisions may also play a role (although this occurs more significantly at temperatures beyond those explored in this thesis).

2.6 Confined atoms

Significant changes to the lineshapes occur when thermal vapours are confined to nano-cells. Most of the data presented in this thesis is taken from a

2D environment*, which significantly changes the environment of the atoms. Throughout this thesis, we adopt the convention that in a 2D environment it is the z axis that is constrained.

Figure 2.5 shows an atom in a nano-cell to help depict the process by which some nano-cell specific phenomena occur. In a 2D environment, the atomic trajectories are limited significantly by the presence of the near walls. Given the mean thermal speed of the atoms of $\sim 250\,\mathrm{m\,s^{-1}}$, the transit time of an atom from one surface to the other is $\sim 3\,\mathrm{ns}$. This is much shorter than the 27 ns [56] lifetime of the 5P state and substantially shorter than the 239 ns [71] lifetime of the 5D state. As a result, the atom effectively experiences a pulsed excitation which increases the perceived laser bandwidth. Additionally, atoms travelling parallel to the laser beam that have the most significant impact on Doppler broadening are less likely to absorb and fluoresce photons due to the short interaction time window. Hence the overall Doppler broadening is reduced. The transit time in x and y is limited by the spot size of the probing laser or collection volume in instances of fluorescence. Typically this is of the order of 10's of µm and does not inhibit the natural decay rate.

The nano-cell is constructed from fused silica which is a dielectric. The excited atomic dipole induces a mirror charge in the surface provided the atom is sufficiently close. We will see in chapter 4 that this van der Waals interaction between the atom and the wall causes considerable redshift to the atom energy levels, specifically the 5D state, resulting in a strong asymmetry in the spectral features. The negative potential energy landscape experienced by the excited atom near the dielectric surface also manifests as an attractive force for the atom onto the wall.

*We use the term 2D to mean that one of the length scales of confinement is of the order of the wavelength of the probing light field.

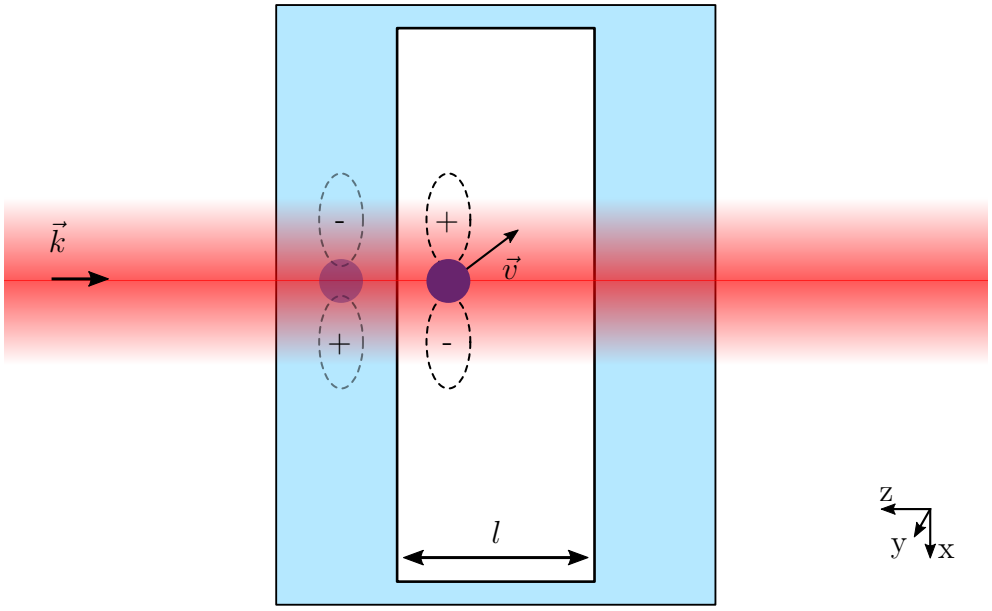

Figure 2.5: Schematic diagram of an atom in a nano-cell highlighting the appearance of some key phenomena. The dielectric material of the nano-cell enables the appearance of mirror charges, creating an attractive van der Waals interaction. Atomic velocity produces a transit time shorter than the excited state lifetime due to the layer thickness $l = 400 - 2000\,\text{nm}$. The Doppler broadening term $\vec{k} \cdot \vec{v}$ (equivalent to equation 2.11) is suppressed as atoms travelling parallel to the beam axis collide with the inner surfaces of the vapour cell and thus contribute less to the overall spectral response.

Having introduced some standard atomic physics and some considerations specific to the nano-cell, the next chapter will discuss the nano-cell design that enables us access to study and control these phenomena. In the later chapters 4, 5, & 6, we present our experimental data. Due to the variety of subjects covered, more specific theory topics are introduced as needed.

Chapter 3

Nano-cell fabrication

3.1 Introduction

Manipulation of the environment of an atomic system has presented a wide range of physics studies, for example, in photonic crystal hollow-core optical fibers [49, 63, 72], atoms in close proximity to nano-fibers [45, 48, 73], and drives progress in applied fields such as miniaturisation and production [7, 8]. A number of applications have also been born of atomic vapours in small geometries [10–12, 74–76].

Sub-wavelength* scale atomic vapours have also been produced and studied [15, 16]. The tiny length scale of these nano-cells makes it possible to interrogate high density vapours [37, 77] and atoms in close proximity to surfaces [41–43]. Historically the nano-cells produced in the NAS, Armenia, have been the workhorse for thin thermal vapour physics. To this day their cells are used due to certain unique qualities, mainly their maximum operating temperature (350 °C or more is not uncommon) and extremely short length

*Typically the wavelength associated with the atomic transition being probed. For the majority of this thesis that is the rubidium D2 line at 780 nm.

scales ($\sim$ 10 nm [57]). Recently, thin alkali vapour cells have been produced with a thickness that varies from a few microns continuously down to 0 nm over a few centimetres [16] offering fine control of the thickness of the vapour being probed.

In addition to the length scale of the atomic vapour, the spatial extent of the probing light fields can be altered to deliver new phenomena and optical control over the system. The choice of the atomic environment and how light interacts with the system determines the information that is ultimately yielded to the experimenter.

We have taken influence from experiments with guided light modes and those with highly confined atoms to move towards a platform that could offer both. Although guided light modes do not currently exist within our nano-cells this option is compatible with our current fabrication process, and we have designed a nano-cell with more flexible optical access than has been demonstrated previously. To enable such optical access it was necessary to produce our own nano-cell design and fabrication process (an extension of reference [17]). The data presented in this thesis was made accessible by the bespoke design of our own nano-cells.

3.2 Design

Our nano-cells bring significant advancement, not only in operation but also during the production phase. Here we describe the main features of the nano-cell. Later, in this chapter we describe explicitly the fabrication process and the advantages therein.

3.2.1 The nano-cell

Figure 3.1 shows the core design of the nano-cells used in this thesis. The nano-cell design has undergone some evolution and improvement through the course of the work but the fundamental components and assembly are consistent across all generations of nano-cells used in this work. Changes to the etched micro-patterns represent the most significant change to the design and this is discussed in further detail later in this chapter.

Our nano-cells are assembled from three distinct parts that we refer to as the cover slide, the block, and the reservoir (see figure 3.1). The block is a fused silica cuboid of dimensions 10 mm × 20 mm × 30 mm with an internal 5 mm diameter tube. The internal tube acts as a conduit for rubidium vapour to travel from the reservoir to the micro-cavities once the cell is complete. The cover slide is a fused silica panel of dimensions 20 mm × 30 mm × 0.5 mm into which we write micro- and nano-scale structures with direct write laser lithography and reactive ion etching respectively. The reservoir is a section of borosilicate glass tube that houses a macroscopic deposit of rubidium that supplies atomic vapour into the nano-channels.

3.2.2 Optical access

For any atomic physics experiment thought is invested into how light enters the system, interacts with the atoms, and how outgoing light is collected. It is in this area that our nano-cells offer a wide range of experimental options for excitation and detection schemes, including the use of high numerical aperture (NA) optics which is not typical in the field of thermal vapour physics. The block is polished on all four perimeter faces enabling light to be coupled

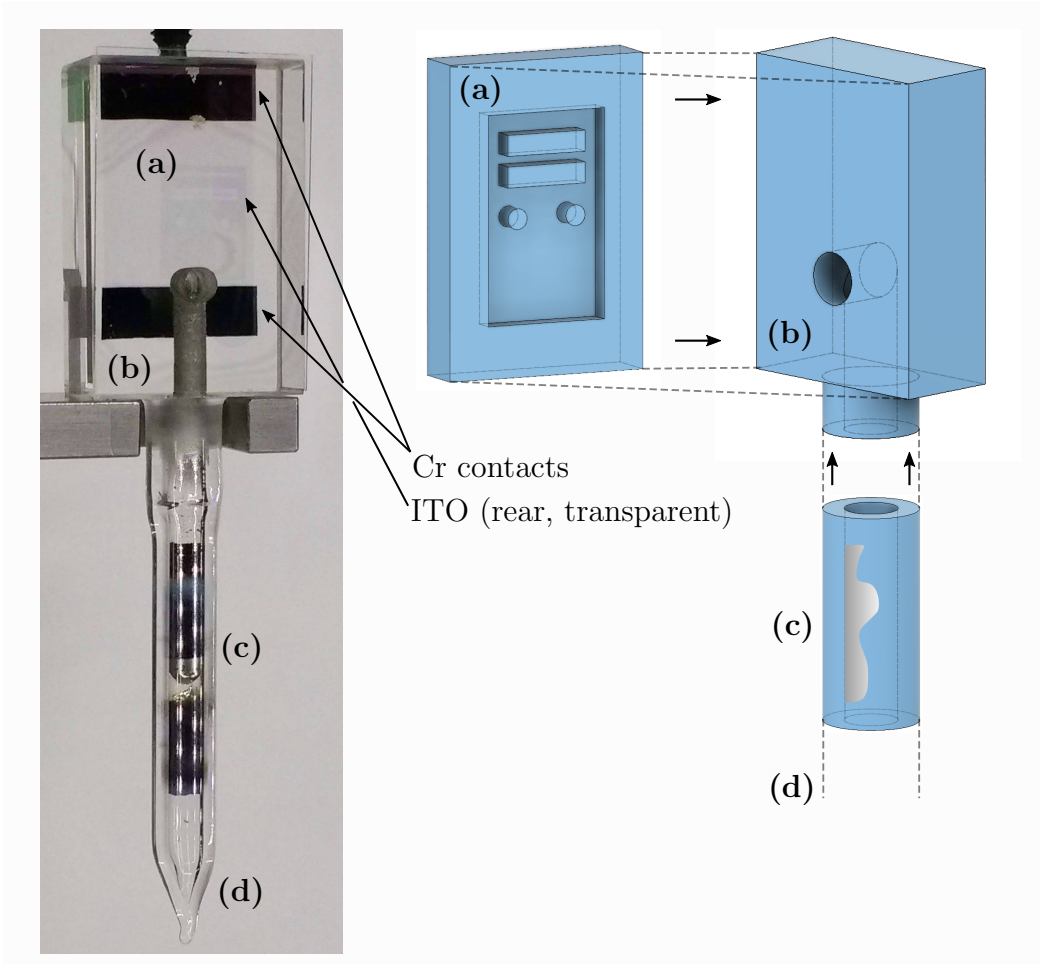

Figure 3.1: Photograph (left, approximately 150% of life size when printed) and exploded schematic diagram (right) showing a completed nano-cell and the key components of the nano-cell respectively. **(a)** Etched cover slide **(b)** Glass block with internal tubing **(c)** Reservoir with condensed rubidium added after bonding and evacuation **(d)** Sealed end after evacuation and loading. The full length of the finished nano-cell is $\sim 80\,\mathrm{mm}$. The nano-cell depicted in the photo has an ITO patch applied to the back (transparent, hence not visible) and chromium contacts (seen as two dark horizontal rectangles). The image was taken with a diffuse back light and hence the interference fringes caused by the cavity are not very pronounced (see the reflection image in figure 3.2 for contrast). A detailed description of the assembly process can be found in the text.

into and out of the nano-cell from almost any direction. We will see in the following chapters how various optical access schemes are employed, and the benefits that they provide for studying a nano-scale thermal vapour system.

3.2.3 Internal structure

Central to the work of this thesis and the true novelty of our nano-cell design is the inclusion of nano-scale structures. Sub-wavelength scale 2D vapour layers have allowed new physical regimes to be studied. Atomic ensembles exhibit new and useful properties because of their confinement. To advance this field of study we form near-arbitrary structures that can be filled with atomic vapour.

Figure 3.2 depicts the internal structure of the nano-cell and a photograph clearly shows the nano-cavities. Our nano-cells have internal structures of 2D vapour layers, 1D channels and 0D 'pockets' for the vapour to enter. The typical length scales of theses structures is approximately 2 µm-400 nm. Due to their size, the channels cause an interference with visible light which is evidenced by the colours observed when reflecting white light (figure 3.2b). The appearance of these colours is exploited (see 3.4.1.1) to determine the cavity length in situ.

3.2.4 Mounting

By using the rectangular glass block as the core element we can produce a nano-cell that is mechanically robust and can be mounted by clamping to the regular faces of the block (see Figure 3.1). We mount to the faces that are not required for optical access so as to maintain the available access for in-going

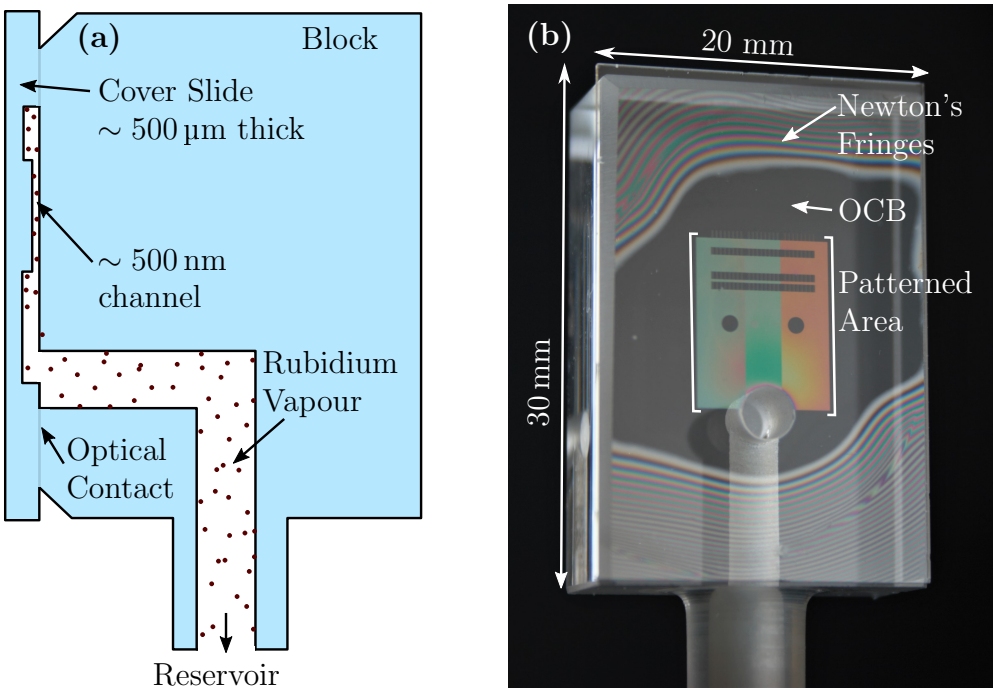

Figure 3.2: **(a)** Schematic cross-section side view of the internal structure of the nano-cell. After bonding the etched cover slide onto the face of the block, the etched nano-channels become cavities for the atomic vapour to occupy. The atomic vapour is supplied from the reservoir via the internal tube of the block. **(b)** Photograph of a completed nano-cell taken with a reflected white light source. The coloured interference fringes indicate the cavities between the cover slide and the block. The optical contact bond (OCB) is evidenced as an absence of fringes and here we see that the OCB totally encloses the patterned area ensuring a vacuum seal. The height and width of the block are labelled, the depth is 10 mm.

and out-going light coupling. Mounting to the glass block directly to a translation stage (as opposed to mounting inside an oven, and then a stage) give increased mechanical stability. To collect light from sub-wavelength structures, we require long integration times and it is therefore critical that the nano-cell does not move by more than the structure size during this integration.

Furthermore, the absence of a cell oven means that high-NA (short working distance) optics can be employed. Additionally the optics in close proximity to

the nano-cell less likely to be heated by the oven. A more detailed evaluation of heating techniques is presented in section 3.4.2.

3.2.5 Materials

A common concern for handling and use of alkali vapours is the high chemical reactivity, a property that is exacerbated by heating. Alkali metals, like rubidium, will self-ignite in open atmosphere and hence most vapour cells are evacuated with others being filled with an inert atmosphere. However, the alkali vapours are sufficiently corrosive that they will also react with the glass of the cell they are contained within. This influences the choice of material when high temperature operation is needed and is the reason for the Armenian nano-cells (e.g. [15]) (made from sapphire) possessing a relatively high maximum operating temperature.

However, machining and bonding of sapphire is difficult as the hardness of the glass also means that conventional glassblowing techniques cannot be employed. We have selected fused silica as the material of choice for the nano-cell due to the excellent optical properties (high transmission for a broad wavelength range), the wide range of machining options that can be employed, and for its compatibility with conventional glassblowing. Hot rubidium vapour will react with the fused silica at temperatures exceeding $\sim 200\,^{\circ}\mathrm{C}$, but we accept this compromise as it is low temperature operation (ultimately room temperature) that we seek.

Rubidium is loaded into the nano-cell via traditional glassblowing whereby a borosilicate glass manifold is attached to the nano-cell. Borosilicate glass is used for convenience, more detail is provided later in section 3.3.4.

3.3 Fabrication methods

We employ a range of machining, bonding, and finishing techniques to produce our nano-cells. The final product is glue-free and all-glass, offering unique advantages and enabling advanced study of atomic vapour physics. We believe our production scheme offers real progress towards applied devices, as our methods are also compatible with integrated photonic techniques e.g. waveguide growth.

3.3.1 Milling and polishing

The core element of the nano-cell is the glass block, a single piece of fused silica of dimensions 10 mm × 20 mm × 30 mm. The block is then ultrasonically milled to create an internal L-shaped tube from the bottom side to the front face that will later act as a conduit for rubidium vapour between the nano-structures and the rubidium reservoir. The glass block is optically polished on four sides to enable light to be delivered and collected through any of the faces. This also facilitates the method of optical contact bonding (see 3.3.3), which a key part of the assembly process. The milling and polishing was performed by a third party supplier, Newcastle Optical.

3.3.2 Etching

To create micro- and nano-structures for the vapour to occupy, we create a patterned cover slide. The cover slide is a fused silica panel measuring 20 mm × 30 mm × 0.5 mm into which we write micro- and nano-scale patterns in photoresist via direct-write laser lithography. We then etch the patterns into

the glass substrate by reactive ion etching. The etching was performed by our collaborative technician Jan Renger at the Max Planck Institute in Erlangen, Germany.

Figure 3.3 shows a microscope image of part of a cover slide after the etching process is complete. We are able to pattern near-arbitrary shapes and are also able to select the depth of the etched pattern. We produce batches of cover slides for redundancy. Multiple new design versions have been completed to an operational state during the course of this investigation. This stands as a testament to the flexibility, scalability, and reliability of our fabrication method.

3.3.3 Bonding

To create a sealed environment for the vapour, the etched cover slide must be bonded to the glass block. The etched patterns form cavities against the front face of the glass block. Provided that the glass block and cover slide are sufficiently polished and clean, an optical contact bond (OCB) can be made whereby the van der Waals interaction between the two glass pieces bonds them together. In practice, an OCB does not spontaneously form. We assemble the nano-cells in an open air environment and hence a thin layer of air forms between the two glass pieces, evidenced by visible coloured fringes. In this state, the nano-channels appear as a discontinuity in the fringes, a useful phenomenon for positioning the cover slide correctly such that the internal tube of the glass block meets the nano-channels to later provide a vapour supply.

Once positioned, the cover slide can be pressed against the glass block to expel the layer of air keeping them apart. An OCB is formed and evidenced by an

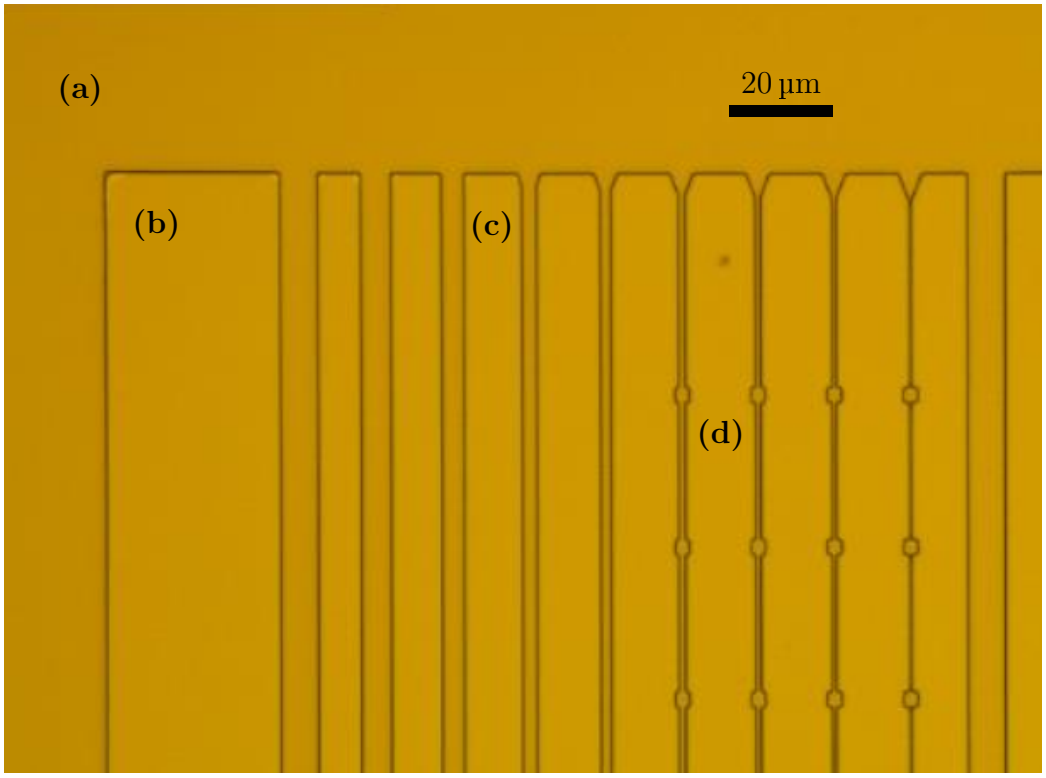

Figure 3.3: A bright field microscope image of a part of an etched cover slide. Using laser lithography and reactive ion etching we have created sub-wavelength structures that will later be occupied by atomic vapour. **(a)** Etched area of the cover slide creating expansive 2D vapour environment, the etch depth is $\sim 500\,\mathrm{nm}$ in this example. **(b)** Unetched area of the cover slide, this surface will form an optical contact bond to the front face of the block. **(c)** Set of channels etched with various widths. **(d)** Some channels include multiple 0D 'pockets'. The scale bar in the upper-right corner indicates the size of these features. Image courtesy of Jan Renger.

absence of fringes or reflections as the two glass surfaces come into direct contact with each other. The OCB can then be 'massaged' to encourage the bond to form across the cover slide with the minimum requirement being that the bond totally surrounds the nano-structures (e.g. figure 3.2b). During this phase, tiny dust particles will be sufficient to keep the glass separated and these can be seen as an area that appears to repel the formation of an OCB. The existing OCB is totally reversible and hence the two glass pieces may be separated, cleaned, and the process repeated until a clean and continuous

bond that encircles the nano-structures is formed.

To make the OCB permanent the newly formed nano-cell head (block and cover slide) is fired in a kiln to 1000 °C for 6 h. The firing scheme has been inherited from prior knowledge [17] and a detailed investigation to optimise the procedure has not been necessary.

3.3.4 Loading

Introduction of rubidium to the nano-cell must be done under a vacuum or inert atmosphere. We opt to use a vacuum to avoid complications to the atomic system when a buffer gas is present, although a nano-cell filled with inert buffer gas may be of future interest. The bonded block and cover slide are attached to a borosilicate glass manifold which is in turn connected to a vacuum pump and a vacuum sealed rubidium vial with a break-seal. The entire manifold is evacuated by the vacuum pump to $\sim 1 \times 10^{-6}$ mbar. A previously inserted steel bar is manipulated with an external magnet to break the glass seal, releasing the rubidium into the manifold. Rubidium has a melting point of 39 °C and can be readily liquefied with a low flame. Liquid rubidium is allowed to flow under gravity until it is made to solidify near the nano-cell. The nano-cell and nearby rubidium deposit can then be closed off and detached from the rest of the manifold to produce the self-contained nano-cell as depicted in figure 3.1. The evacuation, loading, and glassblowing were performed by the Chemistry department at the University of Durham.

3.4 Operation

In this section we describe the practical use case of our nano-cells within this thesis. We include a novel method of measuring the nano-channel internal thickness in situ, using white light spectroscopy.

We will then discuss the evolution of techniques and technologies used to control the atomic vapour density. Although most methods are generally applicable to thermal vapour experiments, we present the benefits and drawbacks of each solution with our specific experimental aims in mind. Additionally, we will discuss rubidium condensation, something typically avoided and seen as problematic in vapour cell experiments. This leads us to consider how we might manipulate condensation to our favour. Finally, we end with a comment on the longevity of our nano-cells.

3.4.1 Characterisation

Precise measurement of the internal dimensions of the nano-cell is essential for quantifying the atom number involved in experimental observations. Although the fabrication process is reliable and reproducible, the colour variation observed across the nano-cavities (figure 3.2b) indicates that the cavity is not uniform as would be expected from the uniform etch depth. Moreover, each nano-cell has a unique pattern of coloured Newton's fringes suggesting that the internal 2D layer thickness differs between nano-cells. This deviation is likely to be due to mechanical stress and relaxation that occurs during the kiln firing stage of bonding. We also observe that the colour fringes change after the firing process, giving weight to this hypothesis. Therefore it is

necessary to measure the cavity depth profile after the nano-cell has been assembled.

Others (e.g. [16, 57]) have employed a method whereby a laser is reflected from the nano-cavity onto a photodiode. By counting oscillations in the reflectivity as a function of position, one can determine the thickness of the cavity relative to a zero thickness cavity. This method requires that the nano-cavity has a certain property: the area of interest in the nano-cavity must be continuously connected to a region of zero thickness by a smoothly varying profile. i.e. the cell must be internally wedge-shaped down to zero thickness. Our nano-cells do not have this property and hence the laser method cannot be used. Instead, we have developed our own method to measure the cavity thickness using white light spectroscopy. Our method is superior to the laser method in that it is an absolute measurement rather than relative hence it is a calibration-free in situ measurement that can be used for discontinuous cavity profiles as will be demonstrated.

3.4.1.1 White light spectroscopy

In contrast to the laser method, white light spectroscopy allows us to observe multiple cavity transmission peaks and to extract the cavity free spectral range directly. We exploit the fact that the nano-cell acts as a low finesse Fabry-Pérot interferometer, with the internal surfaces of the fused silica cavity acting as low reflectivity mirrors. We recall transmission, T, of a Fabry-Pérot cavity:

$$T = \frac{(1-R)^2}{1 - 2R\cos(\delta) + R^2}, \tag{3.1}$$

where R is the reflectivity at the fused silica interface, and $\delta = \frac{2\pi l}{\lambda}$ is the phase shift of each subsequent round-trip reflection, with l the cavity length

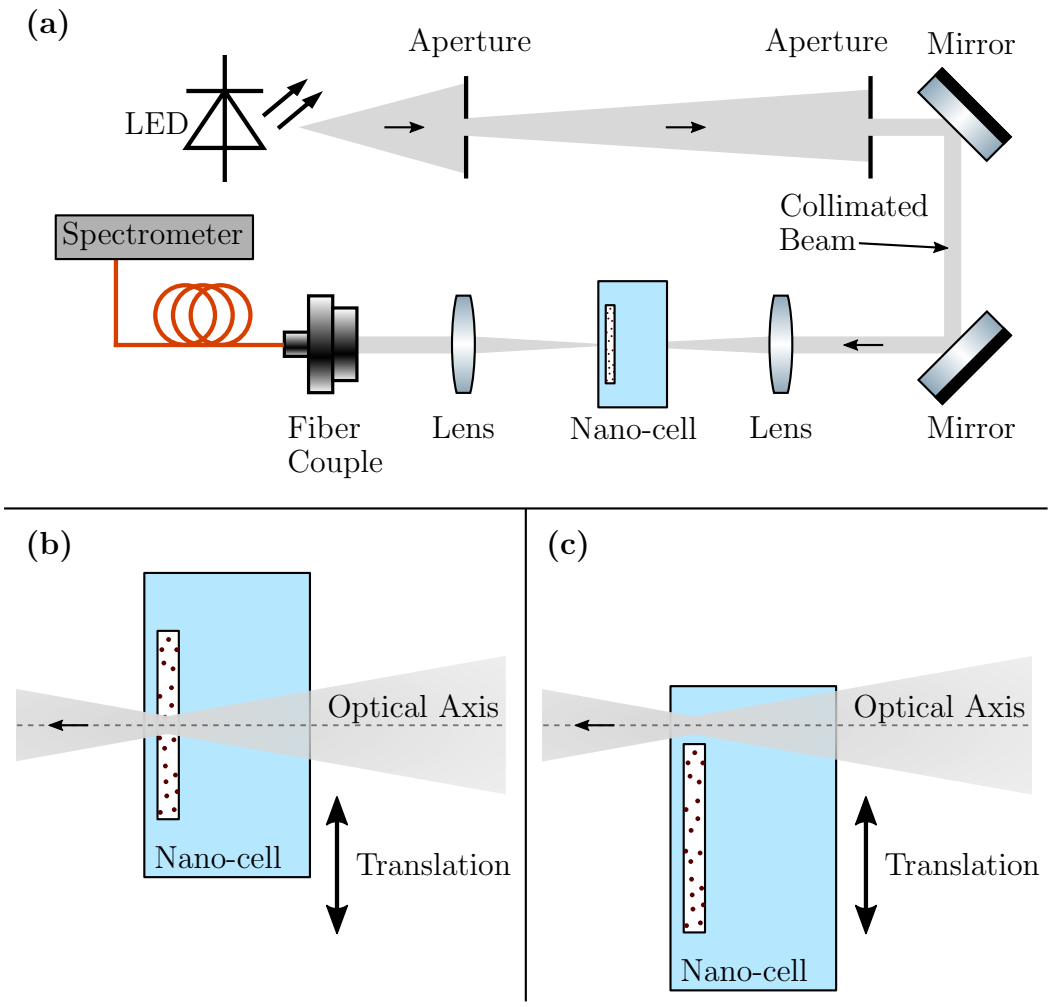

Figure 3.4: Schematic diagram of the white light spectroscopy method used to measure the internal thickness of the cavities within the nano-cell. **(a)** Optical table setup showing white light from an LED being collimated by two apertures before being directed through the nano-cell and collected by multi-mode fiber to a spectrometer. **(b)** Close-up look of the white light beam being focused through the nano-cell cavity. The nano-cell is translated to make incremental cavity thickness measurements in order to map the cavity profile. **(c)** The nano-cell can be translated such that the white light beam does not pass through the cavity at all. In this position, a reference transmission spectrum is recorded by the spectrometer.

and λ the wavelength of the probing light.

The free spectral range (FSR) of our micro-cavities is $\Delta v_{\mathrm{FSR}} = c/2l = 150 - 300\,\mathrm{THz}$, hence we use white light to span multiple Fabry-Pérot trans-

mission peaks. Figure 3.4 shows the experimental setup used. We begin by passing a weakly focused ($\sim$ 100 µm waist) white light beam from an LED though the block and cover slide but avoiding the cavity and record a reference transmission in this position (figure 3.4c). The white light focal spot is translated across the nano-cell such that it passes through the cavity (figure 3.4b) and the transmission is recorded again. The ratio of the transmission spectrum to the reference is taken, and this relative transmission is plotted in figure 3.5b. The Fabry-Pérot cavity resonances are revealed and fitted with a model using equation 3.1; the cavity length is extracted from the fit.

Figure 3.6 shows the result of a horizontal sweep across the face of the nano-cell with white light spectra taken at 0.1 mm intervals at a vertical position of 2 mm. We also observe the discrete depth changes as intended by design, and also the gradual thickness change that induces the visual colour gradient seen in the cell photograph (figure 3.2b). In this case the cell is concave showing a decreasing cavity thickness towards the middle of the patterned area (horizontal position $\approx$ 5 mm). This bowing is caused by deformation of the cover slide and is the reason for the inclusion of two fused silica pillars (two circles at {3.5 mm,1.0 mm} and {7.5 mm,1.0 mm}), to act as spacers preventing the cavity thickness from deviating further from the design specification when under vacuum.

3.4.2 Vapour density control

One of the key parameters that can be controlled in atomic vapour experiments is the inter-atomic spacing, which in turn governs the strength of the interaction between dipoles. With alkali species, the inter-atomic spacing is typically controlled by tuning the temperature of the system and exploiting

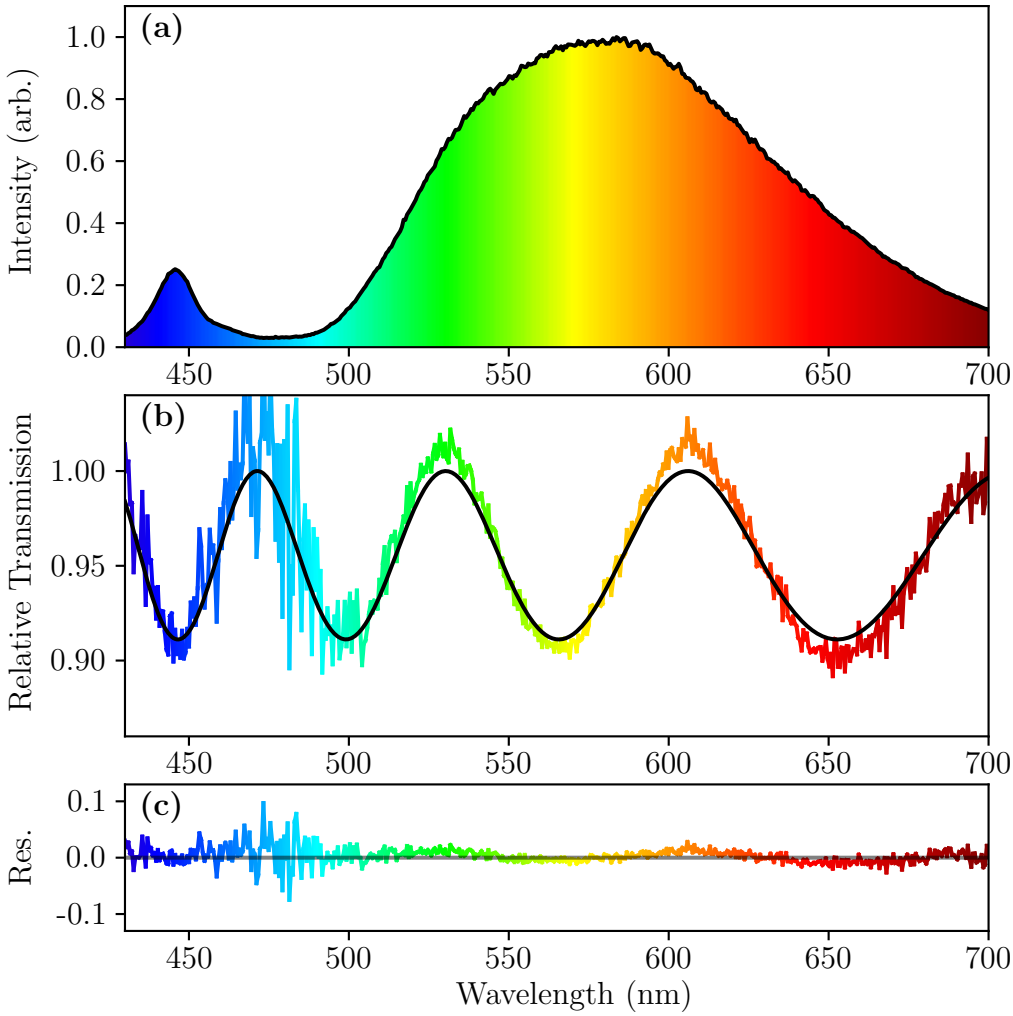

Figure 3.5: **(a)** White light spectrum transmitted through solid (no cavity) part of the vapour cell (as depicted in figure 3.4c) and recorded on a spectrometer. **(b)** Relative transmission of the same white light source when passed through the micro-channels in the nano-cell (as depicted in figure 3.4b). The channels act as a low finesse Fabry-Pérot interferometer. The black line is a fitted Fabry-Pérot model. **(c)** Residual between relative transmission and the fitted Fabry-Pérot model.

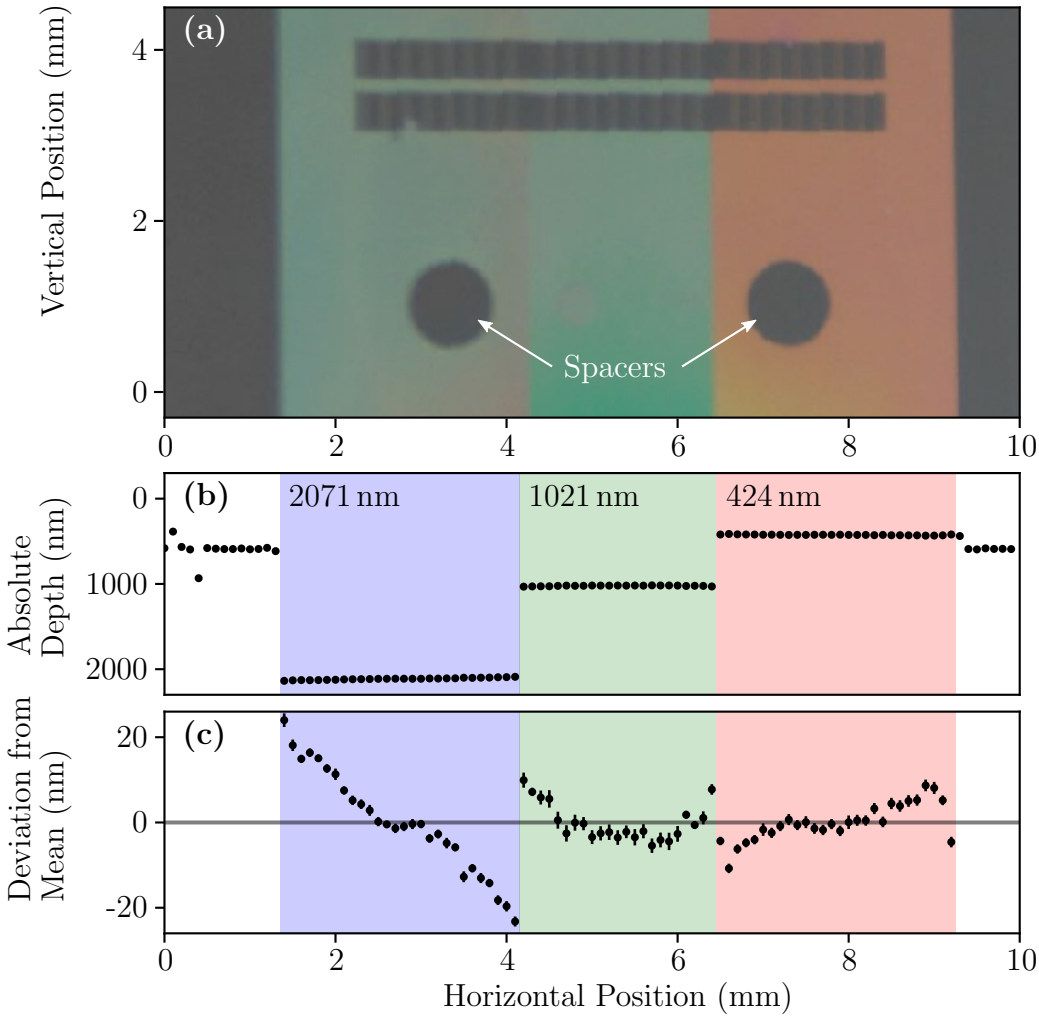

Figure 3.6: **(a)** A close section of the image shown in figure 3.2b. The 'spacers' are columns of fused silica left unetched to prevent the cavity from excessive deformation. **(b)** Absolute cavity thickness extracted from the fitted Fabry-Pérot transmission model as a function of lateral position across the nano-cell. The pass was made at a vertical position of 2 mm. The inset numbers in each shaded region show the average depth for that region. **(c)** Deviation found by subtracting the local region average depth from each data point.

the generous range of vapour densities afforded by the vapour pressure curve (figure 1.1). We have explored a number of methods of temperature control in the nano-cell each with their own merits. They are presented in the following subsections.

An important consideration when designing a heating solution for an alkali vapour cell (large or small) is condensation. Regardless of operating temperature, a thermal gradient must always be maintained to ensure that rubidium condensate does not form on the surfaces that are required for optical access. Thus a thermal gradient must be engineered into the design of any effective heating solution.*

3.4.2.1 Ovens

The most widely used heating method, due to its simplicity, is the cell oven. The oven acts as the mount and heating enclosure for the nano-cell. Cell ovens are advantageous in that they are relatively simple and cheap to make. Ovens are also capable of reaching significant temperatures as their size allows for the inclusion of effective thermal insulation.

A downside to using cell ovens is their large size. This means that they are slow (typically many tens of minutes) to change temperature and to reach a steady state even with active temperature stabilisation. Although, a happy coincidence of the large thermal mass is that the nano-cell is protected from thermal shock in the event of a power failure.

Cell ovens were not used for a majority of the work in this thesis due to optomechanical constraints. Ovens do not typically allow for a great degree of optical access, nor do they facilitate the use of high NA (and hence short

*An exception to this case will be discussed in chapter 6.

working distance) optics. Additionally, the nano-cell is not directly mounted to the optical table and is therefore subject to positional drift as the oven undergoes thermal expansion and contraction.

3.4.2.2 Wire wrapping

A short term solution that was used to great effect was to directly attach heating element wire to the nano-cell. The same wire used in cell ovens was attached using Kapton tape to the external faces of the nano-cell not needed for optical access. The major advantage of this approach is that the nano-cell could be directly mounted to the optical table and be compatible with short working distance optics. Direct mounting of the cell also provided the necessary mechanical stability to probe the sub-micron scale structures inside the nano-cell.

The disadvantage of this method is that with limited surface area to place the wire and without thermal insulation the nano-cell cannot be heated to such high temperatures. Additionally, using Kapton tape to secure the wire gave a limited lifetime (typically 1-2 weeks) as the tape would perish under the heat of the wire and eventually fail. After failure, the wire can be removed and replaced with no lasting damage to the nano-cell.

3.4.2.3 CO_2 laser

Both the cell oven and the wire wrap method of heating lack the ability to apply localised heating or to rapidly change the temperature of the nano-cell. A potential solution for enabling such features was to utilise a CO_2 laser at $\lambda = 10.2\,\mu\text{m}$ to directly heat the nano-cell. The CO_2 laser could be focused to provide spatially selective heating, albeit limited by thermal diffusion in

the glass. The intensity could also be modulated to induce fast changes in the vapour pressure. Some tests were done but the method was ultimately not adopted because of the complexity of delivering the 10.2 µm light via the same high NA optics used for imaging and spectroscopy. The glass of the cell strongly absorbs the 10.2 µm light and the beam energy is thus deposited into the glass which causes the nano-cell to heat. However, the penetration depth is extremely short and so the CO_2 laser would only heat the external surfaces of the nano-cell, and in turn this heat would diffuse through the glass to reach the atom layer inside. Therefore the CO_2 laser provided a similar feature set to the cell oven and wire wrap methods, but with considerable added experimental complexity. Investigatory CO_2 laser experiments were performed by the author in Erlangen, Germany.

3.4.2.4 Indium Tin Oxide (ITO)

The most developed iteration of our nano-cells includes a patch of Indium Tin Oxide (ITO) on the rear side of the block. The ITO layer is a transparent conductor that is used as a resistive heater by passing through a current. Electrical contacts are made by sputtering gold pads along opposite edges of a rectangular area of ITO (see figure 3.1).

The ITO patches are thermally and mechanically robust. Additionally, the transparency does not compromise optical access. ITO also enables a large operational temperature range and long working lifetime.

One difficulty faced with using ITO is connecting the driving power supply to the chromium contacts to provide electrical power. Silver epoxy and soldering have been employed to attach wires, each with limited success. An adhesive-free, press contact solution is in development. ITO development was done

partly by our collaborative technician Jan Renger at the Max Planck Institute in Erlangen, Germany. Later iterations were done by a third party supplier Diamond Coatings, in the UK.

3.4.2.5 Light Induced Atomic Desorption (LIAD)

Perhaps the most ideal solution for manipulating atomic density is to circumvent the need for any heating at all, and this is possible with LIAD. LIAD is a process whereby atoms condensed on the internal surfaces of the nano-cell are promoted into the vapour phase by a non-resonant light source [78]. The non-resonant nature of the effect allows for a wide choice of wavelengths to be used and a compatible choice with the existing experimental setup can be made. The desorbing light can be well focused and switched rapidly to provide excellent spatial and temporal resolution of atomic density changes. The nano-cell does not interact with the desorbing light directly so no heating effect is observed, and hence all thermal related problems typical of the heating methods previously described are avoided. A more detailed report of the initial works involving LIAD can be found in chapter 6.

3.4.3 Longevity

Our nano-cells typically outlive their novelty as production of new internal architectures move the experiment forward. We have seen nano-cells remain operational after $\sim 2\,\mathrm{yr}$ of use and having undergone hundreds of heating and cooling cycles in that time. We have constructed close to a dozen operational nano-cells.

Operation at higher temperatures (above $\sim 180\,^{\circ}\mathrm{C}$) appears to cause a reaction between the rubidium and borosilicate glass of the reservoir as expected.

The exact chemistry is not known but the reaction of rubidium with oxygen in the glass to form rubidium oxide seems plausible. The nano-cells that suffer from internal oxidation are visibly browned, although transmission at $\lambda = 780\,\mathrm{nm}$ is not directly affected. Using transmission spectroscopy, we observe that heavily oxidised nano-channels have an increased transmission on resonance implying that the nano-channel has decreased in thickness. This could be consistent with a build-up of an oxide layer in the nano-channel, but a direct investigation of this hypothesis has not been made.

During the design phase, consideration was given to the ability of the reservoir to nano-cell connection to withstand thermal shock. The borosilicate glass reservoir is attached to the fused silica nano-cell via glassblowing which results in a section of the completed nano-cell that transitions from one glass type to another. The two glasses have low, yet differing thermal expansion coefficients of $\sim 3 \times 10^{-6}\,\mathrm{K}^{-1}$ [79] for borosilicate glass and $\sim 0.5 \times 10^{-6}\,\mathrm{K}^{-1}$ [80] for fused silica, thus causing some mechanical strain across the bonded junction when heated. Only one nano-cell has failed at the glass bond, having formed a small crack which allowed atmosphere to enter the nano-cell and oxidise the rubidium within. This failure occurred after numerous successful thermal cycles, not during fabrication.

In summary, our design and fabrication method enable us to realise thermal vapour systems in a new format. We have created a platform for the study of atomic physics with greater optical access and inclusion of nano-scale structures. The operation and longevity are more than adequate for reliable experimental study.

3.5 Outlook

At each stage of development and advancement, the nano-cell has evolved to gain access to new physical regimes. In this section we propose some short- to medium-term goals that are readily accessible with the current fabrication scheme.

3.5.1 Atom number control

The most promising of all methods used is direct manipulation of the atomic vapour pressure with LIAD, which circumvents the inherent problems associated with heating. LIAD offers the fastest, most localised and most flexible option for controlling atom density inside the nano-cell. Work is ongoing to investigate pulsed LIAD such that atoms could be 'summoned' on demand, potentially removing the randomness of the atom number associated with thermal vapours and creating a switchable single atom source.

Additionally, ITO could be micro-patterned onto the nano-cell or to the inside of the nano-channels to provide novel thermal gradients within the nano-cell. This would allow for a closer study of nano-fluidic flow of the thermal vapour.

3.5.2 Photonic structures

Integration of waveguiding structures within atomic systems has already shown promise for the study of fundamental physics [52, 81, 82]. Devices have been demonstrated where thermal vapours interface with waveguides [83]. These systems use a constrained light mode and unconstrained vapour. Inclusion of waveguides within our nano-cells (which constrain the spatial extent of

the vapour) would open an avenue of unexplored physics. Given the scalable nature of our platform we display great promise for future devices, e.g. quantum networks and arrays.

Furthermore, waveguides could be used to deliver not just resonant light to probe the atoms, but also a LIAD light source to manipulate the number of atoms. Demonstrations of trapping schemes using the evanescent field around a nano-fiber [45, 46, 84] may be realised within our nano-cells also increasing the interrogation time of the atoms.

3.5.3 Lattice structures

Cooperative phenomena can occur in structured ensembles of interacting emitters [33–35, 85]. Experimental realisations of these structured arrays of dipoles is an emerging field with progress being led with cold atom approaches like optical lattices [86] and tweezers [87–91]. We propose that our nano-cell platform could be modified to include lattice-like structures in the etching process, thus creating an atomic thermal vapour with lattice structure. This approach is more scalable than arrays of addressable atom traps and experimentally less complex to implement.

A more speculative avenue of investigation would be to create a LIAD lattice in the nano-cell. By using a lattice shaped beam of desorbing light, LIAD could be performed to create a lattice-structured atomic density. Using light to create lattice shapes returns the benefit of having dynamic control over the lattice parameters as opposed to an etched structure that is fixed. The limitation of requiring lattice length scales of order λ could be overcome with more advanced lithographic techniques, or by selecting an atomic transition

for which λ is significantly larger than the minimum manufacturable feature size, e.g. a Rydberg transition.

3.5.4 Miniaturisation

Numerous other groups produce millimetre and micron scale vapour cells where the external dimensions are impressively reduced to obtain miniaturised atom based technologies (e.g. [14, 92, 93]). A reduction in the overall external dimensions will certainly be an avenue for advancement of the current nano-cell design. The current external dimensions of the nano-cell are constrained by the practical use of glassblowing to attach the reservoir. An alternative loading scheme such as a rubidium dispenser might be incorporated in future designs to remove the need for a reservoir attachment altogether.

Chapter 4

Spectroscopy of atoms in a nano-cell

4.1 Introduction

In this chapter we explore the behaviour of atoms via the atom-light interaction. Spectroscopy, where the response of an atomic system is explored over a range of optical frequencies, can reveal many insights into collective [15, 37, 57, 77, 94, 95] and lone atom [42, 48, 73, 96, 97] phenomena. We will show that the particular choice of measurement determines the effects that become visible in the recorded spectra and demonstrate how our unique nano-cell design allows us access to new and unique measurement schemes. We will explore a familiar optical technique of total internal reflection fluorescence microscopy [98] but applied in a novel way to a nano-layer of atomic vapour. We address various transitions in the rubidium energy level manifold to benefit from frequency discrimination in detection. We demonstrate models that account for the spectral shape observed in the data as well as responding appropriately to the variations in external parameters. Where data and model

differ we speculate as to the cause and propose a deeper investigation to verify such claims. Ultimately we establish the accessibility of new spectral information made possible by our nano-cell design and suggest the most promising direction of further exploration of this domain.

4.1.1 Spectroscopy fundamentals

The non-physicist might assume that light and matter readily interact. We see the world around us, in colour, with light. Objects reflect light, and cast shadows and it is rare to find something that doesn't. However, when we look more closely, specifically at resonant atom-light interactions, we find that the frequency of the light must be a specific frequency in order to resonate with a particular transition in a particular atom. In fact, we rely on this truth to calibrate and normalise the atom-light interaction as laid out in appendix A. Only when the light and atoms are brought to the same location and the light is of the correct frequency (within Γ for a particular transition) can a significant interaction, manifested by an absorption of the incident light and subsequent fluorescence from the atoms, be observed.

Figures 2.2 and 2.3 show a section of the energy level diagram for ^{85}Rb and ^{87}Rb respectively. We exploit various detection schemes and employ frequency discrimination in detection all in the pursuit of a greater signal-to-noise ratio, enough to detect single atoms*. Our aim to reduce the number of atoms so extremely necessitates the use of multiple wavelengths and detection schemes not typically seen in thermal vapour experiments. The combination results in a platform where novel behaviour is seen in spectroscopy and a single atom

*This particular motive is explored further in chapters 5 & 6

might be isolated with all the simplicity that comes with a thermal vapour experiment.

We primarily adopt fluorescence based detection for its superior sensitivity and our nano-cell design enables the use of total internal reflection fluorescence microscopy. We lose direct knowledge of the frequency of the fluorescent light but this can be inferred from knowledge of the rubidium energy level structure and the frequency of the driving light field (or fields) [99]. The adoption of total internal reflection fluorescence (TIRF) and use of multiple driving fields reveals spectral signatures of interesting atomic behaviour, specifically that of the atom-surface interaction and this is explored later in the chapter.

Finally, we suggest a further method of highly sensitive fluorescence detection that avoids some complications arising from the multi-level structure of the rubidium atoms, by using a single frequency two-photon transition to probe the $5D_{5/2}$ state.

4.2 Total Internal Reflection Fluorescence (TIRF)

Throughout this chapter total internal reflection fluorescence microscopy (TIRF) [98] is used as the operating scheme of the experiment. This method allows for the recording of fluorescence spectra with exceptional signal-to-noise ratios. Our nano-cell design is made specifically to accommodate the use of TIRF. In the first instance we deploy a most essential TIRF implementation with a single laser that is scanned across the D2 line resonance in rubidium at

$\lambda = 780\,\text{nm}$. See appendix A for details of the calibration and locking scheme used for the 780 nm laser system.

4.2.1 Theory

Total internal reflection fluorescence occurs when the probing laser field forms an evanescent wave within the medium of interest driving excitations and spontaneous fluorescence from that medium. For total internal reflection to occur the medium of interest must be of lower refractive index than the medium that the laser travels through to reach it. An alkali vapour nano-cell is well placed to meet these condition, as the atomic vapour (refractive index ≈1) is surrounded by the fused silica of the nano-cell (refractive index ∼1.45 [100]).

Let us define θ_1 as the angle between the surface normal and the incident k-vector of the probing laser, n_1 the refractive index of the medium carrying the laser, n_2 the refractive index of the target medium, and θ_1 the angle of the outgoing beam to the surface normal. For a sufficiently small angle, the beam is simply transmitted (and partially reflected) according to Snell's law:

$$n_1 \sin\theta_1 = n_2 \sin\theta_2. \tag{4.1}$$

The change in angle as the beam passes from one medium to the other is called refraction. For a propagating solution to exist we require:

$$\begin{aligned} \frac{n_1 \sin\theta_1}{n_2} &\leq 1, \quad \text{or} \\ \sin\theta_1 &\leq \frac{n_2}{n_1} \approx 0.7, \end{aligned} \tag{4.2}$$

using $n_2 = 1.45$ for fused silica and $n_1 = 1$ for the vapour. Thus there exists an angle, θ_c, called the critical angle of incidence, above which there are no

propagating solutions for the outgoing angle of the transmitted beam. It is here the total internal reflection occurs.

At the vapour layer where total internal reflection occurs, an evanescent light field is created* that can drive excitation in the atoms and induce fluorescence. Although strictly 3-dimensional, we consider only the variation of the laser field as a function of distance from the surface. The evanescent field has the general form $\mathrm{E}(z) = \mathrm{E}_0 e^{-z/\mathrm{d}}$, where E_0 is the electric field at the boundary immediately outside of the medium in which the total internal reflection is occurring. z is the perpendicular distance from the fused silica wall into the vapour, and 'd' is the evanescent field decay length given by [98]:

$$\mathrm{d} = \frac{\lambda}{4\pi}\left(n_1^2 \sin^2\theta_1 - n_2^2\right)^{-1/2}, \tag{4.3}$$

with n_1 the refractive index of fused silica (≈ 1.45), n_2 the refractive index of the vapour (nominally taken as 1), and λ the vacuum wavelength of the light field (we probe the D2 line at $\lambda = 780\,\mathrm{nm}$).

The exponential decay of the evanescent field means that the field strength asymptotically approaches zero but remains finite for all z. Therefore, the field is able to span the thickness of our 2D regions in the nano-cell and some degree of frustrated total internal reflection occurs. This is where the evanescent wave bridges the low refractive index gap and a transmitted beam is still produced on the far side of the vapour channel despite the initial beam being incident above the critical angle. However, in our system the typical length scale for the evanescent field d is $50 - 100\,\mathrm{nm}$. Thus the transmitted beam produced on the far side of a $500 - 1000\,\mathrm{nm}$ vapour layer has a

*The solution is found by solving Maxwell's boundary conditions at the interface. One can also use the complex form of the sine function to solve Snell's law above the critical angle. The result is a complex wavevector that effectively changes the z component of the plane wave solution of the form $\mathrm{e}^{\mathrm{i}kz}$ into a real exponential decay $\mathrm{e}^{-|k|z}$.

negligible intensity. Moreover, the presence of the transmitted beam has no influence on the spectral response of the atoms, although detection of this minor transmitted mode may be of some interest in future investigations.

Thus we have introduced a new length scale, d, the decay length of the evanescent field. This length can be controlled by varying the incident angle, θ_1. Atoms travelling through the evanescent field will have a position dependent driving intensity and an altered transit time effect specifically for excitation. We explore the evolution of the TIRF spectrum as a function of the incident angle and model the data with a Monte-Carlo simulation.

Figure 4.1 depicts the core of the experiment when recording TIRF spectra on the rubidium D2 line. The fluorescence radiates isotropically and is collected by the microscope objective. The fluorescence is divided by a 50:50 non-polarising beam splitter (NPBS) cube that allows for simultaneous imaging of the nano-cell and laser spot (onto an EMCCD) and recording of spectroscopic data (on a fiber-coupled APD). The ability to have live video of the fluorescence spot inside the nano-cell is an essential feature for aligning the emission and collection areas as well as navigating across the nano-cell (by translating the cell) to the desired area of interest. This is especially useful for measurements where the recorded signal is exceptionally weak and thus it is impractical to align by optimising the signal in real time. For more sensitive work, the NPBS can be removed after alignment effectively doubling the activity on the APD.

Ideally there is no mechanism by which the probe beam light can enter the detection path other than by scattering from the atoms and hence the TIRF signal is a dark background measurement and offers exceptional signal-to-background ratio compared to transmission spectroscopy. In practice, the

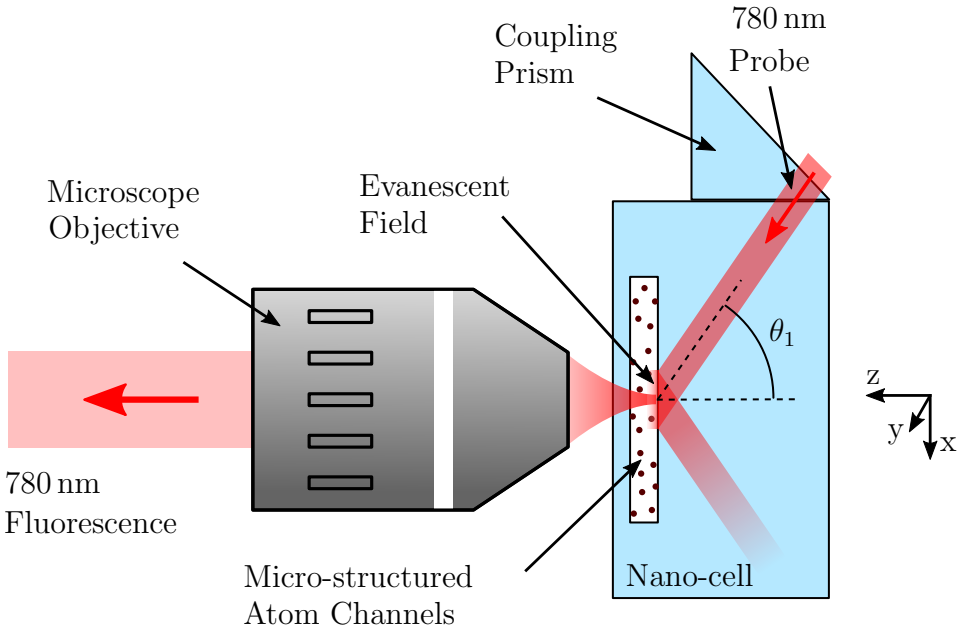

Figure 4.1: Schematic diagram showing the essential and unique components and setup of the TIRF implementation in our nano-cells. A 780 nm probe laser is coupled into the nano-cell with a prism. The beam is then totally internally reflected at the vapour layer and the atoms are driven by the evanescent wave that is formed. Fluorescent light is collected by the objective and directed to an EMCCD or fiber-coupled APD. The microscope objective can be switched to alter the magnification of the imaging system. The nano-cell can be translated in x, y, and z to selectively probe a certain area of interest or internal structure, and to optimise collection efficiency.

probe beam may still be scattered into the detection path by imperfections in the glass-vapour interface and so a clean and undamaged inner surface is essential. A further design advantage made possible with our nano-cells is the thin cover slide allowing the use of high NA lenses to capture the fluorescence. In turn, this means that a small collection area can be used and hence we have a large freedom to translate the nano-cell in x and y to locate an area where the glass-vapour interface is particularly scatter-free. The signal-to-background ratio can be continuously monitored as we translate the nano-cell to assist in finding a low noise area.

The magnification of the imaging system and the numerical aperture of the fluorescence capture can be altered by a choice of the microscope objective directed at the nano-cell. A low magnification lens is used initially for crude positioning of the nano-cell and alignment of the probe laser and collection areas. A high-NA microscope objective is then used for precise alignment and collection of fluorescence from a small area (down to $\sim \lambda^2$) with high-NA.

To focus the collection optics into the nano-cell we first illuminate the nano-cell with collimated incoherent light (typically a white LED torch) from the rear-side so as to project an image of the nano-cell through the microscope objective onto the EMCCD. The nano-cell is translated in z until the image is in focus. Weak laser light can be propagated along the detection path and the back-reflection used for precise positioning of the nano-cell. Newton's rings are observed in the camera and these can be made to converge to a well-focused spot by z translation of the nano-cell. In the case of large activity, one can further optimise the positioning by observing the activity in real time and moving the nano-cell to obtain a maximum. This has the added benefit of removing any additional focusing error in the camera optics.

4.2.2 Angular dependence of TIRF

The signal-to-noise ratio (SNR) is greatly improved by using TIRF rather than transmission spectroscopy. The boost to SNR was the initial justification for the TIRF method and it has been possible to record TIRF spectra at room temperature from the nano-cell. Furthermore, provided stray light can be mitigated, the SNR can be boosted by simply increasing the laser driving intensity, a property not shared by transmission spectroscopy. Similar conditions would yield such low optical depth that transmission spectroscopy

is simply not viable as a detection method. The ability to operate at room temperature will be a major advantage that will be discussed in later chapters where low number of atoms and exceptional mechanical stability make other novel experimental results available. In this chapter we use TIRF to reveal information about the local environment experienced by atoms in the nano-cell by scrutiny of the fluorescence spectra, and with computational modelling.

Figure 4.2 encapsulates a number of findings from TIRF spectroscopy. Firstly, the SNR obtained from a vapour layer of thickness 2 µm at 100 °C is clearly superior to that of transmission spectroscopy (see figure A.2a for example). Such conditions would lead to an expected absorption of just 2 % (value obtained using ElecSus [4, 101]).

Figure 4.2c shows the trend in FWHM of the spectra as the incident angle of the probe laser is varied. We see that the spectrum broadens as the incident angle increases. We attribute this change to the increase in transit-time broadening due to the shorter evanescent decay length, d. A single-atom Monte Carlo simulation reproduces the general trend (figure 4.2c, black dots), although a number of assumptions have been made which will need to be validated with further investigation.

4.2.3 Simulation and modelling

The model fitted to Figure 4.2a and Figure 4.2b is a simple 4-Voigt sum. A Voigt line shape is added to represent each of the four hyperfine ground states. The amplitudes and line centres of each Voigt are left independent to fit the data but they share common Gaussian and Lorentzian component widths. The FWHM of a single peak is then extracted after fitting and is represented by a single circle in figure 4.2c.

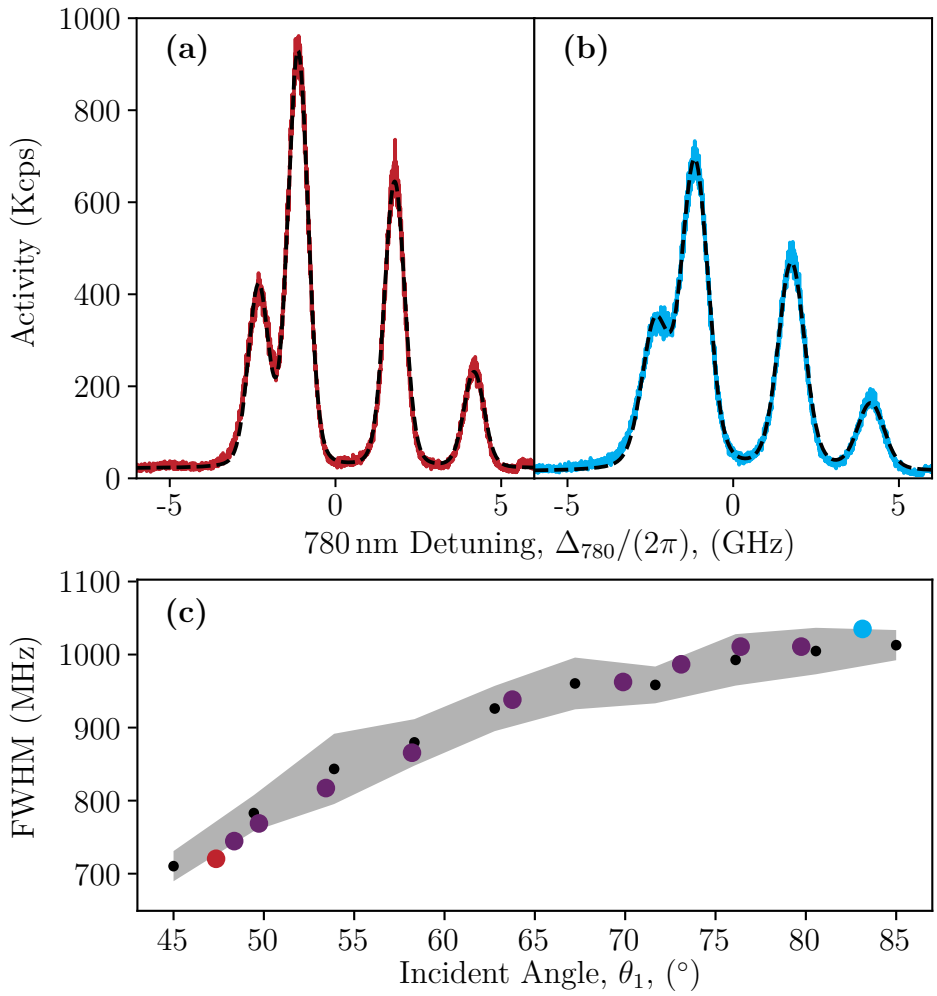

Figure 4.2: **(a)** TIRF spectrum of the D2 line in rubidium (red) recorded with an incident angle of $\theta_1 = 47°$ onto a 2 µm thick vapour layer at 100 °C, and a fitted Voigt model (black dashes). **(b)** TIRF spectrum (blue) taken with $\theta_1 = 83°$, 2 µm thick vapour layer at 100 °C. **(c)** Extracted FWHM of the Voigt model as a function of the incident angle (coloured dots). The extreme data points are colour matched to the spectra shown above. Also plotted are a series of discrete Monte Carlo simulations (black dots, shaded area to indicate 1 standard deviation) that simulates the frequency response of the vapour. The model is described in detail in the following subsection.

The theory points plotted in figure 4.2c is obtained by Monte Carlo simulation. We employ a single-atom simulation to generate a lineshape for a two level atom and extract a FWHM from the resulting spectrum. Figure 4.3 depicts the local environment of the atom in the nano-cell during a TIRF measurement. The model starts by initiating an atom with 3D velocity vector $\vec{v}$ sampled from a Maxwell-Boltzmann distribution. A Lorentzian peak is then produced for this atom with a modified linewidth given by:

$$\Gamma_{\text{eff}}^2 = \Gamma_{\text{nat}}^2 + \left(\frac{\alpha}{t_{\text{trans}}}\right)^2, \tag{4.4}$$

where Γ_{nat} ($= 2\pi \times 6\,\text{MHz}$ [56]) is the natural linewidth, t_{trans} ($= \text{d}/v_z$) is the transit time of the atom across the evanescent field, and α is a free parameter that modifies the weighting of the transit-time broadening. The generated Lorentzian is added to the model spectrum with the centre moved by the Doppler shift, which now occurs along the x axis:

$$\omega' = \omega_0 - \vec{k}_e \cdot \vec{v} = \omega_0 - \vec{k}_e \cdot \hat{x}\ v_x \tag{4.5}$$

The process is then repeated many times with a newly randomised velocity vector until a large number of Lorentzian lines (3000 in this case) have been added. The resulting sum gives a broadened lineshape centred around ω_0. The FWHM of the resulting lineshape is recorded and the simulation is repeated multiple times to obtain a standard deviation of the simulated FWHM. The random error in the simulation is vanishingly small with increasing number of atoms simulated, but a finite simulation must be performed for the sake of computation time. Thus the simulation produces a mean and standard deviation for each discrete angle simulated.

Finally, the simulation is repeated across the range of incident angles, θ, as this affects the evanescent field decay length, d, in turn changing the lineshape

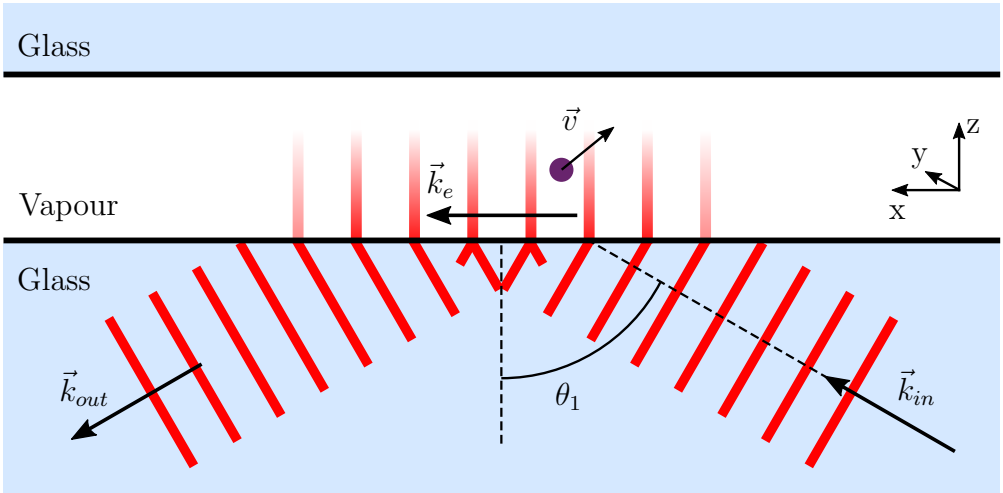

Figure 4.3: A close view diagram of TIRF and the local environment experienced by the atoms. The probe laser is incident on the vapour layer with k-vector $\vec{k}_{in}$ such that total internal reflection occurs. Inside the vapour layer an evanescent wave is formed with k-vector $\vec{k}_e$ which only has a propagating component in the x direction. The electric field strength decays exponentially with increasing z. An atom (purple circle) will experience a Doppler shift due to the x component of its velocity, and a transit-time broadening due to the z component of its velocity.

width due to the transit-time broadening in z. We find $\alpha = 0.3$ gives the optimal fit to the data.

4.2.4 Discussion

The data in figure 4.2c clearly indicates the dependence of the fluorescence FWHM on the incident angle of the probe beam. Our model recreates this trend with a crude transit-time broadening mechanism. The necessity for the parameter α to reduce the transit-time broadening effect demonstrates the need for inclusion of more features of the physical system. Firstly, the position dependent laser field intensity due to the evanescent field could result in a position dependent (and therefore time dependent as the atoms move) Rabi frequency that populates the excited state.

We suspect that atoms in extreme proximity to the internal surfaces of the nano-cell may not have a comparable density or velocity distribution to atoms in a bulk vapour [2, 43, 61, 62, 102–105]. This is perhaps the most challenging of questions to answer as knowledge of individual atomic trajectories is not readily accessible. Instead this can only be inferred by the overall lineshape seen from interrogation of the whole atomic ensemble.

Collective effects might also play a role. Although the temperature of 100 °C used in these results would not typically warrant the inclusion of collective effects, the enhanced sensitivity of the TIRF method may well call for such a complete treatment. A study of the vapour density dependence of the TIRF spectrum could lead to insights here. Additionally, as we can change the numerical aperture of the collection with ease, we can control the number of atoms that are detected. Thus we could conceivably study the evolution of the spectrum as a function of the total number of atoms contributing to it. This would allow us to decouple collective effects of the atoms from collective emission. For example, one could ask what the emission from a single emitter looks like when that single emitter is part of a strongly interacting ensemble.

In summary, our TIRF spectroscopy shows that we are sensitive to atom-surface interactions. The proximity of atoms to the surface and the thickness of the evanescent field appear to cause a broadening effect. To enhance our sensitivity to the atom-surface effects and boost overall SNR, we can excite and detect fluorescence from a different set of energy levels in the rubidium atom. This is done with two infrared probe lasers.

4.3 Two-photon total internal reflection fluorescence

To enhance the SNR and explore new spectral features we add a second laser at $\lambda = 776\,\text{nm}$ to the experiment. With both laser fields present we can drive atoms into the $5P_{3/2}$ state with the 780 nm laser, and then drive a second excitation from $5P_{3/2}$ to $5D_{5/2}$ with the 776 nm laser. From there, the atoms may decay via $6P_{3/2}$ (with a probability of $\sim 10\,\%$ [71]) to the ground state and release a 420 nm photon in the process (see energy level diagrams figure 2.2 & figure 2.3). We are then able to frequency discriminate the fluorescence to achieve an exceptional SNR when detecting the 420 nm fluorescence.

In this section we will demonstrate the novel spectral response observed when using 420 nm fluorescence detection from a two-photon TIRF experiment. Notably we identify two distinct features in the data cased by the two processes that lead to population in the $5D_{5/2}$ state (and thus 420 nm fluorescence): the single-photon process and the two-photon process. One can image the 776 nm laser as a coupling laser between the $5P_{3/2}$ and $5D_{5/2}$ states, creating a dressed state close to the natural line centre of the $5S_{1/2}$ to $5P_{3/2}$ transition.

The single-photon process excites atoms from the ground state into the dressed state with a single 780 nm photon and hence is similar to a two-level transition and subject to Doppler broadening. This mechanism is responsible for the broad features seen in the data.

The two-photon process occurs when an atom simultaneously absorbs a 780 nm

and a 776 nm photon and is excited directly from the $5S_{1/2}$ ground state to the $5D_{5/2}$ state. This condition is met when the sum of the two photon energies matches the $5S_{1/2} \rightarrow 5D_{5/2}$ energy level separation and can still occur when the two laser are far from resonant with their respective transitions. As the two beams are counter-propagating this effect is Doppler-free* leading to sharp fluorescence features.

Finally, we highlight the enhanced sensitivity to atom-surface effects of the $5D_{5/2}$ state, and present a phenomenological model that reproduces some features of the spectrum.

4.3.1 Methodology

The optical system is set up in a near identical way to that in figure 4.1 but with an additional 776 nm beam that is co-linear and counter propagating along the existing 780 nm beam path. The design of our nano-cell makes the required optical access readily available. The APD is replaced by an analogue photomultiplier tube (PMT) for better sensitivity at blue wavelengths. The same EMCCD is used for alignment purposes.

The 776 nm laser is frequency calibrated as described in appendix B. An EIT reference is used to determine the detuning of both the 780 nm and 776 nm lasers.

*An atom with some velocity component parallel to one beam is still Doppler-shifted. However, it is equally and oppositely Doppler-shifted for the other beam and hence the sum of the two Doppler-shifted frequencies remains unchanged regardless of the atom's velocity.

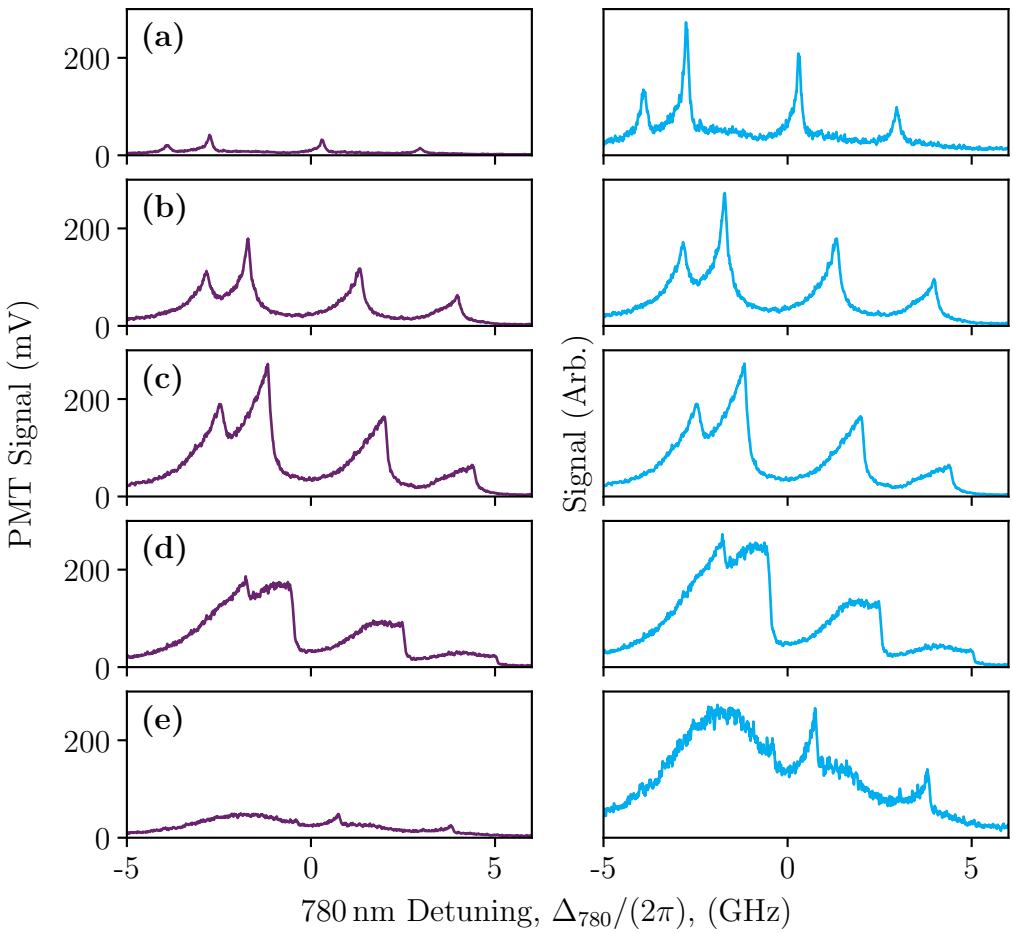

Figure 4.4: 420 nm fluorescence spectra obtained with two-photon TIRF from a 750 nm thick layer at 165 °C. Various discrete detuning of the 776 nm laser: $\Delta_{776}/(2\pi) =$ **(a)**1.5, **(b)**0.5, **(c)** $-$ 0.1, **(d)** $-$ 0.7, **(e)** $-$ 2.0 GHz. The panels to the left plotted in purple are displayed with a common vertical axis to highlight the large change in amplitude of the signal as Δ_{776} is varied. The neighbouring panel to the right, in cyan, is the same data but normalised to have unit amplitude for the sake of clearer depiction of the lineshape.

4.3.2 Detuning dependence of two-photon TIRF spectra

By offsetting the frequency of the 776 nm laser from resonance with the $5P_{3/2} \rightarrow 5D_{5/2}$ transition, we are able to separate the single-photon and two-photon driving processes that lead to 420 nm fluorescence.

Figure 4.4 shows a number of fluorescence spectra recorded with two-photon TIRF for various discrete detuning of the 776 nm laser to both the red and blue side of resonance.

Figure 4.4a depicts the spectrum when the 776 nm laser is far blue detuned ($\Delta_{776}/(2\pi) = 1.5\,\mathrm{GHz}$). The $5D_{5/2}$ state can now only be populated from the four hyperfine ground states of rubidium when the 780 nm laser is equally red detuned to compensate. We observe the four resonances are displaced to the red side compared to the position expected for D2 line resonance. The single-photon process is very weak in these conditions as the 780 nm laser is far detuned from the $5S_{1/2} \rightarrow 5P_{3/2}$ transition. Instead, the two-photon process dominates and we observe four Doppler-free resonances. This occurs when the photon energies sum to allow a transition from the ground state to the $5D_{5/2}$ state. These narrow features also exhibit an asymmetry in their long red tails. This is believed to be due to the atom-surface interaction which causes a red shift of the $5D_{5/2}$ state for atoms in close proximity to the fused silica walls, see below.

As the 776 nm laser is brought closer to resonance, the overall amount of fluorescence increases considerably, and we see a broadening as the single-photon process begins to contribute (figure 4.4b, $\Delta_{776}/(2\pi) = 0.5\,\mathrm{GHz}$). When very near resonance (figure 4.4c, $\Delta_{776}/(2\pi) = -0.1\,\mathrm{GHz}$), we see the largest amount of fluorescence and a very pronounced asymmetry in the lineshape. The sharp drop in fluorescence on the blue side of each peak is accounted for by the Doppler-free geometry and the long red tail occurs because of the 'smearing' of the $5D_{5/2}$ state as atoms distributed in the nano-cell (and hence with varying atom-surface induced red shift) all contribute to the overall lineshape.

Passing beyond resonance with a red detuned 776 nm laser (figure 4.4d, $\Delta_{776}/(2\pi) = 0.7\,\mathrm{GHz}$, and figure 4.4e, $\Delta_{776}/(2\pi) = 2.0\,\mathrm{GHz}$), the signal reduces in strength but the narrow, two-photon process remains as a significant contribution to the overall lineshape. We see that the narrow resonances remain in the expected locations of the D2 line for a lone 780 nm laser. The detection of 420 nm light is again possible due to the atom-surface red shift of the $5D_{5/2}$ state. Population can be driven from the $5P_{3/2}$ state up to $5D_{5/2}$ with a red detuned 776 nm laser provided the atom is sufficiently close to the surface that the red shift of the $5D_{5/2}$ state matches that of the laser and the transition is shifted into resonant. We also continue to see the Doppler-free two-photon process as it is largely independent of the detuning.

4.3.3 Simulation and modelling

For the modelling of the asymmetric two-photon TIRF spectra we assume a collective lineshape for the medium rather than modelling individual atoms in a Monte Carlo approach. We divide the nano-cell into separate volumes to which we assign a lineshape based on the volume size and position. A sum of all these individual contributions results in our overall lineshape. The model appears to qualitatively reproduce many of the peculiarities of the data, and the divergence of the model from the data shows that we have more to learn by examining such features.

Figure 4.5 depicts the stepwise elements that are included in the model to arrive at the set of features seen in the data (figure 4.4). We begin by taking the C_3/r^3 van der Waals shift of the $5D_{5/2}$ state as reported in [42, 59]. The potential is segmented into discrete steps of detuning. The local gradient of the potential then tells us the spatial extent over which the discrete value

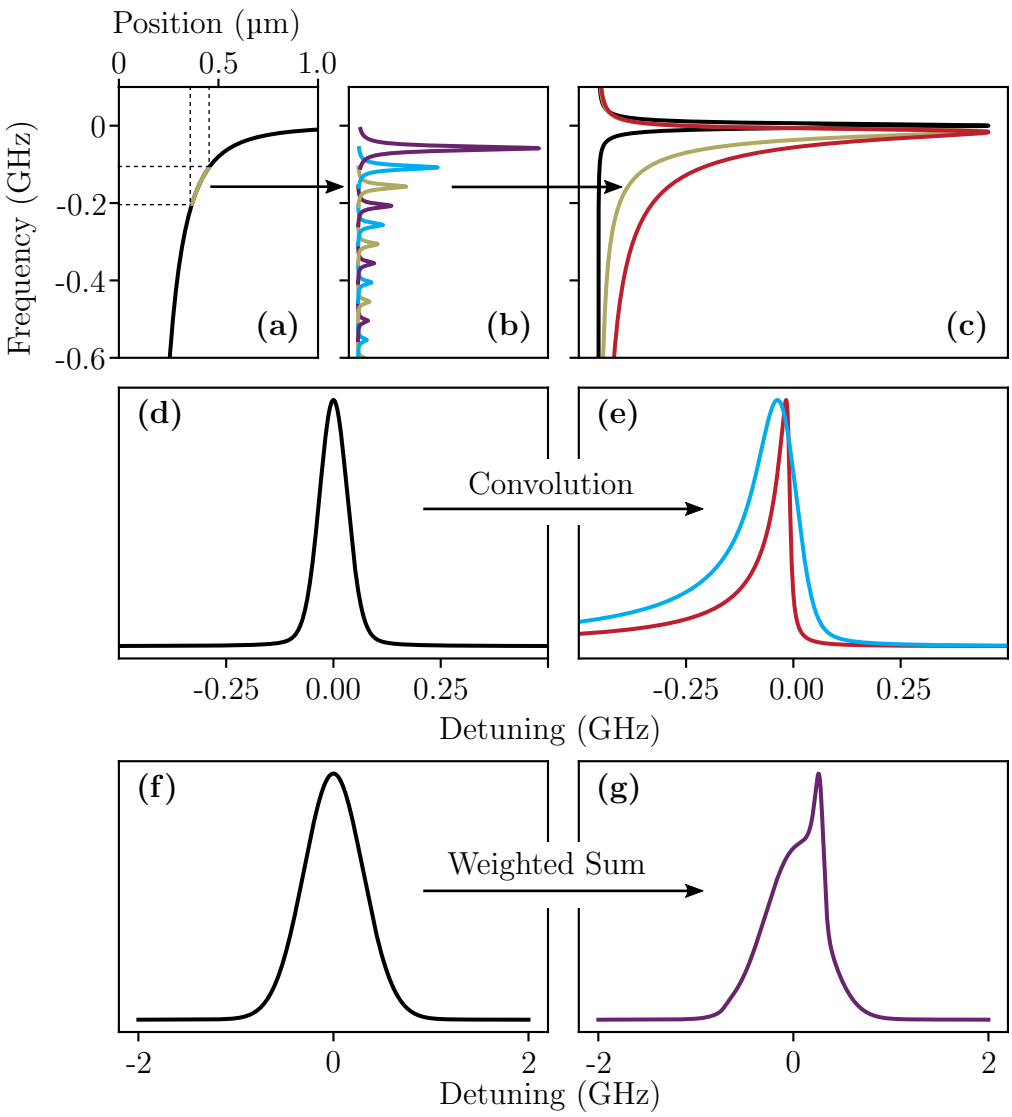

Figure 4.5: Sequential graphs showing the key elements that are included in the model to create the asymmetric lineshape, as seen in the two-photon TIRF data. **(a)** Energy shift of the $5D_{5/2}$ state caused by van der Waals interaction between atoms and the surface as a function of distance from the surface. **(b)** Centre-shifted Lorentzian lines to represent discrete portions of the potential (plotted with coarse intervals for clarity). **(c)** Natural lineshape (black), high resolution sum of segments (gold), and the effect of also including the evanescent field exponential decay on the weighting of the segments (red). **(d)** Additional Voigt profile to be convolved with previous shape to accommodate other broadening mechanisms (transit-time, power broadening, etc.). **(e)** Asymmetric lineshape before (red) and after (cyan) convolution with **(d)**. **(f)** Voigt lineshape with Doppler-broadening to represent the narrow, two-photon process of populating the 5D state. **(g)** Weighted sum of **(e)** and **(f)** with variable shifted centres of the two contributions (narrow transiion is shifted 300 MHz to the red side in this example).

can be assumed constant*. The segment of the potential in question (example highlighted in gold in figure 4.5a) then contributes a natural linewidth Lorentzian with amplitude corresponding to the position range spanned by that segment. We repeat the process to span the range of detuning and locations in the cell (but avoid the singularities at position = 0 and frequency = 0). A sum of all the segments results in an asymmetric lineshape (figure 4.5c, gold line). We can also include the effect of the evanescent decay of the light field, where we assume that segments of the nano-cell further from the surface are driven more weakly and therefore contribute less to the overall fluorescence. Inclusion of this exponential weighting results in an even more extreme asymmetry (figure 4.5c, red line), and apparent shift of the peak centre.

With the asymmetric line now giving some representation of the $5D_{5/2}$ state, we add a modification to account for other effects in the spectral shape. We perform a convolution between the asymmetric lineshape and a Voigt (figure 4.5d) that can have adjustable Gaussian and Lorentzian contributions to account for extra broadening effects in the system e.g. transit-time broadening, power broadening, self-broadening. We do not include Doppler-broadening at this stage as the counter-propagating geometry of the two infrared lasers should mean that we create a Doppler cancellation. We then arrive at the expected lineshape of the narrow, two-photon process (figure 4.5e), which has a further pronounced asymmetry and apparent peak shift.

Finally, we represent the sinlge-photon process with a Doppler-broadened line (figure 4.5f) that remains at the frequency of the D2 line resonance for the 780 nm laser (i.e. does not depend on the 776 nm laser detuning). Fluorescence produced by the sinlge-photon process must occur via population of the

*This approximation is only valid in the limit of infinitesimal divisions and we therefore decrease the detuning step size until the outputted lineshape converges and further increase of resolution has a negligible effect.

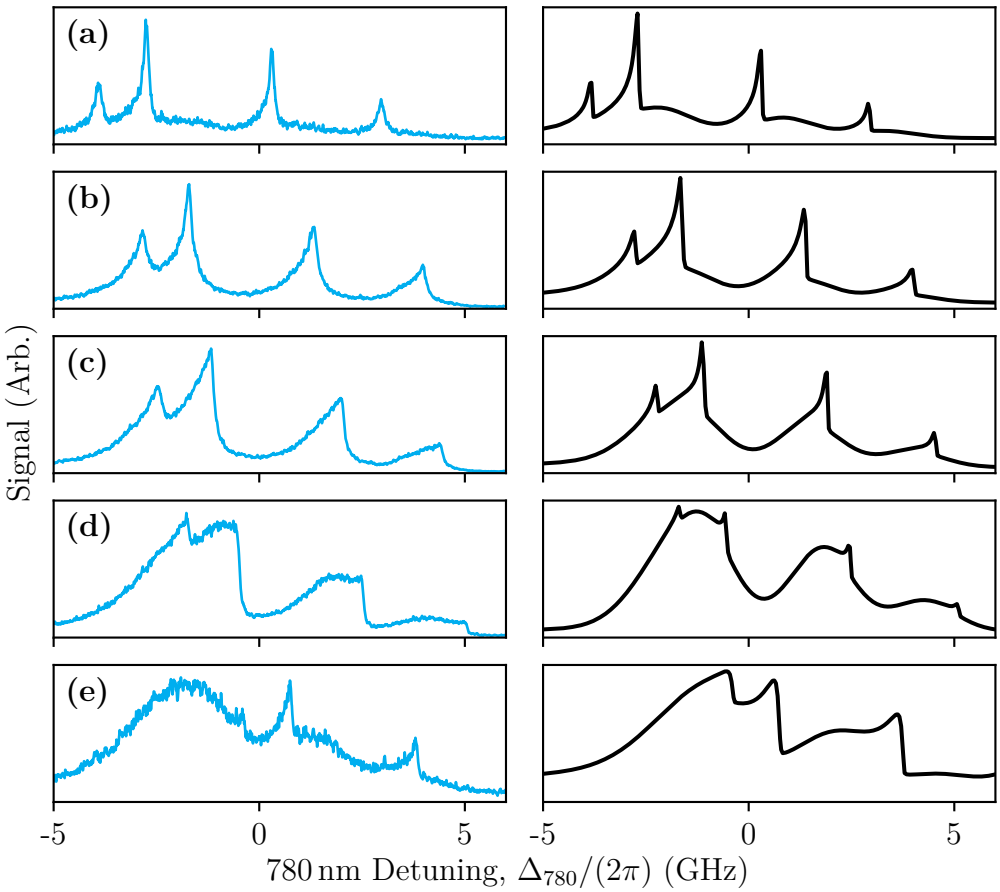

Figure 4.6: 420 nm fluorescence spectra obtained with two-photon TIRF with various discrete detuning of the 776 nm laser: $\Delta_{776}/(2\pi) =$ **(a)**1.5, **(b)**0.5, **(c)** $-$ 0.1, **(d)** $-$ 0.7, **(e)** $-$ 2.0 GHz. Left (cyan) is the experimental data re-normalised to maximum equal to unity (same data as figure 4.4), right (black) computational model. The model appears to recreate qualitative features of the experimental spectra although the success for a blue detuned 776 nm laser (a & b) appears to be better than that for a red detuning (d & e).

$5P_{3/2}$ state, and hence can only occur when the 780 nm laser is near resonance.

The combined line used to model the data is then simply a weighted sum of the single- and two-photon processes (figure 4.5g), copied for each of the four resolved hyperfine ground states.

Figure 4.6 shows a series of spectra and the simulated counterparts for a set of discrete detuning of the 776 nm laser. We find that the model provides a

good approximation for the spectral lineshape for blue detuning of the 776 nm laser but less so for red detuning.

As the 776 nm laser passes through resonance from the blue to the red, it is necessary to modify the weighting to include a larger fraction of single-photon driving. This attempts to simulate the emergence of the large broad features that are observed in Figure 4.6e. However, we see that the simulation appears to shift the D2 line resonances towards the blue side of the expected location in the 780 nm laser scan. This is not likely to be a true shift, but an apparent shift caused by the product of the asymmetric tail of the two-photon process making the single-photon process also appear asymmetric. Therefore, it is plausible that the exact form the the red tail of the two-photon process has a significant bearing on the overall lineshape (especially for a red detuned 776 nm laser). It may be the case that simply tuning the relative weighting of the single- and two-photon processes may be too crude a solution and in fact the two effects depend on one another more closely such that the lineshapes of either feature is affected.

The system has numerous complexities, the atom surface effect, the evanescent decay of the light fields, the two-photon process giving rise to two separate (yet intertwined) mechanisms to create 420 nm fluorescence, such that it will be necessary to decouple the effects before they are fully understood.

4.3.4 Discussion

We set out to gain in SNR by employing the two-photon TIRF method and in the process observed numerous spectral features that have not been reported before. Our established knowledge of the system allows us to construct a top-down model that reproduces qualitatively many of the peculiarities in

the spectra. We open the way for further study on this topic and suggest the beginnings of a reasonable model. Clearly further phenomena need to be included in order to quantitatively match the data.

We speculate that a more detailed treatment of the velocity of individual atoms will be necessary to explain fully what is going on. The lineshape observed in figure 4.4e (also figure 4.6e) is perhaps comparable to the extreme cases of velocity selection as reported in [106].

A full treatment of each atom may be necessary with dynamical optical Bloch equations to allow for the changing conditions that an atom may experience as it traverses the nano-cell and the two evanescent light fields. This would also account for the power of the beams causing EIT and Autler-Townes splitting effects (explored further in chapter 6).

4.4 Conclusion and outlook

The TIRF spectrum lineshape exhibits a number of novel features and the experimental setup gives a handle on a vast number of free parameters. The potential lines of investigation are plentiful. In the first instance then, it should make sense to simplify the system so that individual effects can be isolated, characterised, and understood.

4.4.1 Line shifts, widths, and asymmetries

For TIRF (and two-photon TIRF for added sensitivity) a precise look at the evolution of the width, line shift, or potential asymmetry gives detailed information about the environment experienced by the atoms. By sequentially

building the experiment and model to include each complexity of the environment one could work towards a full understanding of the lineshape, and then exploit that understanding to seek new knowledge. It is clear that the presence of the dielectric surface modifies the lines dramatically, and perhaps this could be used as a tool to perform a sensitive search of surface phenomena e.g. surface charges, or a repulsive atom-surface interaction caused by near resonance with the atom and the dielectric material [107].

4.4.2 Single frequency two-photon spectroscopy

The method of two-photon TIRF used employed a 780 nm laser and a 776 nm laser. This required two sets of laser stabilisation and frequency references, and also resulted in the two processes to excite the $5D_{5/2}$ state. One such route to avoid those complications would be to use two photons of equal frequency that sum to provide the right energy to make the transition $5S_{1/2} \rightarrow 5D_{5/2}$ directly. Work has already commenced with this aim using a single 778 nm laser.

Appendix C shows how a 778 nm frequency reference can be made, and figure 4.7 shows the resulting fluorescence spectrum. The principal idea is that two 778 nm photons sum to have sufficient energy to drive an atom directly from the $5S_{1/2}$ state to the $5D_{5/2}$ state. Additionally, the laser is far detuned (2 nm) from the 5P state such that the 5P state is not populated and any issues arising due to Autler-Townes splitting (see chapter 6) are also avoided. Sufficient optimisation of the frequency reference (and locking system which would need to be developed) could lead to the ability to individually address separate hyperfine levels as a Doppler-free configuration could also be realised with 778 nm light. The advantage would be to work with a system that could

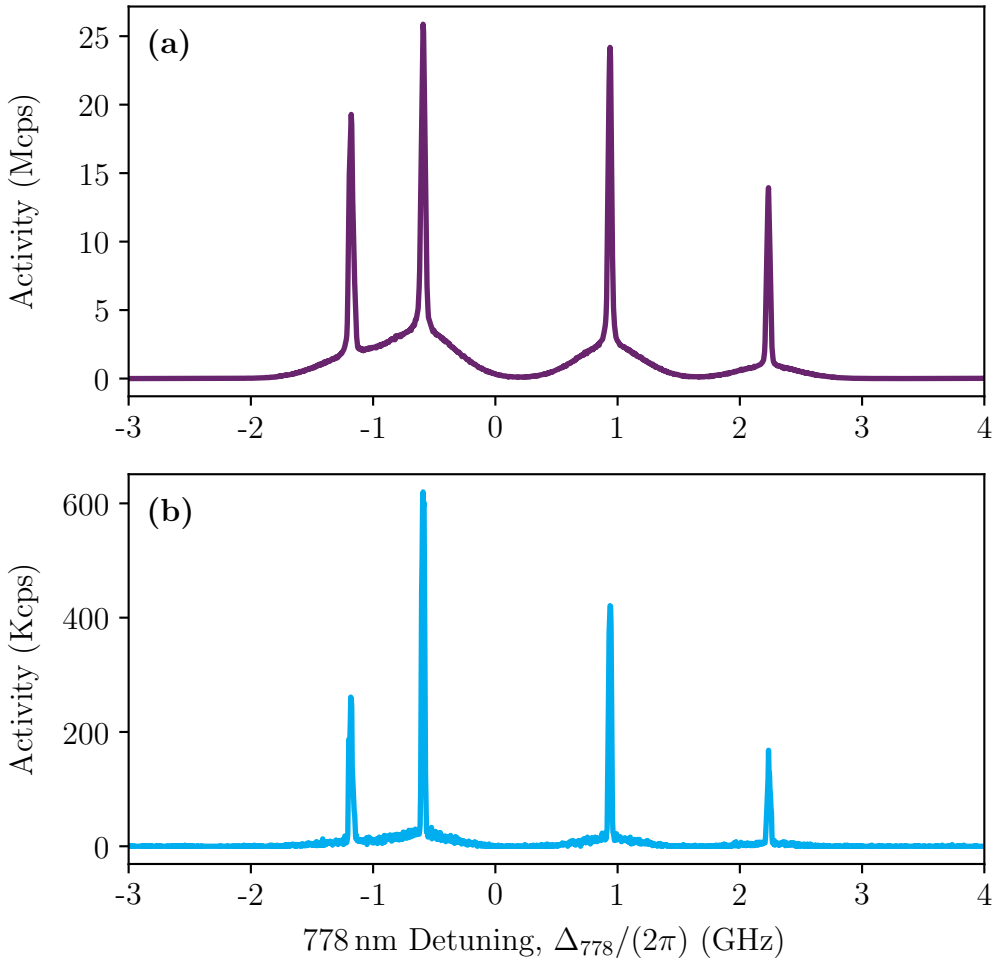

Figure 4.7: **(a)** 778 nm spectroscopy of natural abundance rubidium vapour at a temperature of 142 °C, thickness 2 mm. The spectrum is obtained with a PMT sensitive to blue light fluorescence as atoms decay from the 6P state back to the 5S ground state. The sub-Doppler features appear due to the double-pass geometry creating a velocity selection of the atoms with zero velocity. **(b)** An identical experiment with vapour at 19 °C, thickness 75 mm, to indicate the boost in activity achieved with heating (note the vertical scales). The scaling is not proportional to n (the vapour density) as the two experiments were performed in different vapour cells with different optical access and therefore collection efficiency. Nevertheless, the signal strength advantage of using a heated cell is evident by the $\times 40$ increase in recorded activity. With further optimisation it would be possible to resolve the separate hyperfine levels of the 5D manifold as demonstrated by [69].

be more readily modelled with a simple description, e.g. a two-level atom, by avoiding the single-photon process entirely.

4.5 Chapter summary

We have employed TIRF microscopy on a nano-layer of atomic vapour. Firstly, with a 780 nm laser on the D2 line we fitted a 4-Voigt model to the spectra and extracted the FWHM. We saw a broadening of the fluorescence that depended on the incident angle of the laser. We showed that a Monte Carlo model could explain the broadening as a transit-time broadening due to the very short evanescent wave. However, an investigation of other parameters (e.g. temperature) could reveal other dependencies that should be included into the model, and a more detailed spatial description of the light field experienced by the atoms is likely to be necessary.

Secondly, we adopted a two-photon TIRF method with both a 780 nm laser and a 776 nm laser and switched to detecting fluoresced 420 nm photons for the benefit of the SNR. We uncovered very peculiar lineshapes and are pleased to be the first to report and model such lineshapes. We produced a phenomenological model that reproduced many qualitative features of the data. However, we believe a full dynamical simulation will be necessary for a full understanding and quantitative description.

We propose that single frequency two-photon TIRF with a 778 nm laser may reduce the complexity of modelling and allow for the advantages of the surface-sensitive method to be levered.

All of the above findings are a direct result of our nano-cell design. Our unique fabrication method also allows for different dielectric material choices,

further enriching the available areas of investigation.

Chapter 5

Temporal intensity correlation of fluorescence from a nano-cell

5.1 Introduction

The quantum nature of atomic systems has recently driven experimental and theoretical investigations. Beyond spectral information and light filtering (e.g. [4, 108, 109]), it is the quantum nature of the atoms that offers new understanding and technology [28]. The long coherence time of atomic systems [23] makes them an attractive candidate for quantum information processing. Atoms can be manipulated to couple strongly with light, making the atom-photon interface a promising avenue for quantum communication protocols [19] and integrated devices [26]. Our nano-cells offer a novel, flexible, and accessible platform for such implementations.

Intensity correlation of detected light fields is a routine technique to quantify the internal states of an atom based quantum system. Historically, temporal correlations were performed on classical sources [110], however even thermal light sources offer enhanced applications when one considers the quantum

nature of the detected light field e.g. ghost-imaging [111].

Quantum memories have already been demonstrated [21, 24] and key parameters, such as speed and bandwidth, are being enhanced [22], demonstrating the operational potential of thermal ensembles in the quantum realm.

Further advancements can be achieved through information of temporal correlations [112], and cold atoms can give novel $g^{(2)}(\tau)$ functions [113–115], including perfect bunching ($g^{(2)}(0) = 2$ [116]). Quantum atom-light behaviour is also possible in hot vapour [117], typically by collective excitation [31, 118]. Although the exploration of temporal correlations of photons from a thermal vapour is still primitive [119].

Technologies like single photon sources have been demonstrated using thermal vapours [118, 120] and cold atoms [19, 32], and non-classical light has been recorded from single atoms [121]. Control of single quantum emitters [122] is of wide interest to the realisation of quantum networks, communication, and computation on a system of controlled qubits.

Measurement of the $g^{(2)}(\tau)$ function may provide great insight to the quantum state of the emitting system, and employing a scheme on the nano-scale offers another angle from which to understand the optical dynamics of small systems [123].

In this chapter we report on the first known observation of the second order temporal correlation of fluorescence from a nano-scale thermal atomic vapour. The nano-cell design enables unique observation methods and the flexibility of the architecture allows for near arbitrary spatial confinement of the atomic vapour. Our nano-cells combine the elements of atomic ensembles and low emitter number, providing experimental stability and simplicity for performing quantum measurements (and ultimately information processing)

in the atom-light domain. We explore a large section of the parameter space for our system and speculate the cause of the evolution in the $g^{(2)}(\tau)$ function. Finally, we use our findings to propose the most promising direction of future experimentation.

5.2 Theory

For the duration of this chapter we will consider light as a stream of discrete photons. The quantum interpretation of light and its sources, is necessary to explain some observed phenomena. One of the goals of this project is to isolate a single atom inside the nano-cell and a quantum description of light is required to interpret the evidence that a single emitter has indeed been isolated. Although we do not achieve that goal in this thesis, we still adopt the quantum picture of light to explain our results in a way that might prove most useful for progressing on to the single atom goal. A more detailed derivation of the concepts presented here can be found in many quantum optics texts e.g. [124].

5.2.1 Poissonian light

Let us begin by considering a beam of light with some fixed intensity I, and frequency ω. Using the energy per photon, $\hbar\omega$, we can interpret the beam intensity as a flux, Φ, of photons per second:

$$\Phi = \frac{P}{\hbar\omega}, \tag{5.1}$$

where P is the beam power calculated as a product of the beam cross-section area and the intensity. Thus in any unit time T, the expected number of

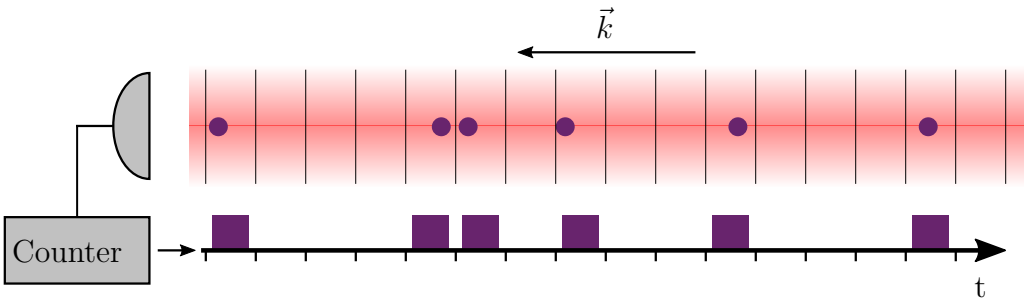

Figure 5.1: A laser beam can be considered a stream of randomly placed photons. A detector divides the incoming beam into time bins and records if a photon event occurred in that bin. The statistical fluctuations in the bin populations gives information about the source. For a real detector with dead time (a period of inactivity after each count), we must ensure that the time spacing between photons is likely to be larger than the deadtime ($\sim 30\,\mathrm{ns}$) to avoid missed counts, hence the flux must be low, typically less than 1×10^6 photons s^{-1}. This also reduces the probability that a single time bin of the beam contains two photons, which would be recorded as a single event by the detector. However, the maximum timing resolution (i.e. minimum time bin size) can be much faster than the deadtime and is limited only by the detector jitter ($\sim 350\,\mathrm{ps}$).

photons passing a given point (or incident to a detector) is given by $N = \Phi T$. The fact that N, the number of photons, must be an integer, and the fact that the exact location of the photons within the beam is not known gives rise to statistical fluctuations. It is the nature of these fluctuations that are of interest in this chapter.

Figure 5.1 shows a laser beam incident on a detector that contains a randomly distributed number of discrete photons. For a laser beam of constant intensity it can be shown that the photons are randomly distributed in time and that the occupancy of the bins recorded by a detector follow Poissonian statistics. Thus the mean bin occupancy is $\bar{N}$ and the standard deviation is $\sqrt{\bar{N}}$.

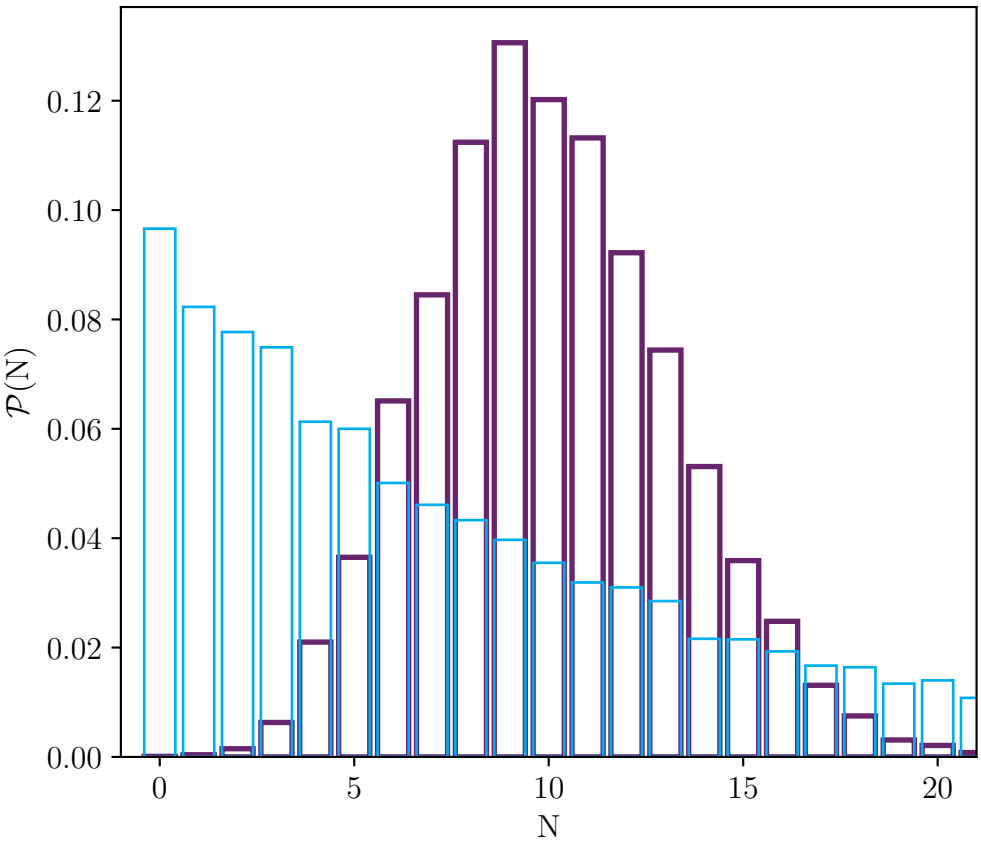

Figure 5.2: Histograms of 10,000 randomly generated numbers sampled from a Poissonian (purple) and Bose-Einstein (cyan) statistical distribution, each with the same mean photon number of $\bar{N} = 10$. Normalising by the total number of samples, the histograms display the effective probability $\mathcal{P}(N)$ of finding N photons in a finite time span for which the long term mean value is 10. For any value of $\bar{N}$, the Bose-Einstein distribution has a larger variance, and is thus classified generally as being 'super-Poissonian'.

5.2.2 Super- and sub-Poissonian light

We can classify light (and hence its source) by its photon statistics. Specifically, we look at the variance in the photon number per time interval and compare this to the variance of the Poissonian distribution, even naming them accordingly. Light with a variance greater than $\sqrt{\bar{N}}$ is referred to as super-Poissonian, and light with variance less than $\sqrt{\bar{N}}$ is referred to as sub-Poissonian.

Figure 5.2 shows histograms for both Poissonian light and an example of super-Poissonian light from a thermal source. The histogram for the thermal source shows specifically one mode of the light field. This is important to note as thermal light sources can give Poissonian statistics in the limit of a large number of detected modes. Hence experimentally, thermal statistics can be missed.

Observing sub-Poissonian light is the goal of many quantum experiments and acts as a benchmark for the performance of quantum single emitters. Sub-Poissonian light is not possible to explain in a classical picture and so constitutes direct proof of the quantum nature of light. Single photon sources, e.g. a single atom, will produce sub-Poissonian light.

5.2.3 Temporal correlations

To observe the photon statistics of light, one might assume that a setup like that of figure 5.1 is sufficient. However, one must decouple the statistical nature of the light from the statistical nature of the photon detection events in the detector. This is to say, a photon counter will always give discrete 'clicks' under incident light, but this is not sufficient to say therefore that the light source must be quantized. Instead, we must perform a temporal correlation of the light with itself and look at the resulting occurrences of pair-wise photon events (or lack thereof). In short we ask: when a photon is detected at time t, what is the probability that another photon will also be detected at a time $t + \tau$?*

For truly random light (Poissonian) the photon events are totally uncorrelated and therefore the probability of recording a second photon is equal for any

*τ can take any value, positive or negative.

value of τ. Explicitly, what we are formulating is the 2nd order intensity correlation function, defined as:

$$g^{(2)}(\tau) = \frac{\langle I(t)\ I(t+\tau)\rangle}{\langle I(t)\rangle\ \langle I(t+\tau)\rangle} \tag{5.2}$$

Where the parentheses $\langle \dots \rangle$ mean to take a long term average. Obtaining data that represents the $g^{(2)}(\tau)$ is rather subtle and our method is described in detail in section 5.3.2. We are able to record a histogram that approximates to the $g^{(2)}(\tau)$ albeit in a discrete time basis as a result of the discrete time binning and post-processing necessary in a real experiment.

The shape of the $g^{(2)}(\tau)$ function informs us about the photon statistics of the light. As alluded to earlier, Poissonian light returns $g^{(2)}(\tau) = 1$, a rather uninteresting result. Super-Poissonian light, also known as bunched light, manifests as a peak in the $g^{(2)}(\tau)$ function centred about $\tau = 0$, thus $g^{(2)}(0) > 1$. This tells us that when a photon is detected there is a greater probability of detecting another photon at the same time rather than at any other time. The photons are said to arrive in bunches rather than being randomly distributed along the beam. Sub-Poissonian light is characterised by a dip in the $g^{(2)}(\tau)$ function, or $g^{(2)}(0) < 1$. This implies that upon detection of a photon, there is a reduced probability of detecting another photon at the same time rather than at any other time. The photons are distributed uniformly in the beam, rather than randomly, and this is referred to as anti-bunching, or anti-bunched, light.

In all cases, the $g^{(2)}(\tau)$ function must tend to 1 in the limit of large τ as events outside of the correlation time are uncorrelated and random regardless of the type of source. This fact means that information about the coherence time of the source can be gained from looking at the shape and width of the peak (or dip) in the $g^{(2)}(\tau)$ function. For lifetime limited sources, the peak

has general form [125]:

$$g^{(2)}(\tau) \quad = \quad 1 + \exp(-2|\tau|/\tau_c), \tag{5.3}$$

and for Doppler-broadened sources has the form [125]:

$$g^{(2)}(\tau) \quad = \quad 1 + \exp\Big(-\pi(\tau/\tau_c)^2\Big). \tag{5.4}$$

Where τ_c is the coherence time in both cases. Note that the form of the $g^{(2)}(\tau)$ function relates to the spectral properties of the lineshape by Fourier transformation into the time domain. Thus the Gaussian lineshape transforms to a Gaussian, and the Lorentzian lineshape transforms to the exponential. In a real experiment, the $g^{(2)}(\tau)$ function is further blurred by the jitter function of the detector which is typically Gaussian. Jitter is the term used to describe the random distribution of time delay inside the detector between a photon arriving and an electrical signal pulse being generated and it is approximately 350 ps [*]. Thus all data seen in this chapter will be fitted with an exponential form convolved with a Gaussian.

5.3 Methods

As demonstrated in chapters 3 & 4 our nano-cell design offers numerous interrogation schemes and the ability to operate high NA collection optics. The choice of excitation and collection schemes makes different phenomena visible and the right choice must be made to be able to correctly interpret the recorded data. We create an implementation of a Hanbury Brown and Twiss (HBT) interferometer [110], using two photon detectors. We collect light using off-axis fluorescence, the choice is justified later in the discussion section 5.5.1.

*Excelitas SPCM-AQRH Family datasheet, link to PDF

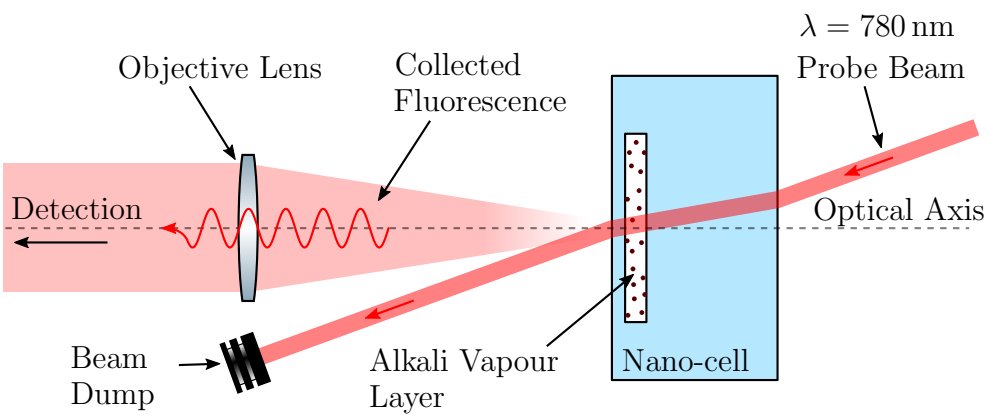

Figure 5.3: Schematic diagram depicting an implementation of off-axis fluorescence spectroscopy. The $\lambda = 780\,\mathrm{nm}$ laser is delivered at a slight angle so as to avoid the objective lens. It is clear now why this method is only available with a low NA objective. The physical size and position of the lens limits the ability to deliver an off-axis beam without conflict.

We also detail the post-processing scheme used to obtain a histogram that we claim is a valid representation of the $g^{(2)}(\tau)$ function. We highlight the reasons why such a method may not be valid and are careful to avoid these experimental limitations (e.g. detector deadtime).

5.3.1 Off-axis fluorescence

Figure 5.3 depicts the reduced optical setup for off-axis fluorescence microscopy. This is done for the simplicity of the optical setup, ease of alignment (fine positioning is less sensitive), and for potential simplicity of the computational modelling. With a beam transmitted through the nano-cell we avoid the complication of the exponentially decaying field that is characteristic of a TIRF type measurement.

A single laser beam with wavelength $\lambda = 780\,\mathrm{nm}$ (tuned to rubidium D2 line) is directed through the nano-cell at a slight angle from the detection axis.

The off-axis beam ensures that laser light cannot enter the detection optics unless via scattering with an atom. This method is also a dark background measurement and achieves an excellent signal-to-noise ratio (SNR). However, unlike the TIRF method, the laser beam now passes through 3 glass surfaces (both inner surfaces of the atom channels and the outermost front face of the nano-cell*) that can each give undesired scattering to the detection path. Furthermore, the use of low NA collection means that the acceptance area is relatively large compared to experiments done in chapter 4 and hence surface imperfections are harder to avoid by translating the nano-cell. Together these effects results in a worsened SNR but we find that the increased levels of background scatter are not a limiting factor for the presented results. Such effects would be problematic for certain experiments and we will return to this topic in the thesis outlook.

Although saturation of the atomic transitions is still a concern, the laser power can be increased for an increase in SNR and total activity. The SNR is only limited by stray laser light reaching the detector by undesired scattering e.g. from imperfections in the glass surfaces. We scan the laser across the D2 line resonances to ensure that the off-resonant activity on the detector is minimised. This ensures that the light recorded by the detectors when the laser is locked to resonance, is dominated by light scattered by atoms and not stray light. To record a $g^{(2)}(\tau)$ correlation, the beam is locked to the ^{85}Rb $F_g = 3 \rightarrow F_e = 2,3,4$ transition using polarisation spectroscopy in a separate vapour cell (see appendix A for details).

*The fourth surface at the rear of the nano-cell may also scatter, but the laser enters the glass outside of the detection mode and so does not typically contribute to the noise.

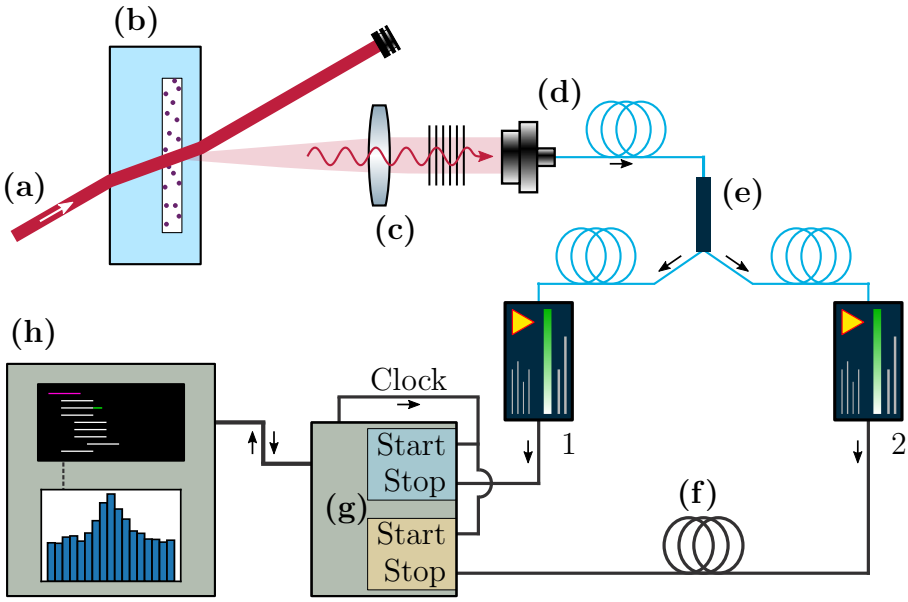

Figure 5.4: Hanbury Brown and Twiss interferometer configuration for the collection and processing of photons from the Nano-cell. A resonant laser beam (a) enters the nano-cell (b) causing excitation and fluorescence in the atomic vapour. The fluorescence is captured by an objective lens, polarisation filtered (c), and coupled into a single-mode fiber (d). The light is split by a fiber beam-splitter (e) and incident onto two avalanche photodiodes (APDs, 1 & 2). The APDs record single photon events and return an electronic TTL pulse which is fed to a time-to-digital converter (TDC, (g)), with one detector being delayed by a BNC extension (f). The delay line is purely for the convenience of post-processing and we ensure that the delay line is significantly larger than the coherence time of the light. We use two separate channels on the TDC (g) each started by a common clock cycle and stopped by an incoming TTL pulse from the corresponding APD. Therefore the TDC records a time-stamp (a.k.a. timetag) for each individual photon, maximising the available information for post-processing. The TDC is connected via USB to a computer (h) that controls the TDC and processes the returned photon timetags with Python to produce a histogram that represents the $g^{(2)}(\tau)$ function of the collected light.

5.3.2 Hanbury Brown and Twiss interferometry

In this section we detail the process by which we arrive at a histogram that approximates the $g^{(2)}(\tau)$ function. Figure 5.4 depicts the optical and electronic systems that are involved in the data recording and processing.

Fluorescence collected from the nano-cell is polarisation filtered before the fiber coupling. The polarisation filter ensures that we are only sensitive to one polarisation mode, boosting the magnitude of the correlation as the two orthogonal polarisation modes are uncorrelated*. Light is then split by a 50:50 non-polarising fiber beam splitter and incident on two detectors. The correlation of detection events between the two detectors gives us information about the $g^{(2)}(\tau)$ function.

The time-to-digital converter (TDC) returns an array of tuples to the computer with each element representing a photon detection event. The tuple contains two values, the first being the time the event was recorded relative to the start of the exposure, and the second is an integer to indicate the channel on which the event occurred. To process this timetag array we search sequentially through the array for neighbouring timetag pairs whereby the first timetag in the pair occurred on channel 1 and the second timetag occurred on channel 2. When a pair is found to satisfy this condition, the time separation of these two events is recorded. A histogram is made of all the generated time separations to display the frequency with which pair-wise events are separated. To allow us to perform a single ordered pass of the timetags†, we add a delay line to the BNC that connects detector 2 to the TDC. This effectively delays the photon detection events from that channel, adding an offset to the case for simultaneous photon detection. The delay must be larger than the coherence time of any expected feature in the $g^{(2)}(\tau)$ function, it is easy to alter and can be done with trial and error. We use a

*This was confirmed by experimentation in which the polarisation filter was removed. The resulting $g^{(2)}(\tau)$ function was halved in magnitude with all other parameters being equal. The result was reproducible regardless of the orientation of the polariser.

†We do not need to search for events where channel 2 clicks first followed by a click on channel 1. This provides a massive computational speed up.

BNC of length 10 m to add approximately 30 ns of delay*.

To avoid missed events due to detector deadtime ($\sim$ 30 ns) we keep the activity intentionally low (<100 Kcps) such that the fraction of deadtime compared to the recording time is small and the likelihood of a photon arriving whilst the detector is inactive is negligible. The BNC delay may cause the recorded photon times to become effectively reordered with events from channel 2 recording later than expected. If the BNC delay is excessive, then pair-wise subsequent photon events can be misreported as the photon arrival order can be altered in the following way. Let us consider a case where three photons are incident on the detectors at times 1 ns, 5 ns, and 20 ns arriving at detectors 1, 2, 1 respectively. We would record one pair-wise event here as an event on channel 1 is followed by an event on channel 2 (1st and 2nd events giving a separation of 4 ns). With the BNC delay (+20 ns), the event on channel 2 is delayed and hence we record 1 ns, 20 ns, and 25 ns on channels 1, 1, 2 respectively. The nearest neighbour pair-wise time is now changed to 5 ns (between the 2nd and 3rd events). This is easily corrected by also searching for next-nearest neighbour pairs and next-next-nearest neighbour pairs, etc. One can increase the order spacing between considered pair-events until all the accepted separation times are larger than the histogram span.

After some exposure time and large number of photons, we can record enough pair-wise events to record a histogram of the separation times of those pairs. This process is then repeated to produce multiple histograms each from an equal integration time. These multiple histograms can be combined to form an average and error bar for the population in each bin. This is the method used for all $g^{(2)}(\tau)$ data presented in this chapter.

*It is common to see an optical delay added to one of the fiber arms before the detectors in other similar experiments. The result is equivalent and the delay is later subtracted from the final histogram such that the $g^{(2)}(\tau)$ function is correctly centred about $\tau = 0$ ns.

5.4 Observations

We shall begin by presenting a general case of the $g^{(2)}(\tau)$ data and indicate the common features that are seen in the nano-cell. We fit to the data a function formed from a double exponential decay convolved with a Gaussian function. Later, we explore the evolution of the data as we vary the vapour density, driving intensity, and thickness of the 2D vapour layer.

Figure 5.5 shows two histograms that are representative of typical $g^{(2)}(\tau)$ data that we have observed in the nano-cell. We first observe thermal light often referred to as bunched light, or simply bunching, as one would expect from a thermal vapour [126]. This is indicated by the value of $g^{(2)}(\tau = 0)$ being larger than 1. The width of the bunching feature tells us about the coherence time of the medium and is $1 - 3\,\mathrm{ns}$. The coherence time is significantly less than the excited state lifetime ($\sim 27\,\mathrm{ns}$ [56]) and we attribute this primarily to motional dephasing. Temperatures in this range give a mean speed of atoms of $\sim 250\,\mathrm{m\,s^{-1}}$ which means an atom will move by a full wavelength (representing an effective 2π dephasing) in $\sim 3\,\mathrm{ns}$. The mean speed does not change significantly over this moderate temperature scale and hence a change in the motional dephasing mechanism cannot account for the dramatic change in the coherence time (width) of the $g^{(2)}(\tau)$ data.

5.4.1 Power dependence

The behaviour of the atomic internal state is coupled to its interaction with the environment, of which the driving light field is a constituent part. By varying the driving intensity experienced by the atoms we attempt to reveal if the short coherence time of the $g^{(2)}(\tau)$ is in fact due to a Rabi oscillation

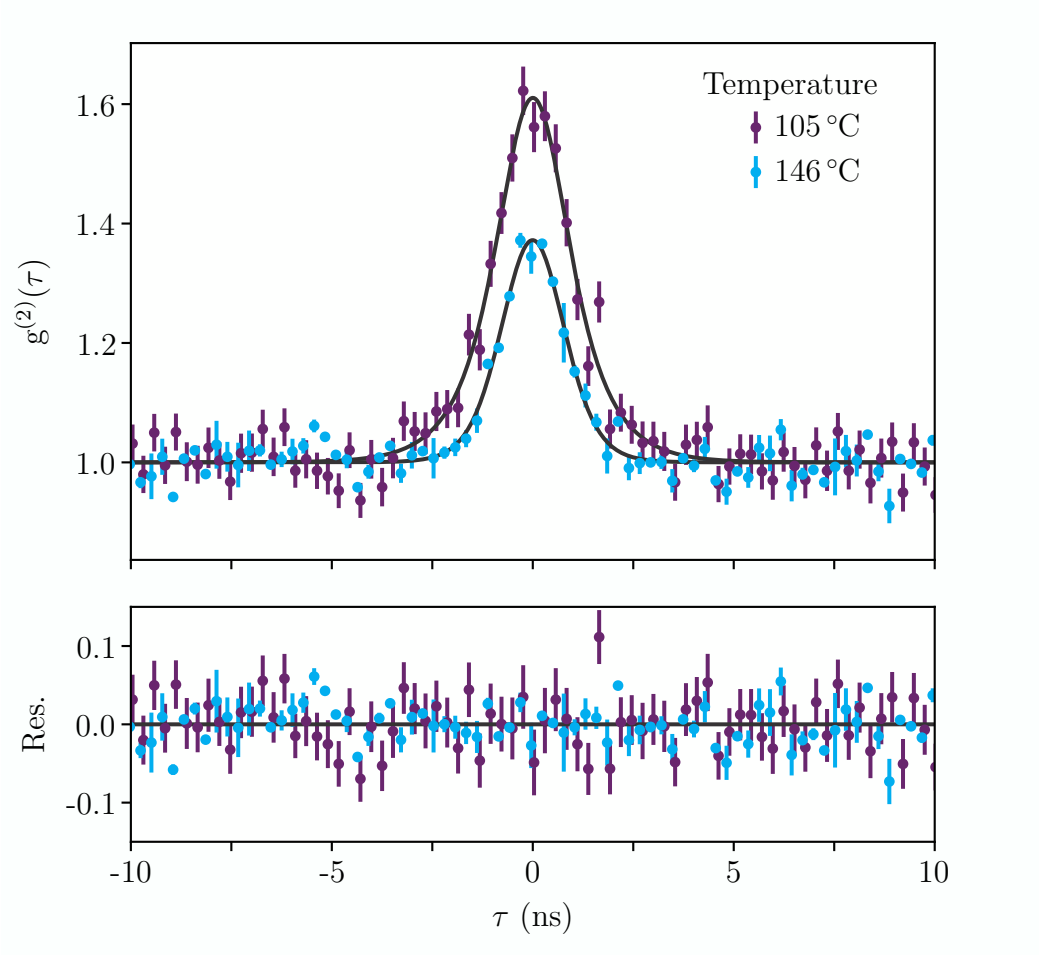

Figure 5.5: Second order temporal correlation ($g^{(2)}(\tau)$) of off-axis fluorescence recorded from a 500 nm thick vapour at 105 °C (purple) and 146 °C (cyan). Both traces are fitted with convolution between a Gaussian and double exponential decay (black line). The temperatures reported here correspond to number densities of $8 \times 10^{12}\,\mathrm{cm}^{-3}$ and $9 \times 10^{13}\,\mathrm{cm}^{-3}$ respectively. It appears that the increased number density suppresses the peak value, and the width, of the $g^{(2)}(\tau)$ function. The lack of structure in the residuals show that the fitting is good.

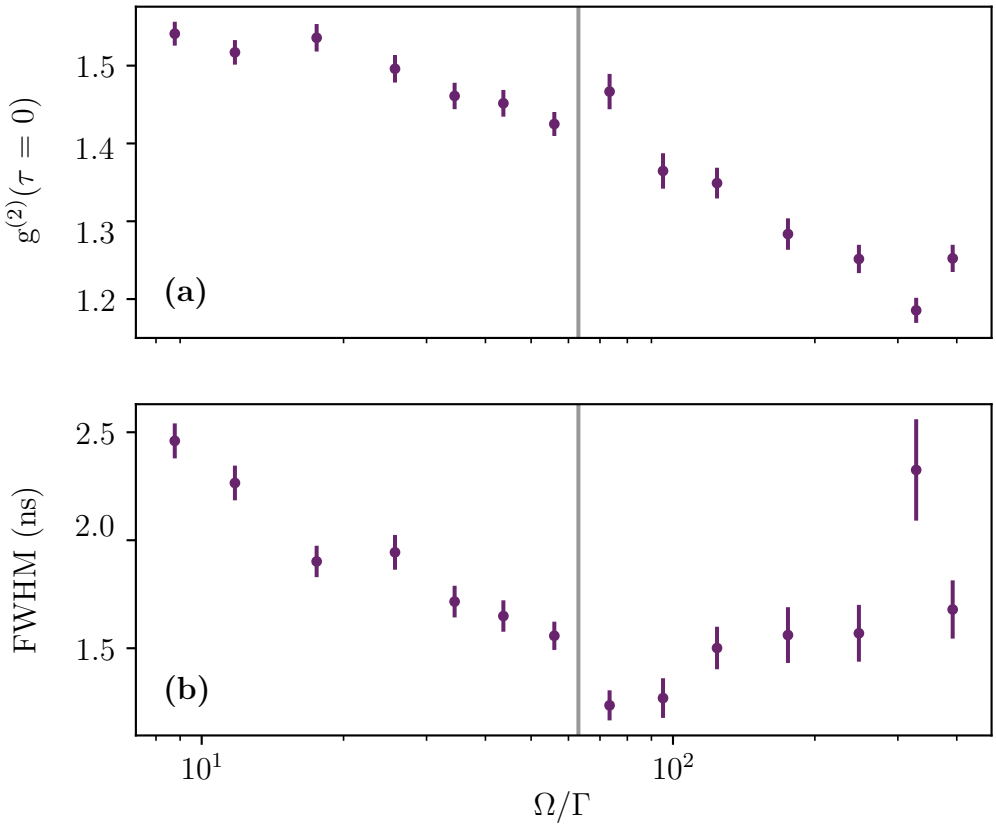

Figure 5.6: **(a)** Peak value and **(b)** full-width-half-maximum of the $g^{(2)}(\tau)$ function as a function of the scaled Rabi frequency. For driving strength to the right of the vertical black line a neutral density filter was added to the collection paths to avoid saturation of the detectors.

that is too fast to resolve above the detector jitter. A Rabi oscillation would be manifested in rapidly varying fringes in the $g^{(2)}(\tau)$ function, although our detector jitter ($\sim 350\,\text{ns}$) would effectively blur these away.

Figure 5.6 shows the trend of the peak value of $g^{(2)}(\tau = 0)$ and the full-width-half-maximum of the $g^{(2)}(\tau)$ function as the driving intensity is varied. We see that an increase in the driving intensity causes a suppression of the height and the width of the bunching feature. Intuitively this can be thought of as the laser field becoming so strong as to dominate over all other dynamics and environment effects on the atom. We therefore expect to detect an output light field that is characteristic of the input field i.e. random light from the

laser where $g^{(2)}(\tau) = 1$ for all τ.

The apparent increase in the full-width-half-maximum at higher powers where the ND filter is included (to the right of the vertical black line) is due to a failure of the fitting routine as the data becomes more noisy. In turn this gives weight to the argument that a more detailed computational model is required to capture the trend observed. The increased noise comes from shot noise as the integration time is now very low to compensate for the high count-rate on the detectors.

5.4.2 Density dependence

A primary motivation for adopting the atomic species rubidium is the wide control over number density we have via tuning the temperature of the nano-cell and its contents. We explore the evolution of the $g^{(2)}(\tau)$ function as a function of the inter-atomic spacing by heating the nano-cell in the range $90-180\,°\mathrm{C}$. As the inter-atomic spacing is varied the strength of the dipole-dipole interaction also varies rapidly with a $1/r^6$ dependence with r the inter-atomic spacing. Thus we aim to transition from a regime where the dipole-dipole interaction is negligible to a regime where it dominates the atom dynamics.

Figure 5.7 shows the evolution of the peak value and full-width-half-maximum of the $g^{(2)}(\tau)$ function as the inter-atomic spacing (temperature) is varied. As the inter-atomic spacing is reduced below $\sim 250\,\mathrm{nm}$ both the peak value and the FHWM are suppressed. We attribute this to the emergence of collective behaviour in the regime where the dipole-dipole interaction dominates over the dipole-laser or dipole-surface interaction. The atoms probed by the light field begin to act characteristically of a single emitter of which we would expect a $g^{(2)}(\tau = 0) = 0$.

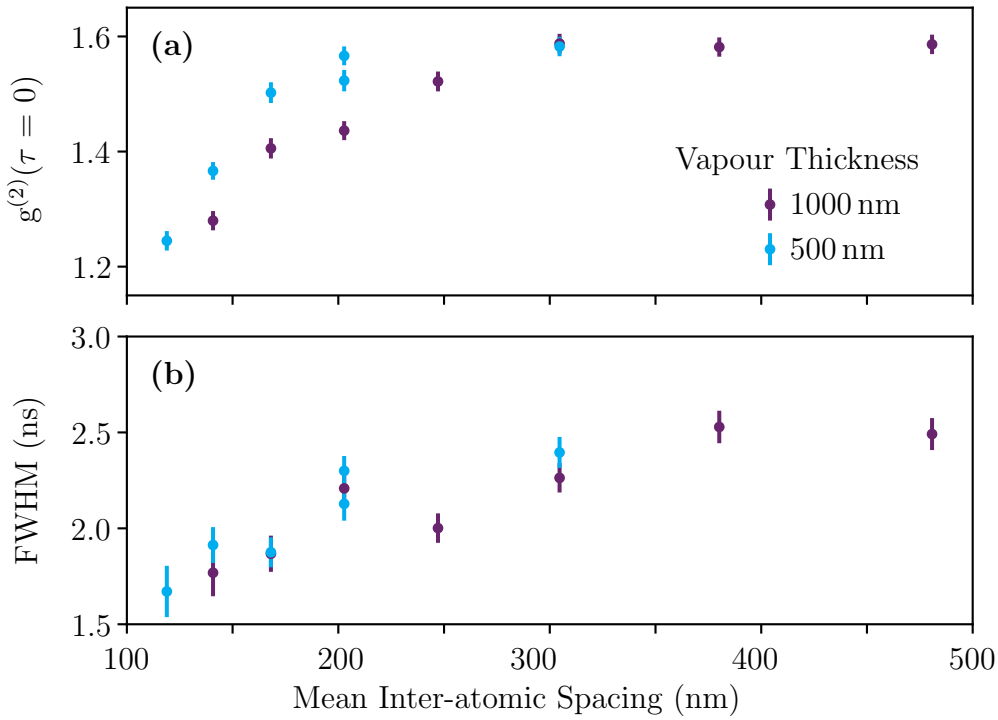

Figure 5.7: **(a)** Peak value and **(b)** full-width-half-maximum of the $g^{(2)}(\tau)$ function of the off-axis fluorescence for two vapour thicknesses either side of the probe wavelength ($\lambda = 780\,\text{nm}$). The high density vapour (lower inter-atomic separation) appears to suppress the size of the bunching feature. All data points shown here were taken with a driving strength of $\Omega/\Gamma \approx 18$.

The reduction of the FWHM may be caused by the proximity of the neighbouring dipoles which increase the decay rate (e.g. superradiance [127]) and therefore reduce coherence time. However, we know that the FWHM is already far from the natural coherence time and so we speculate that the narrowing may be caused by a more subtle effect that is not accommodated by our fitting function.

5.4.3 Vapour layer thickness dependence

The fabrication method of our nano-cell allows for a wide range of internal dimensions. The experiments in this chapter relating to the $g^{(2)}(\tau)$ function

were performed in 2D vapour layer environments and a choice of vapour thickness was readily available. The data shown in figure 5.7 includes the trends over varying vapour density for two different thicknesses, one larger than the probe wavelength (1000 nm, purple) and one thinner than the probe wavelength (500 nm, cyan).

The FWHM appears to be unaffected by the thickness change and this may suggest that the FWHM is not limited by the atom time-of-flight across the nano-cell cavity. However, we speculate that transit time effects may be influential in a further reduced geometry (e.g. 1D or '0D' channels). It is widely understood that in a thin 2D nano-cell environment the spectral response is dominated by atoms travelling parallel to the internal surfaces. These atoms have a longer interaction time with the incoming (and outgoing) light fields and hence contribute more significantly to the recorded spectral response. This velocity selection as it is known explains numerous nano-cell spectroscopy phenomena like Dicke narrowing and the sub-Doppler resolution of some spectral features. We would therefore expect the internal geometry of the nano-cell to have a significant effect on the $g^{(2)}(\tau)$ function even if such extreme structures have not been demonstrated thus far.

The peak $g^{(2)}(\tau = 0)$ value, however, does appear to show a difference between the two thicknesses. The 500 nm layer appears to maintain a higher degree of bunching as the high-density regime begins to take hold. This may be due to a subtle effect whereby the extremely thin vapour layer effectively shows fewer 'phase planes' to the detector that is positioned in the direction of the surface normal to the 2D layer. i.e. all atoms are effectively equidistant to the detector to within 500 nm (less than λ). The same condition is not met for the 1000 nm thick layer.

5.5 Discussion

5.5.1 Selection of the numerical aperture

We used the TIRF method (see section 4.2) to allow for a range of collection optics to be used without alteration of the excitation path. The choice of NA affects the spatial mode and volume from which fluorescence is effectively coupled to the detectors. In all cases presented in this chapter, we couple the light into a single-mode fiber before incidence onto the APDs. However, the collection volume and therefore the effective number of emitters varies considerably (10s to 100,000s). Whilst maintaining single-mode behaviour, the choice of objective lens then alters which mode is collected and the solid angle from which fluorescence is accepted. This may have the effect of creating a larger detector and thus averaging over any angular or spatial dependence of the $g^{(2)}(\tau)$ function. Thus it was uncertain if the objective would alter the recordings and hence a comparison was made.

Figure 5.8 shows three histograms that approximate the $g^{(2)}(\tau)$ function for various choices of the objective lens. We will later discuss the properties of the observed $g^{(2)}(\tau)$ function (height, width, etc.) but for now we will simply conclude the effect of changing NA: not much at all. We see that the profile is unchanged within the noise limit and therefore conclude that we may proceed with any choice of the available NA for further experiment. Accordingly, our choice of objective now falls to other parameters and specifically working distance and magnification are considered. We adopt a long working distance lens (f = 100 mm) for ease of alignment and the further increased optical access it provides for the probe laser beam.

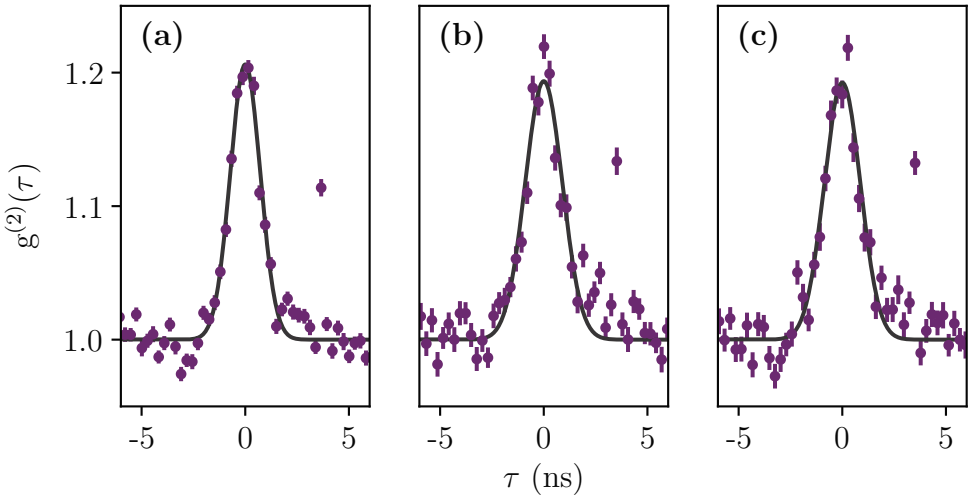

Figure 5.8: Second order temporal correlation of TIRF fluorescence for various numerical aperture [focal length] collection optics, **(a)** NA = 0.7 [f = 2 mm], **(b)** NA = 0.4 [f = 30 mm], **(c)** NA = 0.13 [f = 100 mm]. The computed histogram representing the $g^{(2)}(\tau)$ function is plotted as purple error bars and the black line is a fitted function formed of a double exponential decay convolved with a Gaussian. The function is unaffected by the change of collection optic indicating that the mode-selection of the optical fiber is limiting the spatial mode of the collection. The spurious bin seen at $\tau = 3$ ns is caused by an integer rounding error when the timetags are digitised. The computational error has been resolved in all subsequent data sets.

5.5.2 Trends of the temporal correlations

During the development of the methodology itself we looked at the influence of the choice of numerical aperture when collecting light via TIRF. We saw little difference between the choices of NA and used this as a justification for adopting the off-axis fluorescence method given the ease of implementation and potential simplification for computational modelling. The change in collection angle associated with a higher NA, and the fact that this too did not alter the $g^{(2)}(\tau)$ function in a significant way might suggest that there is no angular dependence in the system. However, with a high NA objective we collect light from a very small volume and effectively reduce the detection

volume to '0D'*. It is not possible for a '0D' system to exhibit multiple phase planes. i.e. all atoms detected are equidistant to the detector provided a sufficiently high NA collection.

The variation in nano-cell thickness appeared to indicate a difference in the evolution of the $g^{(2)}(\tau)$ function as a function of atomic density and this may be evidence of the formation of phase planes in the nano-cell. A full investigation of the angular dependence and $g^{(2)}(\tau)$ of a distributed atomic system could give further understanding of the observed phenomena. Skornia et al. [128] postulate that non-classical interference can be seen from uncorrelated atoms driven by a coherent field, and that the resulting $g^{(2)}(\tau)$ function depends strongly on the emission direction.

We saw in all cases the general shape of the $g^{(2)}(\tau)$ function was an example of bunched light, with the bunching feature having a peak value in the range $1.2 - 1.65$ and a FWHM in the range $1 - 3\,\mathrm{ns}$. This is far from the natural lifetime of the excited state. One possible explanation is motional dephasing as the timescales are consistent with the thermal velocity of the atoms. However, the thermal velocity does not change significantly over our range of explored parameters and yet the feature size does, suggesting a dependence of the $g^{(2)}(\tau)$ function on other system parameters (vapour density, driving intensity, etc.).

By varying the laser driving intensity and the atomic density we were able to move between regimes where the system is dominated by the atom-laser interaction or the dipole-dipole interaction and demonstrated the effect on the $g^{(2)}(\tau)$ function. Close scrutiny of the $g^{(2)}(\tau)$ function might offer a novel method of understanding saturation effects in an environment where more

*We use the term '0D' when all the spatial dimensions relevant to the atom system are near or below λ

traditional techniques may not be available. It is already well known that the nano-cell environment can alter the saturation intensity [3, 129].

Control of the atomic density is a topic we look at in chapter 6 and may be of great significance in advancing the study of the $g^{(2)}(\tau)$ function in the nano-cell. A combination of on demand density and observation of the $g^{(2)}(\tau)$ function may be the most promising avenue to move forwards towards obtaining an addressable single atom, which would provide great use for quantum networks, communication, and computing.

5.6 Outlook

First and foremost a theoretical investigation of the photon statistics of atoms in a nano-cell should be conducted. We have presented a number of observations with currently only intuitive explanations and not a predictive model.

Extensions of each of the experimental data sets into more simple systems could also provide the foundation steps to a full dynamical model of the photon field and its interaction with the atoms in the nano-cell*. Exploration of the parameter space in atomic density and laser intensity would allow us to remain in a regime where these effects are not necessary to include in a simulation and from there more complex dynamics could be added.

An experimental consideration that may have significance for the result and hence simulation is the idea of a uniform Rabi frequency in the nano-cell. We know that this is not physical, as in our experimentation the illumination area and accepted mode area are of similar size. Figure 5.9 shows how the

*In fact, this was the motivation for adopting the off-axis fluorescence method over TIRF. The atoms in the nano-cell now exist in a light field that is uniform in the z direction in contrast to the exponentially decaying light field produced by TIRF.

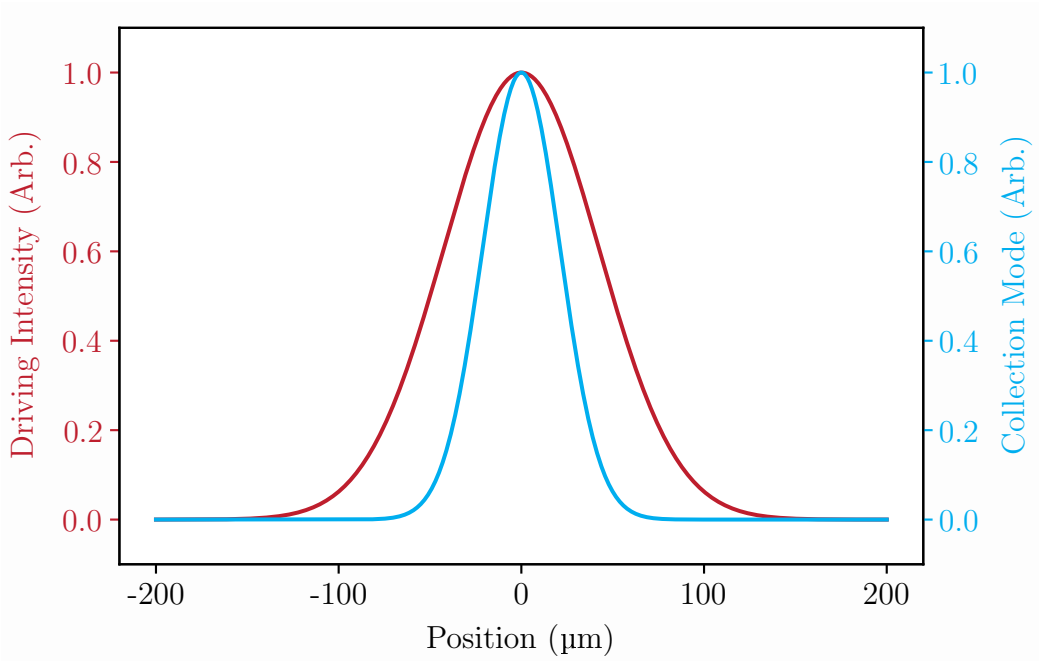

Figure 5.9: Gaussian profiles of the laser excitation spot (red) and the single mode fiber effective acceptance area (cyan) in the nano-cell. In any real experiment the excitation and detection spatial modes have finite extent, and can therefore influence the ability to resolve certain effects. In the ideal case the excitation area would be much larger than the collection area such that across the spatial extent of the detector we observe identical conditions. However, as our modes are similar in size, the detector will be sensitive to areas of the nano-cell with different Rabi frequencies and the recorded data will be a weighted sum of all these contributions across the detected spatial mode.

overlap of the excitation and detection modes can lead to a 'smearing' of the $g^{(2)}(\tau)$ function as we effectively record fluorescence from atoms that have a range of Rabi frequencies. Experimentally this can be avoided by having an excitation mode much larger than the collection mode, but this creates problems of its own e.g. laser power requirement is increased and undesired scattering is increased.

Further extensions to the $g^{(2)}(\tau)$ experiments would be to adopt the same two colour two-photon method as used in chapter 4, and perform an auto-correlation of the emitted 420 nm photons. Again, close scrutiny of the $g^{(2)}(\tau)$

function may provide knowledge of how the internal excited states of the atom behave differently to the first exited state inside the nano-cell. A ladder-type [130] and diamond-type [118] scheme have been explored but the large difference in frequency would allow for a more sensitive detection of 420 nm photons. Moreover, the different k-vectors mean a spatial mode-match is not required and spatial separation of the beams is more readily achieved. We saw a difference in the spectroscopy of the $5D_{5/2}$ state (see chapter 4) and thus it stands to reason that we might expect a different $g^{(2)}(\tau)$ function too.

Chapter 6

Spontaneous and stimulated diffusion of atoms within the nano-cell

6.1 Introduction

Much is already known about the motion and mechanical interaction of atoms and surfaces [2, 59, 62, 131]. Specifically we are concerned with alkali atoms interacting with the internal surfaces of the dielectric nano-cell, a system in which van der Waals forces [132], non-uniform velocity distributions of desorbing atoms [61, 105], bound surface states [41, 107], and surface charges [133] can occur. In such a complex environment, multiple mechanisms are at play which offers both a challenging and rewarding study.

We study the diffusion of atoms inside our nano-cell where atoms coat the internal surfaces [64] and diffuse in the vapour phase. We shall use transmission imaging to observe long time-scale temperature induced density gradients.

Light induced atomic desorption (LIAD) [134–137] is the process by which atoms are promoted from the condensed phase (typically the inner surfaces of a vapour chamber) into the vapour phase such that they may interact with probing or trapping light fields. LIAD has historically been used to boost the background vapour pressure for MOT loading [138–141] and are typically achieved with large scale illumination over timescales of seconds. In contrast, we use a tightly focused pulsed laser to achieve spatial and temporal control of the LIAD response. Such pulsed work has been reported [142], but never before in a nano-cell environment where fast control of density is most beneficial. We detect the LIAD response by changes in the selective reflection [143–146] signal.

In this chapter we explore the ability to control the atom density inside the nano-cell. We demonstrate passive control of the density by the internal structure of the nano-cell, large-scale diffusion of atoms across the nano-cell by thermal gradients, and fast localised control of the number of atoms by LIAD. Where possible we model the response of the atoms to understand the mechanism behind the recorded phenomena.

6.2 Transmission imaging

The simplest detection scheme employed in atomic vapour experiments is transmission spectroscopy. By extension, the most simple imaging method is also transmission based. By passing a resonant 780 nm laser with a large cross section (~ 5 mm waist), we illuminate the entire nano-cell and observe an absence of transmitted light where the vapour is optically thick. The weakness of this approach is that the optical thickness is reduced because

of the extremely thin vapour layers that are being probed and as such we are forced to operate the nano-cell at high temperatures near 260 °C. This temperature is enough to induce damage to the interior of the nano-cell via the chemical reaction between the alkali vapour and the glass*.

Transmission imaging reveals the spatial distribution of atomic vapour inside the 2D layer. If one were to assume uninterrupted diffusion of the vapour then the nano-cell should be evenly filled with vapour of a density that is determined by temperature. We know from long experience that it is necessary to allow nano-cells to reach equilibrium as the temperature is changed and the density of atoms is redistributed back and forth between the reservoir and the nano-channels. Thus we anticipate a gradient in the atomic density for some transient period whilst the atoms diffuse along the nano-channels. The time scale of this diffusion becomes large in the limit of a tightly confined vapour. We shall show that the atoms take some minutes to hours to fully occupy the nano-cell.

We also create an empirical model of the atomic diffusion that verifies the sticking time of atoms to the inner surfaces between successive flights. The model includes no mechanism for atoms to dwell on the inner surfaces as we show this is computationally challenging. However, a correction can be made in post-production which produces realistic dwell times.

6.2.1 Methodology

We pass a collimated 780 nm laser through the nano-cell at normal incidence to the 2D vapour layer. The beam is in the weak probe regime in order to maximise the contrast in the transmission image. To image the nano-cell

*This topic has already been discussed in chapter 3.

we use a 4f imaging system formed by two lenses and capture stills with an EMCCD. The light levels are sufficiently high that the EM module of the camera is not active and hence a similar experiment could be done with a conventional CCD or CMOS camera.

At a particular time or temperature of interest we record two images, one with a resonant laser* and one with an off-resonant laser. By subtracting the two images we reveal the atomic vapour density in the nano-cell whilst cancelling most of the interference fringes. This method also accommodates the fact that the nano-cell moves considerably, as it is mounted in a cell oven for this particular measurement.

6.2.2 Temperature induced atomic diffusion in two dimensions

Figure 6.1 shows the result of transmission imaging the nano-cell with emphasis on the 750 nm thick channel. In the first panel we see an image taken with a resonant laser that spans the entire field of view with the nano-cell at room temperature. Due to the short propagation length through the vapour the optical depth is negligible and the nano-cell appears transparent. We are able to resolve the edges of the internal nano-channels as the light diffracts from the borders of refractive index change (between glass and the evacuated channel). The fringes that span the entire image are caused by the long coherence length of the light source enabling minor reflections at the various optics in the systems to interfere. They are present even when the nano-cell is removed entirely and can be removed by calibration in post production.

*We lock to the ^{85}Rb $F_g = 3 \rightarrow F_e = 2,3,4$ for maximal absorption as described in appendix A.

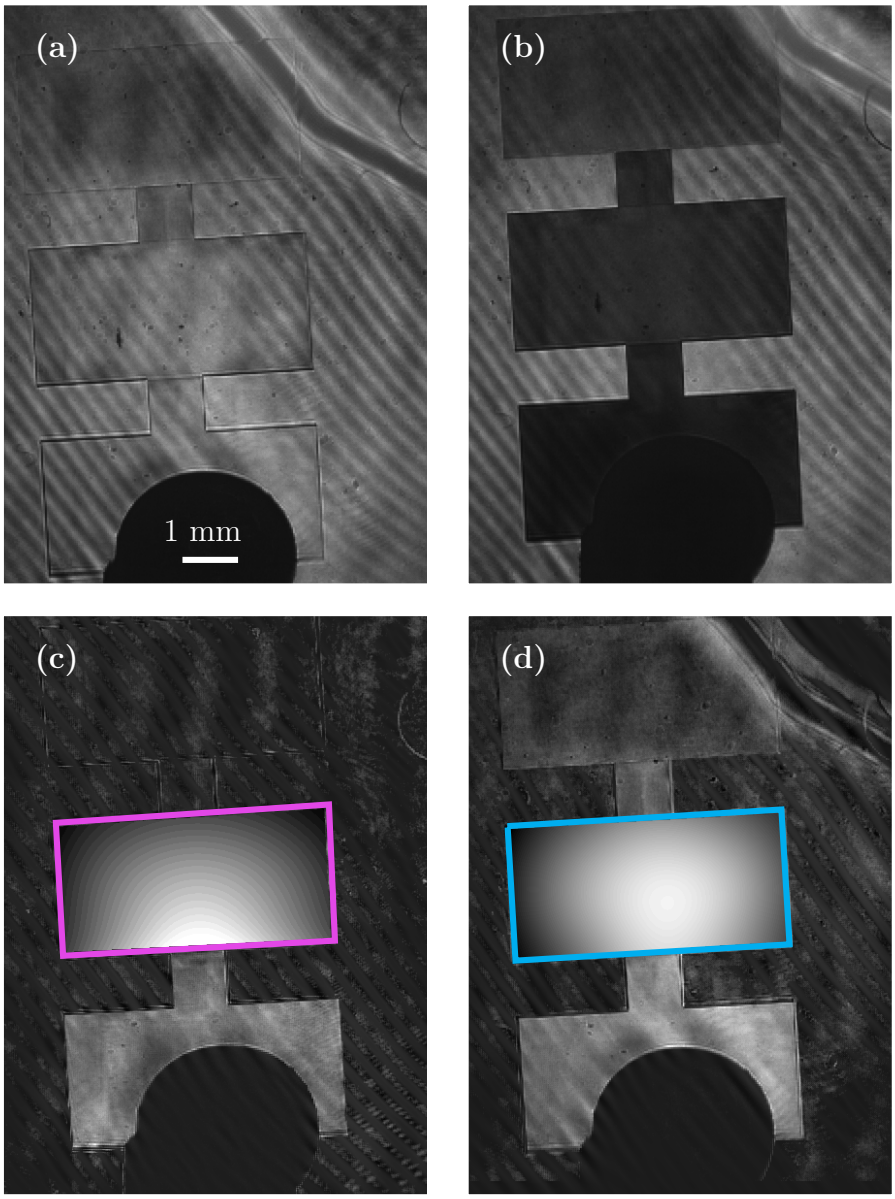

Figure 6.1: Transmission images of a three-chamber nano-cell at: **(a)** room temperature, and **(b)** 260 °C. **(c)** after 10 minutes of diffusion. The purple box highlights the 750 nm channel and the dynamic range has been enhanced by 10x for clarity. A radial gradient is seen. **(d)** after 6 hours of diffusion. The cyan box highlights the same area, now enhanced by 4x for clarity. The radial gradient has gone and instead a gradient that corresponds to the channel thickness is present, suggesting a uniform distribution of atoms.

In panel b, the cell is heated to 260 °C and now the optical thickness is evidenced by the dark shadow that fills the extent of the nano-cell. With close inspection we see that the three large rectangular channels have sequentially darker shadows from top to bottom which corresponds to the sequential thickness 500 nm, 750 nm, 1000 nm from top to bottom.

Figure 6.1c and 6.1d each show the result of the difference of two images. The result is found by taking an image with the 780 nm laser resonant and a second image with the laser non-resonant and subtracting it. The interference fringes are suppressed and the edge features of the nano-cell are also missing as they are common to both images. This isolates the change in absorption when on- and off-resonance. In addition, the 750 nm thick channel (highlighted by the coloured boxes) has been smoothed and the dynamic range enhanced (10x for panel c, 4x for panel d). Figure 6.1c shows the distribution of atoms after the nano-cell has been heated for just 10 minutes. We see that a gradient exists in the highlighted region that appears to spread out radially from the lower aperture of the channel (access from to the reservoir).

Figure 6.1d shows the distribution of atoms after the nano-cell has been heated for 6 hours. The radial pattern of absorption is now gone and the fact that the dynamic range only requires boosting by 4x suggests an overall larger quantity of atoms compared to the case after 10 minutes of heating. We still see a gradient in the absorption, but here it spans from left to right with minima in each corner of the channel. This variation corresponds to the variation in the nano-channel thickness, formed when the nano-cell is fabricated.

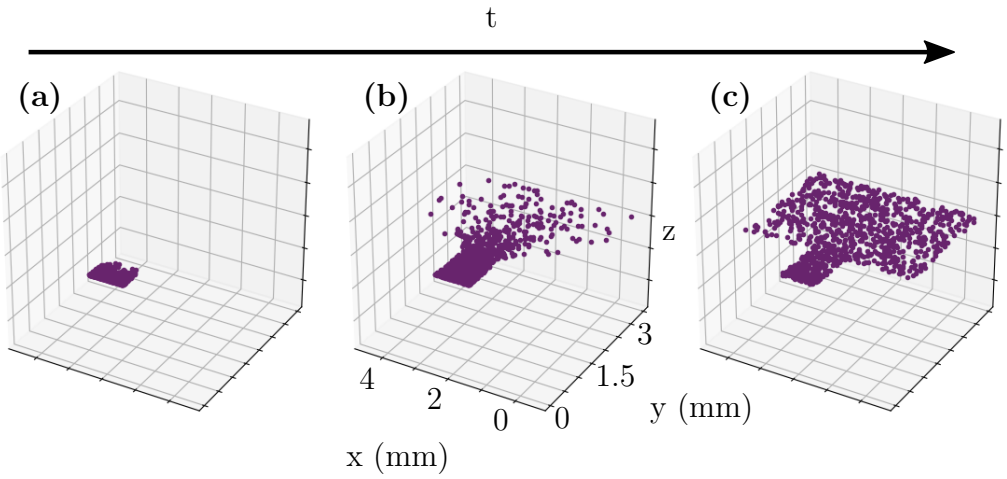

Figure 6.2: 3-dimensional ballistic simulation of atomic diffusion in a nano-cell after various evolution times: **(a)** 40 ns, **(b)** 400 ns, **(c)** 4000 ns. We see the atoms initially form a gradient distribution as they travel into the nano-channel, but have become evenly distributed after the expected time of flight given the size of the nano-channel and the atomic velocities. This timescale is faster than what we observe in experiment suggesting that elastic collisions are not occurring between the atoms and the inner surfaces of the nano-cell.

6.2.3 Ballistic modelling of atomic diffusion

Figure 6.2 shows three snap shots taken from a 3D simulation of the atom trajectories inside the nano-cell. Each atom is modelled independently and no atom-atom interactions or collective effects are considered. We model each atom as a point particle initialised with a thermal velocity. Each atom is then propagated with time steps of 10 ns. Upon collision with the internal surfaces of the nano-cell the atoms rebound elastically. The channel has width 5 mm, height 2.5 mm, and thickness 750 nm.

Despite the simplicity of the model, we do see that in the intermediate stage (Figure 6.2b) we replicate the gradient seen in experiment before reaching a uniform distribution. The simulation reaches uniformity after just 40 µs which is considerably faster than the experimental observations. It is known

that atoms in such an environment have an extended dwell time on the surfaces between successive 'flights'. The inclusion of such dwell times in the simulation becomes complex, however an approximation can be made in post-production where the run time is extended by the average dwell time multiplied by the number of atom-surface collisions that have occurred in the simulation. Given that ∼55 collisions that happen every time step, in the 4000 ns simulation shown here we have a total of ∼22000 collisions. Therefore to match the experimental timescale of some hours, an average dwell time of $\sim$ 100 µs is required. However, it can be seen that the calculation is dependent on the number of atoms in the simulation. The lack of atom-atom interactions means that the simulated diffusion speed should unaffected by the atom number, yet the collision rate of atom-surface is linearly dependent on the atom number. Therefore, the adding a finite dwell time per atom-collision to scale the duration of the simulation may give an incorrect prediction of the real system.

6.2.4 Discussion

The experimental data demonstrates that collective atomic diffusion is much slower than the mean velocity of the individual atoms. This rules out the possibility of elastic collisions between the atoms and the walls. The model demonstrates that a correction can be made by introducing a finite dwell time, whereby atoms that collide with a wall stay put for some time before entering the vapour phase again. This dwell time was required to be $\sim$ 100 µs in order to correct the time scale of the model. Additionally, the long dwell time might suggest that the atom rethermalises and hence leaves the surface with an entirely uncorrelated velocity vector from the one it arrived with. This

mechanism would further reduce the diffusion rate as the atoms would now travel laterally with motion akin to a random walk, or Levy flights. Including such mechanisms into the model becomes challenging due to the very short transit time, or average flight time, of individual atoms. The time of flight is $\sim 3\,\mathrm{ns}$ requiring a short time step of simulation to avoid atoms going out of bounds. However, the data suggests that the full time of the experiment is on the scale of minutes to hours. Thus an extremely large number of total time steps would be required for a per atom ballistic model.

An alternative method of deducing the atom dwell time (at equilibrium) is via knowledge of the vapour density and the surface density of the atoms. for example, if we have a vapour density of $9 \times 10^9\,\mathrm{cm}^{-3}$ at $20\,^\circ\mathrm{C}$, given the mean atom speed we expect $7.5 \times 10^{13}\,\mathrm{cm}^{-2}\,\mathrm{s}^{-1}$ atoms hitting the inner surface of the vapour cell. To maintain equilibrium, atoms must also be leaving the surface at this rate. If we had knowledge of the number of static atoms on the surface, the dwell time would be easily obtained. This is not the same as the quantity of condensed atoms on the surface. If one assumes a surface density of an atomic monolayer ($\sim 4 \times 10^{14}\,\mathrm{cm}^{-2}$ [65]), we would expect a dwell time of $\sim 5\,\mathrm{s}$ (ratio of monolayer density to collision rate). This is not observed in experiment, in fact little is known about the surface density of rubidium and its evolution with temperature hence the curiosity of the investigations in this chapter. A logical deduction is that the dwell time would be reduced at higher temperatures. At an increased temperature, the higher vapour pressure means that the rate of atoms colliding with the walls would be increased and therefore the rate of atoms leaving the walls must be similarly increased to maintain the vapour pressure. If the surface density was unchanged this alone would lead to a reduced dwell time. However, the equilibrium position on the phase diagram between condensed and vaporised

rubidium has also changed suggesting that if an increased atom density exists in the vapour phase, these atoms must have come from the condensed phase and hence the surface density must be reduced at higher temperatures. It then also stands to reason that LIAD experiments (as we shall soon explore) may be more successful at lower temperatures where the surface density is maximised and the contrast in vapour pressure would be most pronounced by an artificial out flux of atoms from the surface made by a laser pulse.

6.3 420 nm fluorescence microscopy

For all the benefits of employing 420 nm detection that were explored in chapter 4, we again use the same excitation and detection wavelengths here. We can separate the 420 nm fluorescence from the two infrared lasers giving an enhanced SNR. Additionally the dark background scheme allows us to operate beyond the saturation intensity for a boosted signal. We demonstrate the limit of this advantage and show evidence of an Autler-Townes splitting induced by high laser intensity.

We use independent control of the 780 nm and 776 nm beams and the high NA microscope objective to separate the focal spots requiring atoms to travel laterally between the two foci to become excited. An optical Bloch equation model predicts a spatial asymmetry in the fluorescence, however we will show the result of increasing the spot separation does not create the expected effect and speculate as to the cause of the resulting fluorescence image.

Finally, we co-locate the 780 nm and 776 nm in order to probe the in situ atomic density as we probe inside a 1D atom vapour channel.

6.3.1 Theory

We model our atom as a three-level system in which we are only able to detect population in the highest level via the decay mechanism that produces 420 nm fluorescence. We describe the atom with a 3x3 density matrix, $\hat{\rho} = \rho_{ij}$. The diagonal elements, ρ_{00}, ρ_{11}, and ρ_{22} represent the populations of each of the atomic levels respectively. We apply a Hamiltonian, $\hat{H}$, to represent the two laser fields:

$$\hat{H} = \begin{bmatrix} 0 & \Omega_{780} & 0 \\ \Omega_{780} & 0 & \Omega_{776} \\ 0 & \Omega_{776} & 0 \end{bmatrix}, \tag{6.1}$$

where Ω_{780} and Ω_{776} are the Rabi frequencies of the 780 nm and 776 nm lasers respectively. We then obtain the rate of change of density by:

$$\frac{\partial \hat{\rho}}{\partial t} = \frac{i}{\hbar}[\hat{H}, \hat{p}] - M, \tag{6.2}$$

where M is the decay matrix allowing for spontaneous decay of the excited states. Using the time derivative of $\hat{\rho}$ and multiplying by a small time step*, we can evolve the population of the three level atom in time.

Figure 6.3 shows the result of a three-level optical Bloch equation simulation where the two laser spots have been separated by 10 µm. In the simulation, an atom travels from left to right with a mean thermal velocity of 250 m s^{-1}. The atom sequentially passes through the 780 nm and then the 776 nm spot and population is transferred into the 1st and 2nd excited state respectively at each laser. The power and spatial extent of the beams use real values taken from the experiment.

*A compromise is needed as a large time step would reduce accuracy, but a small time step increases simulation time. We use a step of 1×10^{-11} s for the 200 ns simulation in figure 6.3.

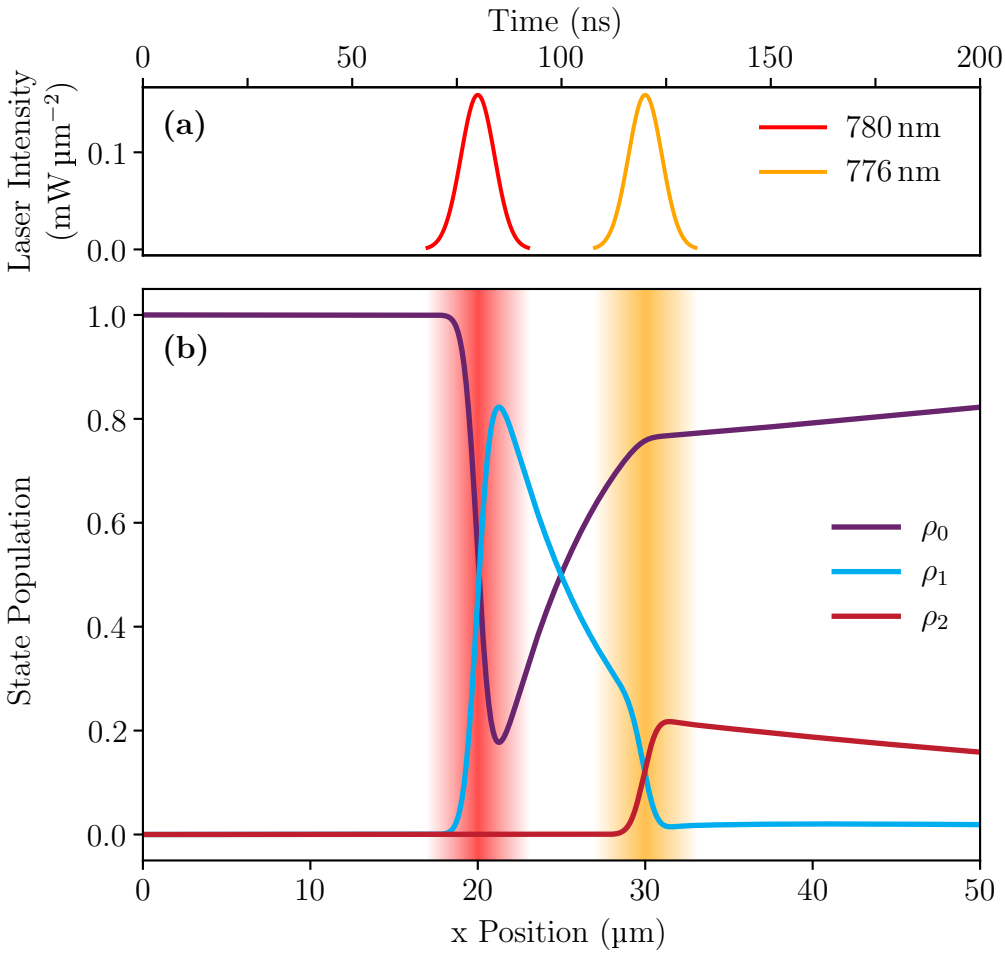

Figure 6.3: Optical Bloch equation simulation for an atom passing spatially separated laser beams. **(a)** 1 dimensional cross-section of the 780 nm and 776 nm laser spots as a function of time. **(b)** Population in each of the three-levels in the model atom as a function of position. Note that the position and time axis are directly related via the velocity of the atom which is taken to be 250 m s^{-1}, the mean thermal velocity.

An atom initialised in the ground state (ρ_0, purple line) is transferred into the 5P state (ρ_1, cyan line) by the 780 nm beam and then into the 5D state (ρ_2, red line) by the 776 nm beam. As the excitation is sequential, it is clear that if the atom direction were reversed such that it encountered the 776 nm whilst in the ground state, then no population can be transferred to the 5D state. We therefore would expect from experiment that placing two displaced beams in the configuration shown here into a layer of thermal atoms that the resulting fluorescence emission should be non-isotropic.

Simulated Raman adiabatic passage (STIRAP) could also theoretically occur if an atom was to pass through the 776 nm beam and then the 780 nm, provided the atomic velocity and spatial separation of the beams were suitable. Simulation shows that for STIRAP to occur the spatial overlap of the two laser spots, the spot widths, the atomic velocity, and the laser intensities have to be just right for the effect to be significant. Given the broad distribution in atomic velocities we expect that STIRAP would play an insignificant effect in the overall fluorescence image recorded. However, even if a STIRAP process were occurring, this would also by non-isotropic, with fluorescence being produced along a line drawn through both laser foci. We shall see in the data that there is no evidence for a non-isotropic sequential excitation of atoms by STIRAP or otherwise.

6.3.2 Methodology

Figure 6.4 depicts the method by which we are able to create independent laser foci with the two infrared beams. We use an EMCCD to create the 420 nm images in figure 6.5, but replace the camera with a photomultiplier tube to collect spectra as seen in figure 6.6.

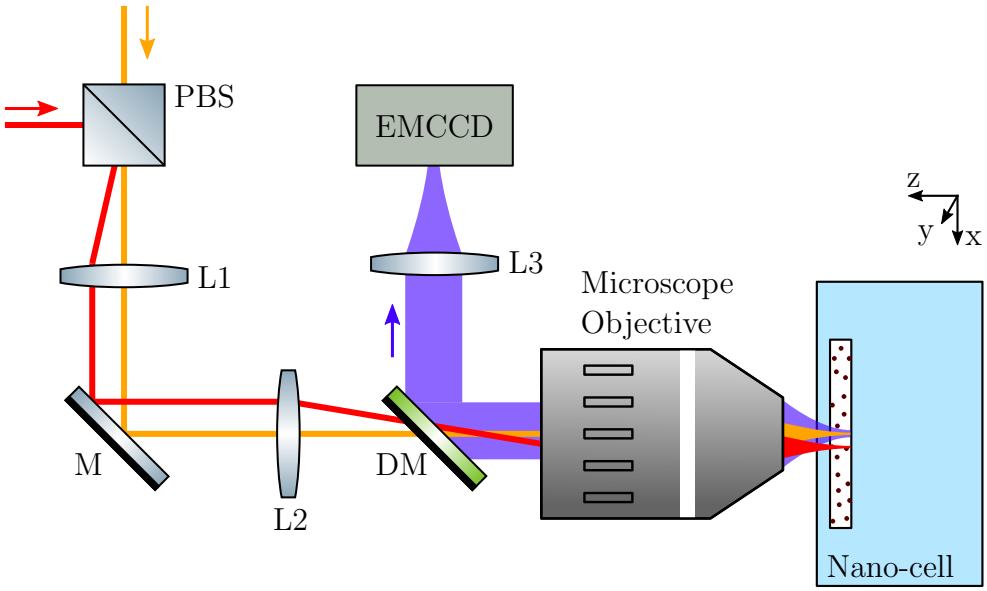

Figure 6.4: Optical table diagram for 420 nm fluorescence microscopy imaging. The 780 nm (red line) and 776 nm (orange line) lasers are combined on a polarising beam splitter (PBS) such that the are co-located on the focal plane of lens 1 (L1). The beams can be independently angled and hence the two beams are focused onto the mirror in different positions, but with parallel k-vectors. L2 and the microscope objective are placed to form a 4f imaging system such that the 780 nm and 776 nm foci formed on the mirror are then reproduced inside the nano-cell with an extreme magnification (75x in this case). The two infrared beams can be independently positioned in the nano-cell. 420 nm fluorescence from the nano-cell is then captured by the same microscope objective, separated by a dichroic mirror, and imaged onto an EMCCD. Alternatively, the EMCCD can be replaced by a photo multiplier tube which has a faster response time and can therefore be used for 420 nm fluorescence spectroscopy.

6.3.3 Spatially separated two-step excitation

Figure 6.5 shows a series of 420 nm fluorescence images from a 2D vapour of thickness 750 nm at 75 °C. The separation of the two infrared lasers is sequentially increased and an unexpected pattern emerges in the images.

Figure 6.5a shows co-located laser spots in the nano-cell and the result is a dark spot (absence of fluorescence) in the centre. We attribute this to the

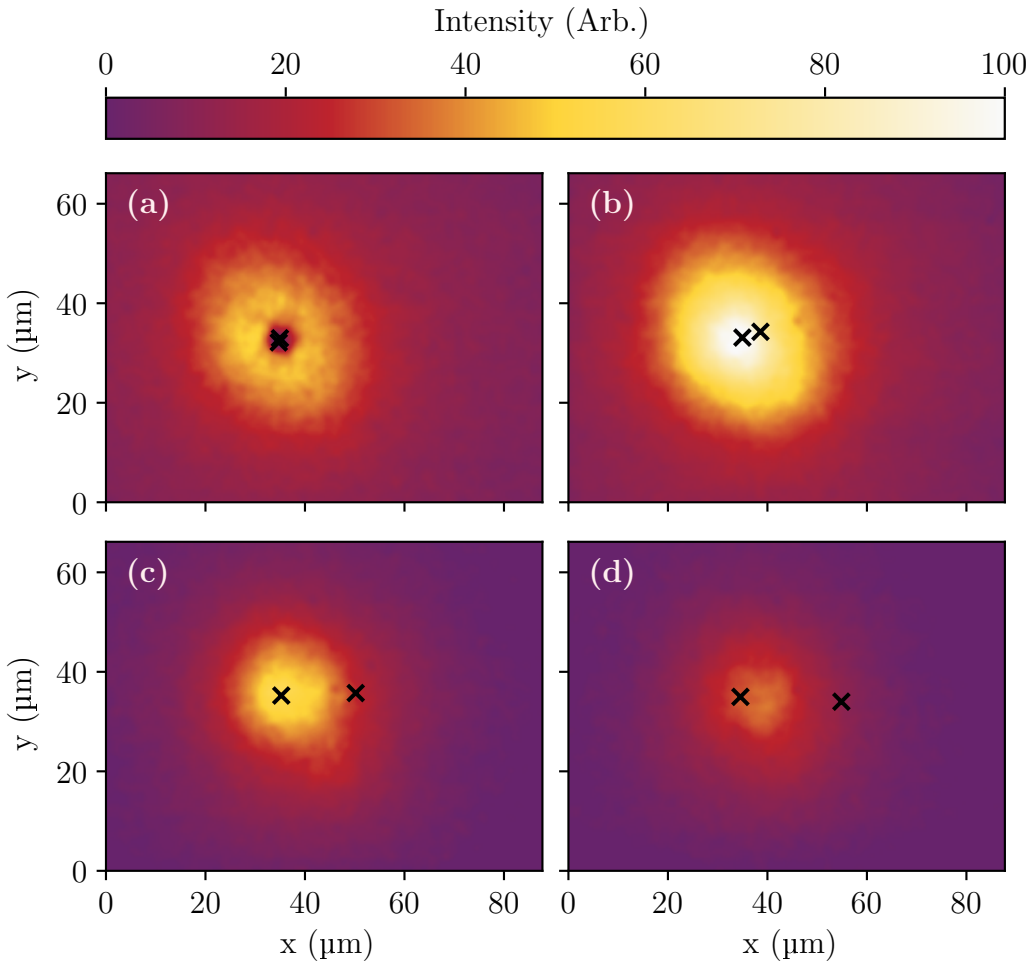

Figure 6.5: 420 nm fluorescence imaging of 750 nm thick 2D vapour with spatially separated beams. Temperature is 75 °C, each image has been scaled to fit to a common intensity axis hence relative intensity is preserved. In all four cases the locations of the foci of the two infrared beams are indicated by black crosses, the left most is the 776 nm laser spot centre and the right most is the 780 nm laser spot centre. **(a)** Laser spots are co-located. **(b)** Separation = ~ 4 µm. **(c)** Separation = ~ 15 µm. **(d)** Separation = ~ 20 µm.

large intensity causing an Autler-Townes splitting of the 5P state such that the 776 nm laser is no longer resonant with the 5P→5D transition.

With the beams separated slightly (figure 6.5b) the splitting of the 5P state is reduced around the centre of the 776 nm beam and a large amount of fluorescence can be seen. This can be explained simply by a large overlap of the intensity profile of the infrared laser spots, but with insufficient intensity to induce an Autler-Townes splitting.

As the two spots are separated further we notice a few features that provide clues to the mechanism by which fluorescence is produced. First, the fluorescence is predominantly produced from the location of the 776 nm laser (left most black cross). Second, the fluorescence appears to be isotropically distributed although the centre is shifted slightly towards the 780 nm spot (right most black cross). Together, this suggests that fluorescence is not dominated by atoms that travel sequentially from the 780 nm laser to the 776 nm laser as would be expected from our optical Bloch model. Instead, it appears that atomic diffusion is not evidenced here and that 420 nm fluorescence is being produced by atoms anywhere in the nano-cell that has a sufficient combination of 780 nm and 776 nm laser power. This is not to suggest that atoms are not propagating and being sequentially excited, only that this effect is lost against the background of the more dominant process. Ultimately the data tells us that it is the position of the atoms that determines the strength of the fluorescence rather than their velocity. To isolate the effect of atoms passing sequentially through the two beams in order to become excited to the 5D state, we would need significantly reduced laser intensity or more confined optical modes such that excitation is only possible in close proximity to each laser spot centre. The appearance of fluorescence only near the 776 nm laser

however, does suggest that atoms are excited to the 5D state at that location and the large radius of the fluorescence pattern does not match the rather short laser waist of $\approx 2\,\mu\text{m}$ which could suggest that fluorescence occurring far from the 776 nm laser spot centre is due to atoms that have been excited travelling some distance before decaying. The 5D state has a lifetime of 240 ns and the mean atomic velocity is $\sim 250\,\text{m}\,\text{s}^{-1}$ which gives a distance of $\sim 60\,\mu\text{m}$ which is consistent with the data. Corrections are likely needed to accommodate for the angular distribution of atomic velocities (not all atoms travel parallel to the walls). To summarise, an explanation for the data we see is that the 780 nm laser intensity is sufficient to populate the 5P state over a large area of the nano-cell, albeit with a spatial gradient that corresponds to the spatial mode of the light field. The 776 nm laser is only strong enough to promote atoms to the 5D state that are very close to the spot centre and from there the atoms have the 240 ns lifetime to propagate in all direction before decaying or colliding with the walls (we assume that an excited atom colliding with a wall decays non-radiatively and hence is not detected).

6.3.4 Diffusion in one dimension

By co-locating the focal spots of the infrared lasers in the nano-cell, reducing the power to avoid the Autler-Townes splitting, and replacing the EMCCD with a PMT, we are able to record localised 420 nm fluorescence spectra from the nano-cell. Moreover, by using the high NA microscope objective for focusing and collection we can select a very small probe volume to investigate and are mostly insensitive to unwanted scattering by frequency discrimination in detection. We employ these tactics to probe the fluorescence signal along a 1 dimensional channel with width of 1 µm, depth of 500 nm, and length of

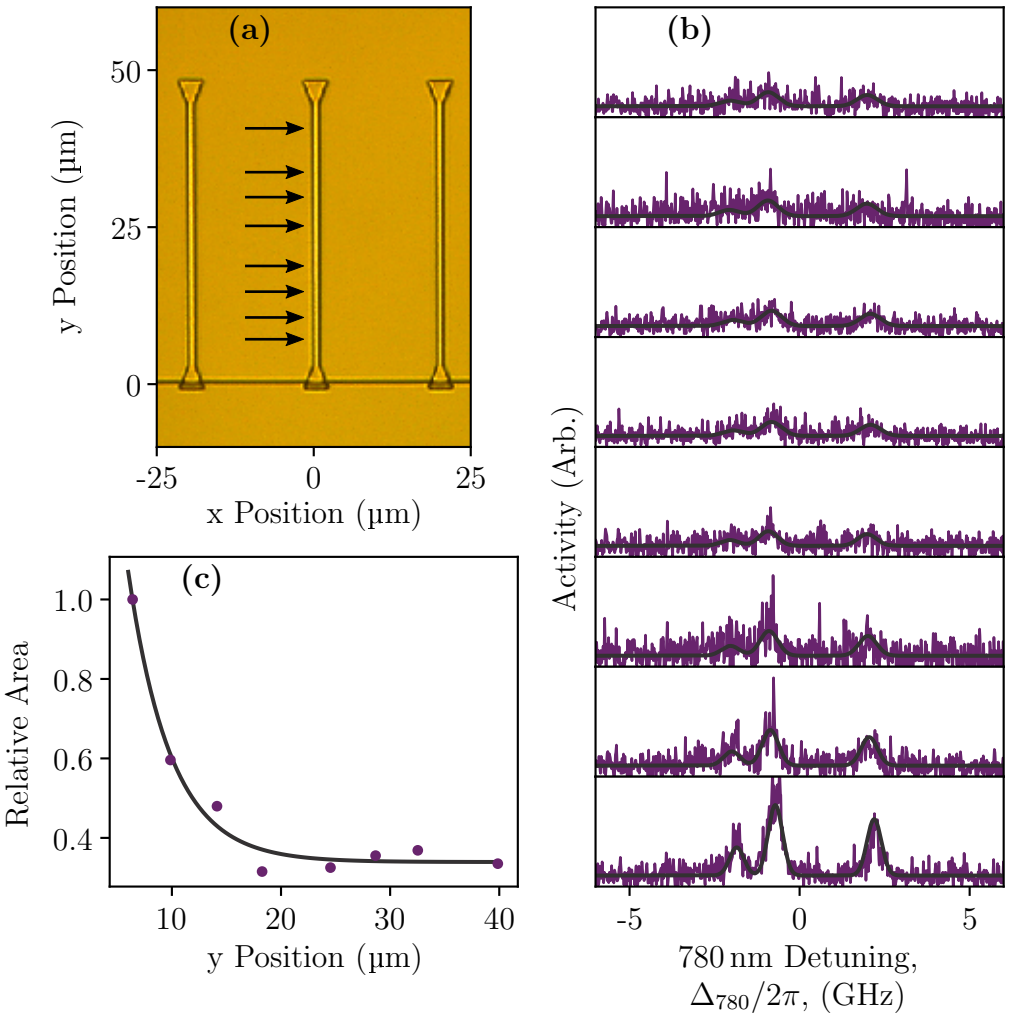

Figure 6.6: **(a)** Bright field image of a 1D channel etched into the nanocell interior. Rubidium vapour is supplied from below from the 2D region and the arrows indicate the locations where 420 nm fluorescence spectra were recorded. The channel probed here has a width of 1 µm, depth of 500 nm, and length of 50 µm. **(b)** 420 nm fluorescence spectra recorded from each of the corresponding positions indicated by the black arrows, at room temperature. The black curve fitted to each spectrum is a 4-Voigt model, although the ^{87}Rb F_g=2 transition is not present. **(c)** Extracted area under the curve for each spectrum obtained from the fitted 4-Voigt model as a function of channel position. The black line is a fitted exponential decay.

50 µm. Figure 6.6 shows the outcome.

We observe that the vapour density is not uniform along the 1D channel, but instead decays exponentially as we probe locations further from the rubidium

reservoir. This indicates that the structure alone is enough to strongly perturb the steady state density and that the vapour pressure curve relied upon for bulk vapour experiments cannot be applied to such confined geometry.

6.3.5 Discussion

Displacing the two infrared spots did not reveal evidence of sequential excitation as expected. Although the effect may well be present, it is not visible above the background fluorescence observed from atoms that effectively do not travel significant distances laterally. One solution may be to considerably reduce the beam powers such that the atomic populations are not driven by any atom that is not in very close proximity to one of the infrared laser spots.

As we suggested in chapter 4, the use of 778 nm light may be of use to allow high intensity light fields without inducing an Autler-Townes effect.

When combining the two infrared spots and investigating the atomic density along a 1D channel, we observed a strong deviation from the vapour pressure curve. This spectroscopic investigation, combined with the earlier transmission imaging shows that the diffusion of atoms is significantly slowed by the internal geometry of the nano-cell. Given the great flexibility with which we can make internal structures, it stands to reason that diffusion phenomena could be manipulated to engineer a gradient or density of the atomic vapour that is not possible elsewhere.

6.4 Light induced atomic desorption

The aim of this chapter has been to explore multiple ways in which the atomic vapour density can be engineered spatially. Further opportunities arise if we

are able to control the vapour density temporally. Heating the nano-cell or exploiting the internal structure are slow (compared to the atom internal state dynamics) or not changing at all. To gain temporal control we attempt to use LIAD in the nano-cell. LIAD is a process whereby non-resonant incident light interacts with atoms that are condensed on the inner surfaces of a vapour chamber and promotes them into the vapour phase. As the mechanism is light induced we are theoretically limited only by the temporal and spatial resolution with which we can manipulate the light source, thus offering great potential for the control of atoms in the nano-cell.

We will demonstrate one scheme of creating and detecting a LIAD response within the nano-cell. However, we will later draw on our experience in the other chapters of this thesis to conclude that many other flexible approaches to LIAD and its application can be achieved due to the design of our nano-cells.

6.4.1 Methodology

The experiments performed in this section were conducted at the Max Planck Institute for the Physics of Light in Erlangen, Germany. The data presented in figures 6.8 and 6.9 result from those experiments. Figure 6.7 shows the optical setup used for our pulsed LIAD experiments. We combine a 780 nm probe laser and a 355 nm pulsed laser with a dichroic mirror. The 780 nm beam is partially reflected by the glass-vapour interfaces inside the nano-cell. The retro-reflected 780 nm light is then collected by the microscope objective and partially reflected by a glass blank before being incident on an APD.

The 355 nm laser is used to produce a LIAD response in the nano-cell and has a pulse width of ~ 1 ns, maximal repetition rate of 1 kHz, and maximal

pulse energy of 42 µJ. We select the wavelength of 355 nm for a variety of reasons, primarily the strength of the LIAD response is greater for shorter wavelengths [139]. A further shortening of the wavelength requires optics that are not compatible with the infrared probe lasers, nor is transmitted by the fused silica of the nano-cell itself. Lastly, we consider the availability of lasers in the UV/deep blue region. A 355 nm laser is readily available by doubling and summing a 1064 nm Nd:YAG.

We choose a pulsed laser to perform LIAD such that we may resolve the dynamics of the response in the nano-cell. We know that the time of flight of thermal atoms across the nano-cell is ~ 3 ns, and the excited state lifetime for 5P is 27 ns. By operating the 355 nm laser faster than these time scales we are able to look at the response of a single pulse rather than a long term average effect. This is a crucial step towards creating an on-demand single atom or array of atoms. As we have seen in chapter 5, the long term average of our thermal system produces thermal light, hence we must operate faster than the system dynamics to achieve true single emitter control.

Figure 6.8 shows a spectrum recorded by selective reflection for a hot (160 ° °C) vapour layer in the absence of any LIAD effects. We see a dispersive shaped response as the 780 nm probe laser is scanned across the D2 line. At room temperature (low atom density) there would be no observable spectral signature, just a constant 3% reflection. This contrast in response between high and low density is the signature we use to identify a LIAD event. The maximal contrast is achieved near the ^{85}Rb $F_g = 3 \rightarrow F_e = 2,3,4$ resonance and is marked with a vertical purple line. By locking the 780 nm laser to this frequency, an increase in the atomic vapour density will be evidenced by a reduction in the recorded reflection intensity. Additionally, any scattered

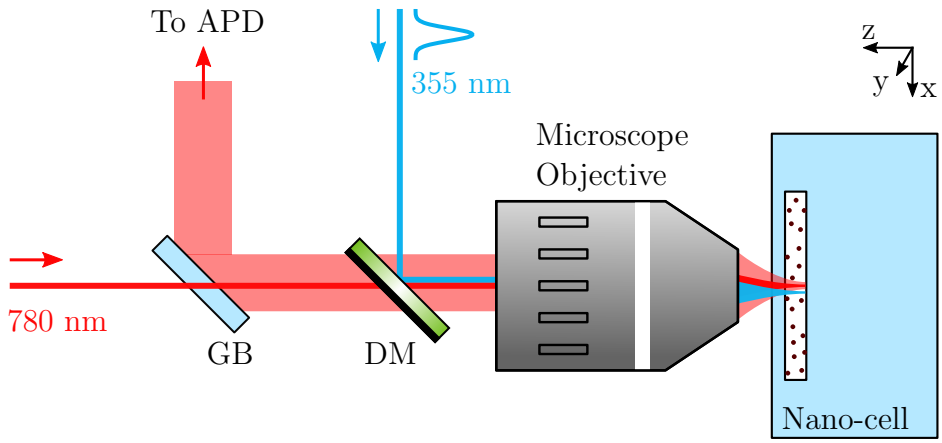

Figure 6.7: Optical setup schematic for pulsed LIAD experiments. APD: avalanche photodiode, GB: glass blank, DM: dichroic mirror. The 780 nm probe beam is focused into the nano-cell by the microscope objective. The retro-reflection from the internal surfaces of the vapour channel is partially reflected by a glass blank and then recorded by an APD. A dichroic mirror is used to bring the 355 nm pulses into the nano-cell coaxially with the 780 nm beam.

light from the 355 nm pulse will contribute additional counts, thus the only mechanism by which the recorded reflection activity can be reduced is by a presence of atoms in the nano-cell. The measurement is limited in the same fashion as transmission spectroscopy in that it is bright background and can be saturated with excess power, but the background is now just a 3% reflection rather than the transmitted beam, which boosts contrast by ∼30x compared to transmission spectroscopy.

To record the spectrum in figure 6.8, and for laser locking when performing LIAD, the 780 nm probe laser is locked to a tunable high finesse cavity. The cavity is stabilised to a wavemeter.

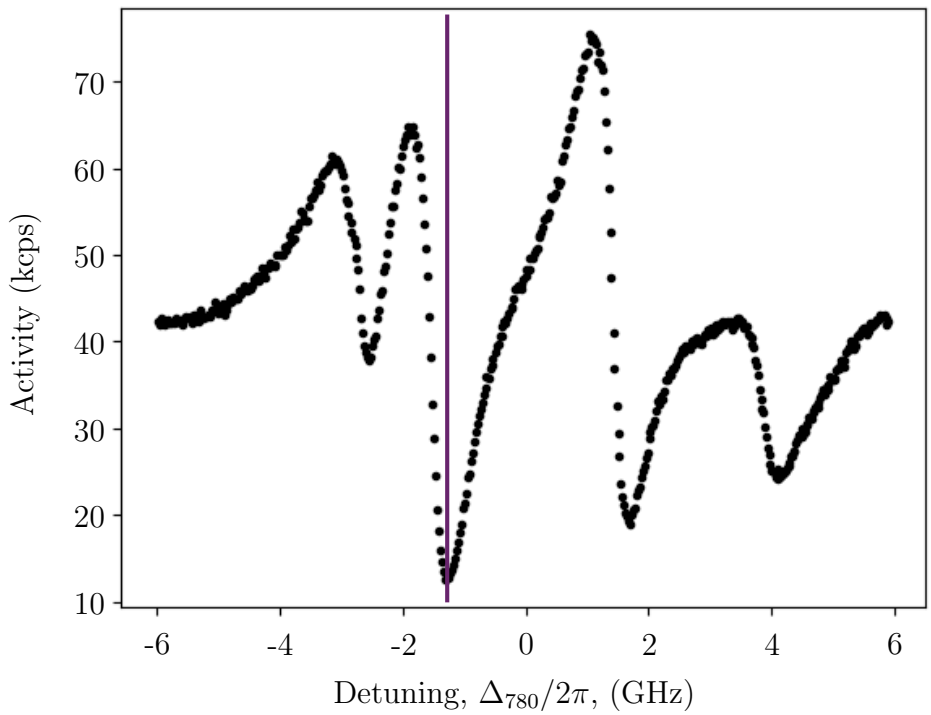

Figure 6.8: Reflection spectroscopy of 2D thermal vapour at 160 °C, thickness 1 µm. As the 780 nm laser is scanned over the D2 line the reflection coefficient at the glass-vapour interface changes due to the change in refractive index of the atomic vapour. During a LIAD experiment, the 780 nm laser is locked to the minimum of the ^{85}Rb $F_g = 3 \rightarrow F_e = 2,3,4$ dispersion (vertical purple line), for maximal contrast.

6.4.2 Observations

Figure 6.9 shows a histogram of photon counts accumulated over 90,000 pulses, in a room temperature nano-cell. After the incident 355 nm pulse at time = 0 ns the reflection signal drops to below 10 kcps, a greater contrast than what was seen in figure 6.8. The dip indicated that the atomic density changes from $n = 1 \times 10^{10}\,\mathrm{cm}^{-3}$ (room temperature steady state) to in excess of $n = 1 \times 10^{15}\,\mathrm{cm}^{-3}$ in a few nanoseconds following the 355 nm pulse. The probe volume is of the order of 1 µm^3 suggesting a total of $\sim$ 1000 atoms

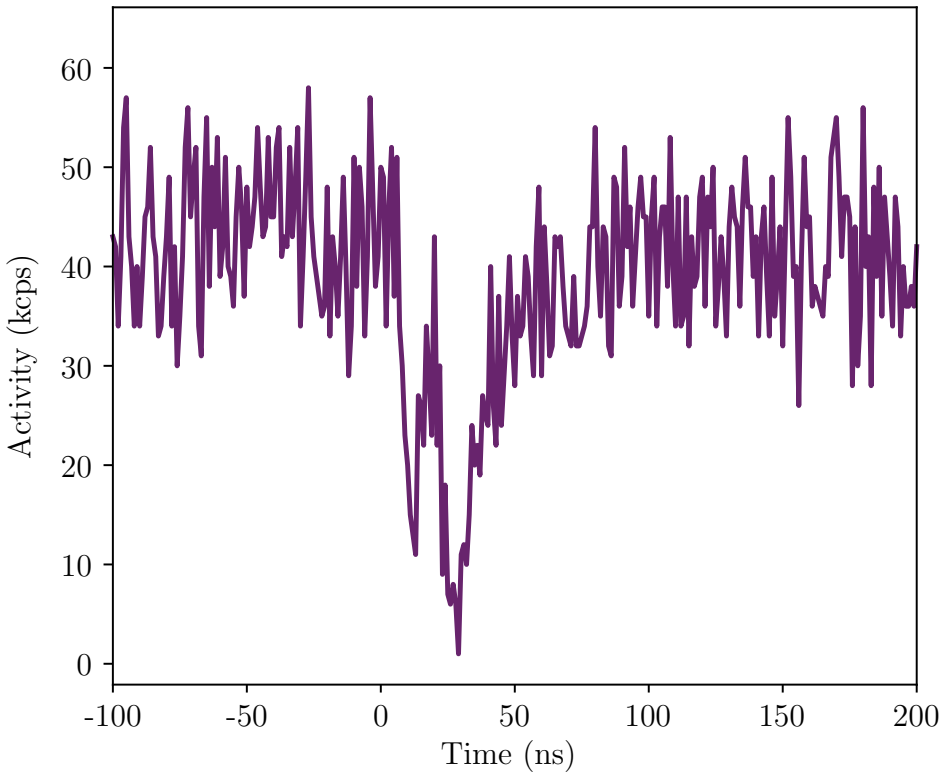

Figure 6.9: Light induced atomic desorption in 2D layer of thickness 1 µm at room temperature. The trace shown here is a histogram of photon counts accumulated over 90,000 separate pulsed LIAD events. The $\sim$ 1 ns 355 nm pulse is incident on the nano-cell at approximately 0 ns. After the 355 nm pulse we see that the background level of signal is reduced for a period of $\sim$ 100 ns before returning to the steady state level.

are promoted from the inner surfaces of the nano-cell during each 355 nm pulse. This is consistent with the response reported by Petrov [142]. The surface density of condensed rubidium reported by Kitagami [65] is again consistent with the quantity of atoms available to be released to the vapour phase.

The large number of repeated pulses is a requirement set by the temporal resolution of the histogram (such that each bin is well populated) and the maximum sustained activity that can be achieved on the APD*.

*For example, say we wish to have 100 photons per bin (such that error is $\sqrt{100} = 10$ per bin), and timing resolution of 1 ns. At the maximum activity of the APD (1 MHz) a

6.4.3 Discussion

Figure 6.9 also shows that the reflection intensity does not return to normal levels until $\sim$ 100 ns after the 355 nm pulse. The cause of this long time scale is not presently known. The transit time of $\sim$ 3 ns would suggest that the atoms created by LIAD are either not travelling between the walls and adsorbing again on contact, do not have a typical thermal velocity, or are perhaps diffusing laterally out of the detection area and hence have a longer time of interaction with the 780 nm probe beam. By fitting an exponential to the tail of the LIAD dip ($30 - 100$ ns) we extract a time constant of 13 ns which is much longer than the transit time between walls, but shorter than any excited state lifetime, suggesting that some other mechanism is responsible.

Additionally, the origin of the double dip structure is not known. Further experimentation and modelling is required to understand the many mechanisms at play when performing pulsed LIAD in a nano-cell.

6.5 Conclusion and outlook

In this chapter we have explored some means to manipulate the atomic density of a thermal vapour. To have a greater degree of control over the number, position, and velocity of individual atoms offers the possibility of creating scalable quantum devices that rely on the atom-light interaction. We have demonstrated passive control by changing the atomic density with novel internal structure and geometry. Thermal diffusion and temperature gradients

single shot of the experiment would register an average bin population of 0.001 photons. Thus we require 100,000 experimental shots to achieve a significant bin population, and hence overcome the shot noise.

have been seen to cause a density gradient. Lastly, we used LIAD to show a fast and localised control of the atom number in the nano-cell.

We propose that LIAD offers the most promising avenue of exploration for manipulating the atom density. This is due to the fact that light is more readily controlled and localised than temperature or internal etched structures. We suggest that alternative detection methods, for example two-photon TIRF, could offer a more sensitive and reliable detection scheme for future LIAD work. Boosting the signal strength and the reducing the number of pulse events required to populate a histogram would also reduce the risk of surface depletion.

We speculate that localised heating may still have potential for use in the nano-cell. Delivery of localised heat may be achieved with a focused CO_2 laser, but is limited by the thickness of the glass. Alternatively, heated plasmonic nano-particles to boost vapour pressure [147] have been demonstrated and such nano-particles could be included in the fabrication of future nano-cells.

We have demonstrated the fabrication of alkali nanocells with very small internal geometry. The goal of the work is to progress towards individual atom control with the potential to isolate a single atom in such a nano-cell. This could be used, for example, as a single emitter or scaled to an array of emitters. Either by lattice structure of the nano-cell internal geometry or by structured LIAD light beams, one could produce a switchable on-demand array of single atoms.

Chapter 7

Summary and Outlook

In this thesis we have shown that the design and production of a new type of alkali vapour nano-cell could allow advancements in the study of atomic physics. We have demonstrated a number of both fundamental and applied studies. We have shown experimental data and computational models that indicate the limits of our understanding, further highlighting how our nano-cells open up new questions for atomic systems. We will now provide a recommendation for the future lines of studies for each diverging path of research and ultimately how these may combine to produce new quantum technology.

7.1 Spectroscopy

As demonstrated in chapter 2 & 4, the lineshape of the atomic resonances tell us a great deal about the behaviour of atoms as individuals and as a collective. Information about the velocity distribution and excited state lifetimes can be inferred from the spectral profile. Within the nano-cell environment we also encounter the effects of the atom-surface interaction which effectively gives

some positional information about the atoms. Furthermore, by using the TIRF method we can enhance our sensitivity to the atoms closest to the surface as well as performing velocity selective measurements. When expanding the spectroscopy work to include 2-photon excitation we saw some novel features, and also benefited from Doppler cancellation of the counter propagating beams. As has been done in other atomic systems, we propose that careful modelling of the fluorescence spectra will reveal detailed information about the spatial and velocity distribution of the atoms within the nano-cell and other nano-scale geometries that are yet to be produced in the platform. The most promising advancement is to use 778 nm photons to perform a single colour 2-photon excitation in rubidium, as described in the outlook section of chapter 4. By separating the multiple phenomena observed in figure 4.4 we stand a better chance of understanding and modelling the atomic response and therefore extracting useful information.

It is postulated that a repulsive interaction may exist between certain alkali metals and dielectric materials [107]. This may be manifested in the spectral signature as a strong asymmetry to the blue side of resonance. If found, such an effect could be used to 'trap' atoms between the close internal surfaces of the nano-cell thus enhancing the interaction time and potentially altering diffusion.

7.2 Temporal correlations

Chapter 5 explored the photon statistics of light coming from atoms fluorescing in the nano-cell. We initially hoped that the low temperature and low detection volume would result in the collection of light from very few emit-

ters (ideally 1), and thus we would see anti-bunched light. However, we saw thermal light in all cases and this was most likely due to the timescales by which atoms enter and leave our detection volume being much faster that the rate at which photons can be extracted from a single emitter. Nevertheless, a study of the photon statistics gives us information about the dynamics of the system at very short timescales, which is typically unavailable in spectroscopic methods due to the required integration times (for spectra). We propose that the photon statistics should be continually monitored in all cases as the implementation is relatively easy and compatible with the other optical techniques used.

Additionally, we will soon combine the sections of this thesis to propose a viable method to achieve single atom control in the nano-cell. Temporal correlations will be necessary evidence to confirm that a single atom has been isolated.

7.3 Light induced atomic desorption

Of the work done to document and understand diffusion of atoms in chapter 6, LIAD offers the most potential for manipulating the atomic density. Being the most flexible in terms of time scale and spatial extent, the control of the atoms via non-resonant light is a vast improvement over control via temperature. Further work is needed to quantify the LIAD response and adoption of the sensitive detection techniques used in the other chapters should be useful for this.

It has been reported that at low intensities that LIAD behaves in an analogous way to the photoelectric effect [78]. It then stands to reason that with a

precise control of the LIAD effect a single atom could be liberated from the surface on demand. Perhaps a greater understanding of the LIAD effect could also be used to prevent atoms from sticking to the surfaces at all. This could act as a trapping mechanism whereby the atoms are continually repelled away from the inner surfaces of the nano-cell.

Ultimately, the highest contrast when performing a LIAD experiment comes from having a low background vapour pressure such that an atomic response is only observed from the desorbed atoms. As such, cryogenic cooling of the nano-cell may allow us to explore a system where there are no spontaneously occurring atoms, and only those stimulated into the vapour phase by LIAD are available for interaction with a light field. This could lead to a switchable on-demand optical response, in effect a photon-photon interaction mediated though an atomic ensemble.

7.4 Internal structure design advancements

The core of the thesis is the nano-cell design. We have seen a number of scientific results and suggested future works to be done using them. The existing structures already show the promise of new findings. However, there is no reason that the nano-cell design should not continue in its development. Internal structures can be elaborated and the fabrication method is also compatible with the growth of waveguiding materials. Even within the confines of the current fabrication methods, we propose new structures that might realise scalable quantum atomic systems.

Figure 7.1 shows structures made in the latest generation of nano-cells with the inclusion of '0D' pockets. The pockets are small volumes of $\sim 1\,\mu\text{m}$ in

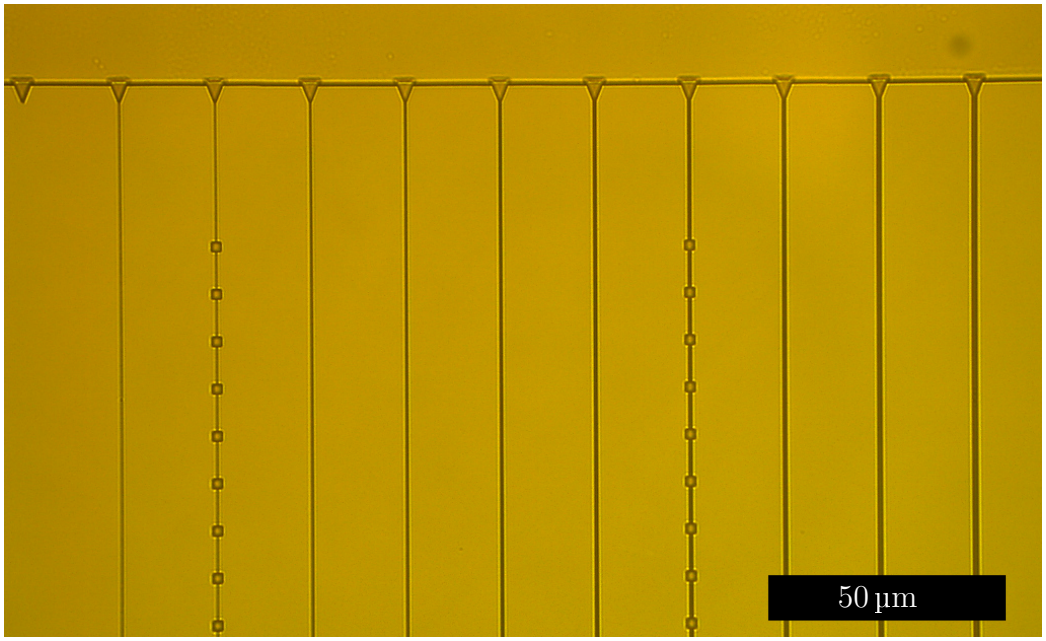

Figure 7.1: Image of '0D' structures in the nano-cell. In the latest generation of nano-cells, the thinnest channels include a series of chambers. These chambers can be fabricated such that all dimensions are less than λ. We refer to this as zero-dimensional. It is a clear extension then that a 2D lattice may also be fabricated. Per-site resolution and addressing these pockets individually will be a new challenge for the experiment, but the robust nature of thermal vapour cells, and specifically our own nano-cells, makes the route still more simple than cold atom counter parts. One could reasonably predict that this platform could be modified to produce an array of pockets with each pocket containing a single atom and in which neighbours may communicate by exchanging photons. We propose our nano-cell to be a novel platform for quantum information protocols.

all three dimensions, placed at intervals along a 1D channel. All the length scales here are customisable and so chains of atom pockets or 2D lattices can be made. Work has yet to be done inside such structures, but we propose that with LIAD and induced diffusion, the sites could be populated with atoms. Additionally, the vapour pressure of each pocket could be controlled individually with LIAD with per-site resolution of the desorbing laser light. Thus an array of coupled quantum emitters could be made possible for the first in the domain of thermal alkali vapours.

7.5 On-demand atomic lattice

Combining all the elements of this thesis to a single applied goal could result in a controlled lattice of quantum emitters. By etching a pattern of '0D' pockets into the nano-cell we achieve the essential backbone of the lattice structure. Spontaneous and stimulated diffusion by heat or by LIAD could be used to fill the pockets with atoms from the reservoir. Each pocket would have some equilibrium of atoms condensed onto the inner surfaces (i.e. unavailable for interaction) and in the vapour phase (i.e. available for interaction). Spectroscopy would confirm the occupancy of the sites and provide insight into the spatial and velocity distribution of the atoms within. Finally, precise control of the occupancy of each site could be adjusted using the LIAD effect. This would result in an array of quantum emitters in which the site occupancy could be changed during the operation of the lattice, a feature not present in cold atom systems.

Considerations could also be made for the material used, as the dielectric response plays an important role in the behaviour of atoms near a surface. Additionally, light guiding modes could be added between sights by the deposition of high refractive index material. Such structures are commonplace in guided light experiments, although we have not yet attempted to grow them specifically in our nano-cells.

7.6 Closing remarks

In summary, we have designed and developed a new generation of atomic vapour nano-cells. We have demonstrated numerous areas where the design

allows us to study fundamental physics and reveal novel phenomena. Using spectroscopy we have shown how the greater optical access allows us to use TIRF, in order to be highly sensitive to atom-surface interactions. Previously unseen structure in the fluorescence spectra gives us new information about the spatial and velocity distributions of the atoms. Temporal correlation of the fluorescent light has shown us the quantum nature of the light and hence the atomic system from which it originated. We have speculated as to the cause of the observed trends as a function of laser intensity and atomic vapour pressure. Finally, we showed how the diffusion of atoms within the nano-cell is modified by the very nature of the environment and how the density could be manipulated and controlled with LIAD.

We believe that our new nano-cell design demonstrates a significant advancement of the atomic physics research field, by opening multiple avenues of investigation and offering a promising platform for quantum technologies.

Appendix A

780 nm laser calibration, normalisation, and locking

In the laboratory our detectors are not typically able to detect the frequency of the recorded light. Photodiodes return a voltage, photon counters give TTL pulses, and EMCCDs return an accumulated charge, and all of these devices return these signals as a function of time. Therefore, a degree of post-processing is necessary to convert the raw recorded data into a more universal format, namely the frequency domain. This is done with an atomic frequency reference where well-documented (and narrow) spectral features are produced that allow a conversion from the time domain of the detector recordings into the frequency domain of the laser. It is also necessary to compensate for the power drift of the laser whereby the output beam power depends on the lasing wavelength and hence varies across a typical $2\pi \times 10\,\mathrm{GHz}$ scan range.

In this appendix we will show the optical table setup used that allows a number of key operational modes. We will use saturated spectroscopy as the frequency reference when producing spectra by scanning a laser. Transmission spectroscopy is used to normalise the laser output power. Finally, the same

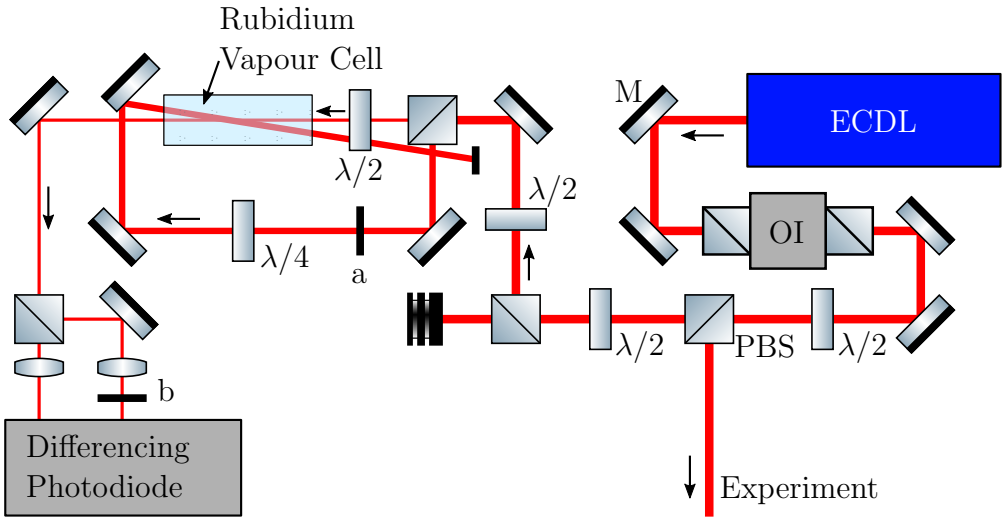

Figure A.1: M: Mirror, PBS: Polarising beam splitter, $\lambda/2$: half-wave plate, $\lambda/4$: quarter-wave plate. Partial optical table diagram showing the external cavity diode laser (ECDL) and frequency reference (for rubidium D2 line). A 75 mm natural abundance rubidium vapour cell is probed by a weak fraction of the laser beam. The operation of the setup can be changed by the inclusion/exclusion of beam blocks at sites marked 'a' and 'b'. With both blocks present, we record transmission spectroscopy; with beam block at 'a' removed we see saturated absorption spectroscopy by optically pumping the vapour. By removing both beam blocks we obtain an error signal that can be used to lock the laser.

setup can be used to frequency stabilise (lock) the 780 nm laser.

Figure A.1 shows the optical table setup for the frequency reference section of the experiment. The half-wave plate before the vapour cell prepares the probe beam with a 45° linear polarisation. The addition or removal of beam blocks at the locations 'a' and 'b' in the figure allow the frequency reference to act in different ways depending on the required purpose. With a beam block present at both 'a' and 'b', we reduce the system to a single beam and single photodiode and are able to record a transmission spectrum from the 75 mm vapour cell. If the beam block at 'a' is removed, then the vapour is pumped by the counter-propagating beam and we observe a saturated-absorption spectrum that can be used for fine resolution frequency calibration. By removing

the beam block at 'b' we independently record the transmission of the two orthogonal light polarisation modes through the vapour. By taking the difference, we are then sensitive to the dichroism of the vapour. The presence of the quarter-wave plate in the counter-propagating pump beam induces a dichroism in the vapour by optical hyperfine pumping. The dichroism produces a sharp error signal that can be used in a feedback loop to stabilise the laser to the atomic signal (laser locking).

A.1 Power normalisation

Figure A.2 shows how the laser power drift can be compensated by extrapolating a polynomial fit to the off-resonant parts of the spectrum. The laser is scanned across the D2 line and we observe the characteristic Doppler-broadened absorption lines of each of the two ground states and of each of the two isotopes. We also observe that the entire trace is on a sloping background and this caused by a common occurrence in ECDL systems whereby the laser output power varies as the lasing frequency is scanned. This is easily compensated for in post-production. We select the non-resonant portions of the trace (highlighted in cyan) and fit a 5th order polynomial* (grey line) that approximates the transmission in the absence of any atoms. We then divide the original data set by the fitted polynomial and we recover the trace plotted in Figure A.2b. We note that this single point-to-point re-normalisation is only valid is the photodiode response is zero in the absence of any laser light. The normalisation can also be applied in an identical way to a saturated spectroscopy trace.

*The exact form of the power drift is not known, a polynomial is chosen for simplicity and the order is made sufficiently high to make a reasonable fit.

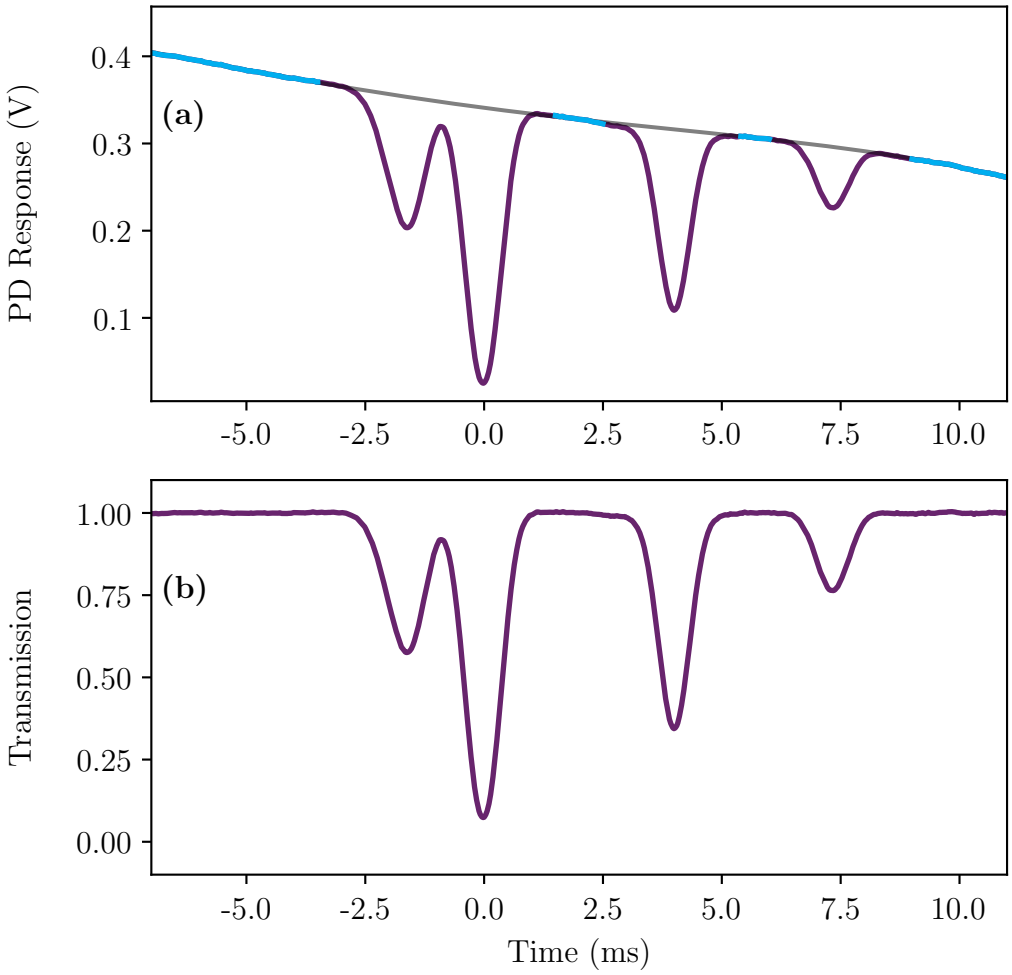

Figure A.2: **(a)** Transmission spectroscopy (purple line) of a 75 mm Rb vapour cell at room temperature, polynomial fit (grey line) is made to the off resonant sections (cyan) of the trace. **(b)** same data after division by the fitted polynomial.

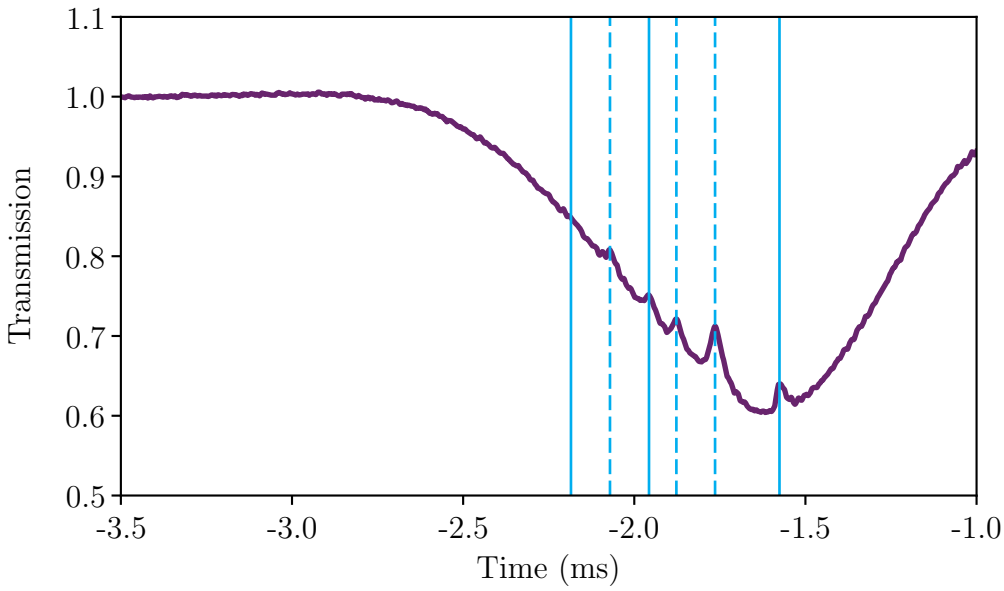

Figure A.3: A close-up of the ^{87}Rb F_g=1 ground state transmission (purple line) whilst the vapour is optically pumped by a counter-propagating beam of the same frequency. Three resonances (solids cyan lines) and three crossovers (dashed cyan lines) appear as narrow transmission peaks within the Doppler-broadened absorption dip due to the presence of the pump beam. These narrow resonances can be used as a frequency reference (see text for detail). A normalisation has been applied to the transmission axis.

A.2 Frequency calibration

The laser is scanned with a triangle profile across the Rb D2 line. Atoms with a specific velocity class will be resonant with both the 'probe' and 'pump' beams at certain laser detunings. When the frequency condition is met and the atom is driven by both beams, there is an increased transmission of the probe beam due to a depletion of the ground state by optical pumping. This is manifested by 6 sub-Doppler width transmission peaks appearing inside the Doppler-broadened absorption dip. Three of these peaks are due to the condition whereby a stationary atom is resonant with both 'probe' and 'pump' beams, the other three are called crossover resonances and occur at each of the halfway points between resonances. The crossover resonances occur when the

laser is detuned between resonances. Atoms with the correct velocity class will see a red-shifted 'probe' beam and blue-shifted 'pump' beam (or vice versa) and can be optically pumped, producing an increased transmission. In the example shown here, only 5 of the peaks are identifiable but the signature spacing of the transitions allows us to deduce where the 6th must lie. By identifying the spacings between features that are exact doubles of each other we can infer which transitions are resonances (solid cyan lines) and which are crossovers (dashed cyan lines). The known frequencies of these transitions can be found in the literature and we thus arrive at a set of points that allows us to convert from the time domain of the laser scan into the frequency domain. Similar features can be identified in all four of the ground state absorption dips to create a total of 24 frequency reference points across the laser scan range. One might assume that just 2 points are necessary to convert from one linear scale (oscilloscope time base) to another (laser frequency) but this is only true when the conversion is linear, which is typically not the case. Using the 24 reference points we can reconstruct a polynomial fit between the observed and expected locations of the sub-Doppler features. With this, we are able to compensate for the mild non-linearity present in the laser scan. Further accuracy can be obtained by using a Fabry-Pérot etalon with a convenient free spectral range (e.g. $\sim 200\,\text{MHz}$). The transmission peaks of the etalon will be evenly spaced in frequency and can be used as a ruler to linearise the time axis. A more crude frequency calibration can be performed by simply using the transmission minima of the Doppler-broadened transmission spectroscopy trace as four reference points.

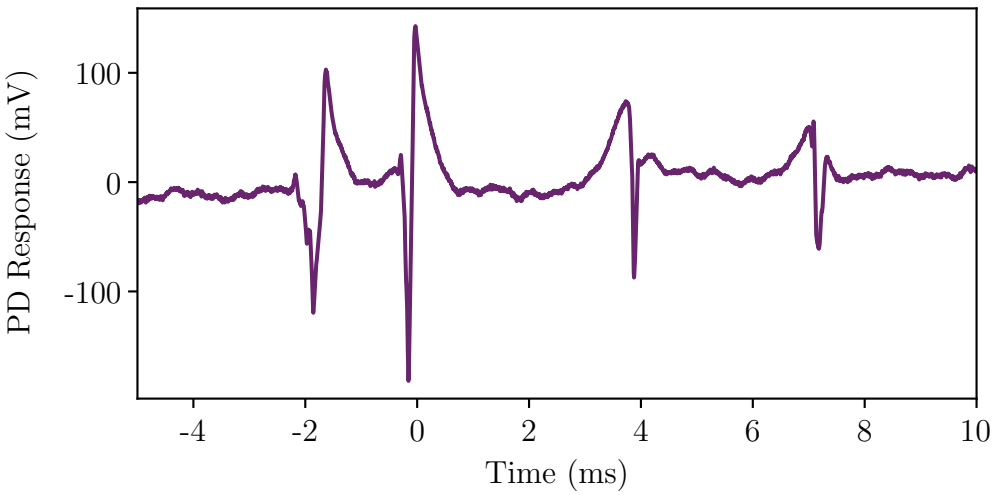

Figure A.4: A trace showing a typical laser lock signal generated via polarisation spectroscopy. Typically we lock to the ^{85}Rb $F_g = 3 \rightarrow F_e = 2,3,4$ error signal (located near 0 ms) as it is the strongest transition, thus producing a more stable lock but also inducing the most activity in the atoms when the laser is used in experiment. The dichroism in the vapour is revealed by taking the difference between two photodiode signals that each record the transmission of the vapour for the orthogonal polarisation modes of the light. The high power used for optical pumping of the medium exaggerates the sizes of the lock features. However, this causes a power broadening that mixes the hyperfine levels of the 5P state such that each ground state produces just a signal locking point. The frequency precision is compromised in favour of stability. We achieve a gradient of $3\,\mathrm{kV\,s^{-1}}$ ($\sim 4\,\mathrm{mV\,kHz^{-1}}$). We find that the D2 line lock is stable for days and is not typically the limiting factor for integration time in the experiment.

A.3 Locking

Figure A.4 shows the locking signal produced by the 780 nm atomic reference. We observe just a single zero crossing for each of the hyperfine ground states rather than the expected 12 (three hyperfine excited levels accessible from each ground state). This is due to the excess power used to optically pump the vapour, inducing a power broadening of the error signals into each other. We therefore do not resolve the separate excited state hyperfine levels, but the benefit is a larger and more stable (i.e. total time spent locked) lock.

Appendix B

776 nm laser calibration and locking

Adding a 776 nm laser allows us to perform excited state spectroscopy on, and obtain fluorescence from, the $5D_{5/2}$ state. As with the 780 nm laser, we must frequency calibrate the 776 nm laser and this is also done with an atomic reference.

Figure B.1 shows the experimental setup used to produce an EIT reference trace and also to lock the 776 nm laser. The setup is very similar to the polarisation spectroscopy lock used on the D2 line to lock the 780 nm, with a few subtle differences. We now begin with a 780 nm laser locked to the ^{85}Rb $F_g = 3 \rightarrow F_e = 2,3,4$ transition and use this to probe the heated atomic vapour. The same vapour is optically pumped with a strong circularly polarised 776 nm beam that induces a dichroism in the vapour. The dichroism is observed as an optical rotation which is detected by the differencing photodiode, similarly to the 780 nm system. The 776 nm laser is scanned over the $5P_{3/2} \rightarrow 5D_{5/2}$ resonance and although one should expect a separate error signal for each hyperfine level, the excess power used here broadens the

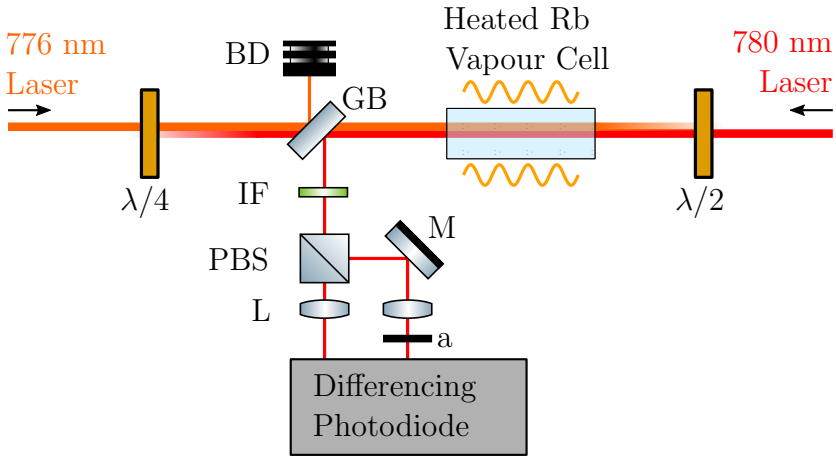

Figure B.1: BD: Beam dump, GB: Glass blank, IF: Interference filter, L: Lens, M: Mirror, PBS: Polarising beam splitter, $\lambda/2$: half-wave plate, $\lambda/4$: quarter-wave plate. Diagram showing the optical table setup used to create an error signal for locking the 776 nm laser, and to produce an atomic frequency reference for performing two-photon TIRF measurements. The cell is heated to increase the vapour pressure and therefore size of the atomic signal.

lines such that a single error signal is observed. This is the same compromise made with the 780 nm polarisation spectroscopy lock where signal strength is gained at the expense of frequency stability. However, the robustness of the lock is paramount for long integration times and hence the method is accepted. By including the beam block at 'a', we reduce the setup to transmission spectroscopy with an EIT feature created by the 780 nm beam.

When recording fluorescence spectra of the $5D_{5/2}$ state, we use an EIT reference trace as shown in figure B.2 to measure the offset detuning of the free running 776 nm laser. The familiar transmission spectroscopy trace is produced by scanning the 780 nm laser across the D2 line, but additional EIT features appear due the presence of the counter-propagating 776 nm laser. We define the detuning of the 776 nm laser, Δ_{776}, as the position of the EIT window within the ^{85}Rb F=3 ground state (at $\Delta_{780} = -1.2$ GHz), taken relative to the centre of the Doppler-broadened absorption dip. The example in

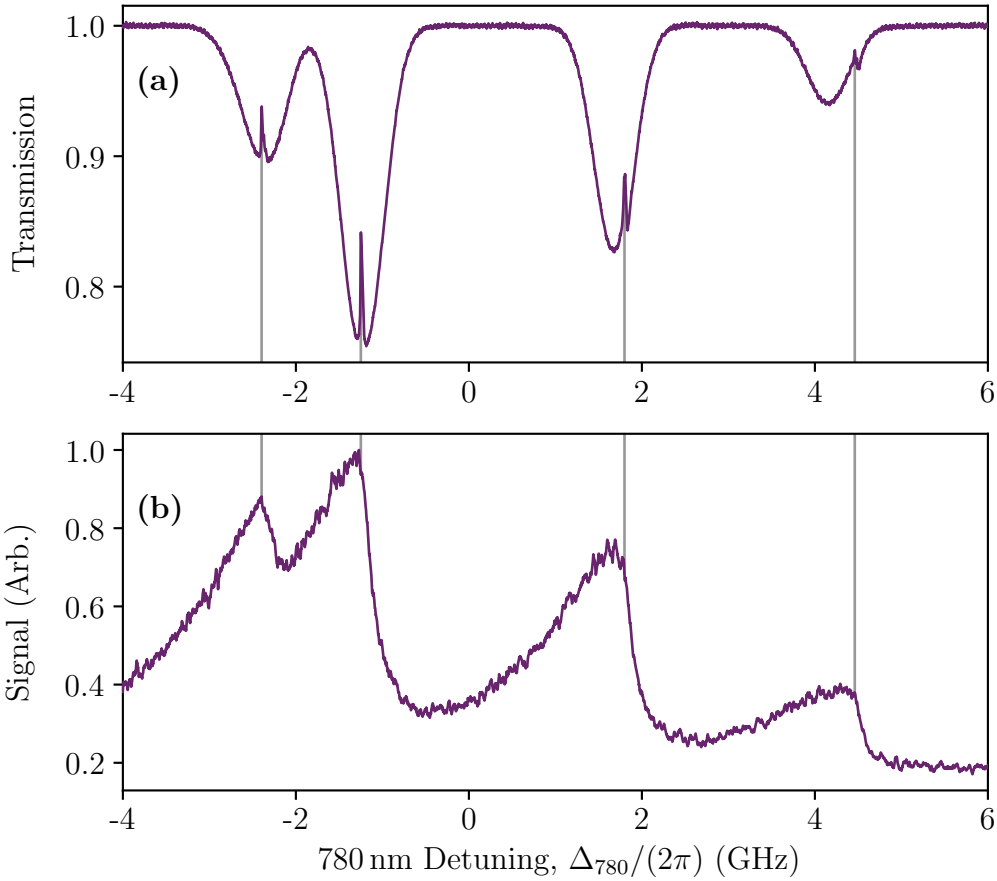

Figure B.2: **(a)** EIT reference spectrum used to measure the detuning of the 776 nm laser. **(b)** 420 nm fluorescence spectrum from two-photon TIRF setup recorded on analogue PMT.

figure B.2 shows that the EIT window is centred on the Doppler-broadened feature for the ^{85}Rb F=3 ground state, which defines $\Delta_{776} = 0\,\text{GHz}$. Note that the EIT window for each ground state transition is not centred to its respective absorption window. This is due to the hyperfine selection rules constraining the accessible F levels in the 5P and 5D manifold. Figure B.2b shows a 420 nm fluorescence spectrum from two-photon TIRF setup recorded on analogue PMT. We see a strong asymmetry of the lines which is explored further in section 4.3.

Appendix C

778 nm laser calibration

Figure C.1 shows the optical setup used to create a 778 nm frequency reference. The counter-propagating geometry creates a Doppler-free excitation of the $5D_{5/2}$ state where the separate hyperfine levels can be resolved [69]. With appropriate electronics and feedback, a stable laser lock could be realised. The level of 420 nm fluorescence coming from the cell could be used as a feedback signal for stabilising the laser frequency.

Figure C.1 shows the optical table setup used to create a frequency reference and to identify the single frequency two photon resonance at 778 nm. This wavelength makes it possible to excite directly from $5S_{1/2}$ to $5D_{5/2}$. The 778 nm beam is delivered via fiber and divided using a half-wave plate and PBS. The reflected port of the PBS is then focused through a heated 2 mm vapour cell and retro-reflected by a plane mirror. The retro-reflection is mode-matched to the first pass beam by ensuring a good coupling back up the optical fiber. This is achieved by optimal placement of the two lenses and the plane mirror inclination. The 778 nm light can drive a two photon transition from $5S_{1/2}$ to $5D_{5/2}$ and from there the atoms may decay via $6P_{3/2}$ and produce blue fluorescence which is detected by a PMT. The transmitted

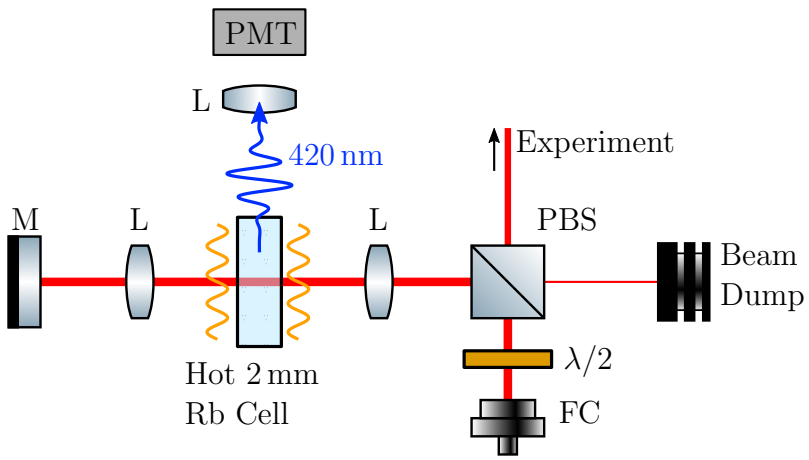

Figure C.1: FC: fiber coupler, L: lens, M: mirror, PBS: polarising beam splitter, PMT: photomultiplier tube, $\lambda/2$: half-wave plate. Table diagram of the optical system used to make a 778 nm frequency reference. The use of the optical fiber is non-essential but helps to ensure a single spatial mode of the laser and provides a mechanism for aligning the system by re-coupling the retro-reflected beam.

port of the PBS is delivered to the experiment, hence a trade-off must be made between useful power to the experiment and power used to create the atomic frequency reference. Instead, using a heated vapour cell produces a stronger fluorescence signal, requiring less laser power. In theory, the presence of the beam dump should not be necessary as no polarisation mode of the light should be able to exit through the right side of the PBS. However, it is good practice to account for the non-ideal polarisation state of the light and the non-perfect performance of the PBS. The double-pass configuration creates a Doppler-free absorption as the velocity of any given atom induces an equal redshift and blueshift on each beam. The resonance condition to excite to the $5D_{5/2}$ state is met for all atomic velocities provided the laser centre frequency is matched to the atomic transition.

Bibliography

[1] R. H. Dicke, 'The effect of collisions upon the doppler width of spectral lines', Phys. Rev. **89**, 472–473 (1953).

[2] H. B. G. Casimir and D. Polder, 'The influence of retardation on the London-van der Waals forces', Phys. Rev. **73**, 360–372 (1948).

[3] P. Siddons, C. S. Adams, C. Ge and I. G. Hughes, 'Absolute absorption on rubidium D lines: comparison between theory and experiment', J. Phys. B At. Mol. Opt. Phys. **41**, 155004 (2008).

[4] M. A. Zentile, J. Keaveney, R. S. Mathew, D. J. Whiting, C. S. Adams and I. G. Hughes, 'Optimization of atomic Faraday filters in the presence of homogeneous line broadening', J. Phys. B: At. Mol. Opt. Phys. **48**, 185001 (2015).

[5] J. Keaveney, S. A. Wrathmall, C. S. Adams and I. G. Hughes, 'Optimized ultra-narrow atomic bandpass filters via magneto-optic rotation in an unconstrained geometry', Opt. Lett. **43**, 4272 (2018).

[6] J. Keaveney, W. J. Hamlyn, C. S. Adams and I. G. Hughes, 'A single-mode external cavity diode laser using an intra-cavity atomic Faraday

filter with short-term linewidth <400 kHz and long-term stability of <1 MHz', Rev. Sci. Instrum. **87**, 095111 (2016).

[7] Y. Pétremand, C. Affolderbach, R. Straessle, M. Pellaton, D. Briand, G. Mileti and N. F. de Rooij, 'Microfabricated rubidium vapour cell with a thick glass core for small-scale atomic clock applications', J. Micromech. Microeng. **22**, 025013 (2012).

[8] M. Hasegawa, R. K. Chutani, C. Gorecki, R. Boudot, P. Dziuban, S. Galliou, N. Passilly, V. Giordano and A. Jornod, 'Microfabrication and thermal behavior of miniature cesium-vapor cells for atomic clock operations', MEMS, 712–715 (2011).

[9] J. Kitching, E. A. Donley, S. Knappe, M. Hummon, A. T. Dellis, J. Sherman, K. Srinivasan, V. A. Aksyuk, Q. Li, D. Westly, B. Roxworthy and A. Lal, 'NIST on a Chip: Realizing SI units with microfabricated alkali vapour cells', J. Phys.: Conf. Ser. **723**, 012056 (2016).

[10] V. K. Shah and R. T. Wakai, 'A compact, high performance atomic magnetometer for biomedical applications', Phys. Med. Biol. **58**, 8153–8161 (2013).

[11] E. Boto, S. S. Meyer, V. Shah, O. Alem, S. Knappe, P. Kruger, T. M. Fromhold, M. Lim, P. M. Glover, P. G. Morris, R. Bowtell, G. R. Barnes and M. J. Brookes, 'A new generation of magnetoencephalography: Room temperature measurements using optically-pumped magnetometers', Neuroimage **149**, 404–414 (2017).

[12] R. Wyllie, M. Kauer, R. T. Wakai and T. G. Walker, 'Optical magnetometer array for fetal magnetocardiography', Opt. Lett. **37**, 2247 (2012).

[13] D. Budker and M. Romalis, 'Optical magnetometry', Nat. Phys. **3**, 227–234 (2007).

[14] L.-A. Liew, S. Knappe, J. Moreland, H. Robinson, L. Hollberg and J. Kitching, 'Microfabricated alkali atom vapor cells', Appl. Phys. Lett. **84**, 2694–2696 (2004).

[15] D. Sarkisyan, D. Bloch, A. Papoyan and M. Ducloy, 'Sub-Doppler spectroscopy by sub-micron thin Cs vapour layer', Opt. Commun. **200**, 201–208 (2001).

[16] T. Peyrot, C. Beurthe, S. Coumar, M. Roulliay, K. Perronet, P. Bonnay, C. S. Adams, A. Browaeys and Y. R. P. Sortais, 'Fabrication and characterization of super-polished wedged borosilicate nano-cells', Opt. Lett. **44**, 1940 (2019).

[17] K. A. Whittaker, J. Keaveney, I. G. Hughes, A. Sargysyan, D. Sarkisyan, B. Gmeiner, V. Sandoghdar and C. S. Adams, 'Interrogation and fabrication of nm scale hot alkali vapour cells', J. Phys. Conf. Ser. **635**, 122006 (2015).

[18] A. Sipahigil, R. E. Evans, D. D. Sukachev, M. J. Burek, J. Borregaard, M. K. Bhaskar, C. T. Nguyen, J. L. Pacheco, H. A. Atikian, C. Meuwly, R. M. Camacho, F. Jelezko, E. Bielejec, H. Park, M. Lončar and M. D. Lukin, 'An integrated diamond nanophotonics platform for quantum-optical networks', Science **354**, 847–850 (2016).

[19] L.-M. Duan, M. D. Lukin, J. I. Cirac and P. Zoller, 'Long-distance quantum communication with atomic ensembles and linear optics', Nature **414**, 413–418 (2001).

[20] H. J. Kimble, 'The quantum internet', Nature **453**, 1023–1030 (2008).

[21] C. Simon, M. Afzelius, J. Appel, A. Boyer de la Giroday, S. J. Dewhurst, N. Gisin, C. Y. Hu, F. Jelezko, S. Kröll, J. H. Müller, J. Nunn, E. S. Polzik, J. G. Rarity, H. De Riedmatten, W. Rosenfeld, A. J. Shields, N. Sköld, R. M. Stevenson, R. Thew, I. A. Walmsley, M. C. Weber, H. Weinfurter, J. Wrachtrup and R. J. Young, 'Quantum memories', Eur. Phys. J. D **58**, 1–22 (2010).

[22] K. F. Reim, J. Nunn, V. O. Lorenz, B. J. Sussman, K. C. Lee, N. K. Langford, D. Jaksch and I. A. Walmsley, 'Towards high-speed optical quantum memories', Nat. Photonics **4**, 218–221 (2010).

[23] R. M. Camacho, P. K. Vudyasetu and J. C. Howell, 'Four-wave-mixing stopped light in hot atomic rubidium vapour', Nat. Photonics **3**, 103–106 (2009).

[24] A. I. Lvovsky, B. C. Sanders and W. Tittel, 'Optical quantum memory', Nat. Photonics **3**, 706–714 (2009).

[25] D. F. Phillips, A. Fleischhauer, A. Mair, R. L. Walsworth and M. D. Lukin, 'Storage of light in atomic vapor', Phys. Rev. Lett. **86**, 783–786 (2001).

[26] R. A. Nyman, S. Scheel and E. A. Hinds, 'Prospects for using integrated atom-photon junctions for quantum information processing', Quantum Inf. Process. (2011).

[27] D. J. Saunders, J. H. D. Munns, T. F. M. Champion, C. Qiu, K. T. Kaczmarek, E. Poem, P. M. Ledingham, I. A. Walmsley and J. Nunn, 'Cavity-Enhanced Room-Temperature Broadband Raman Memory', Phys. Rev. Lett. **116**, 090501 (2016).

[28] K. Hammerer, A. S. Sørensen and E. S. Polzik, 'Quantum interface between light and atomic ensembles', Rev. Mod. Phys. **82**, 1041–1093 (2010).

[29] S. Welte, B. Hacker, S. Daiss, S. Ritter and G. Rempe, 'Photon-Mediated Quantum Gate between Two Neutral Atoms in an Optical Cavity', Phys. Rev. X **8**, 011018 (2018).

[30] H. Busche, P. Huillery, S. W. Ball, T. Ilieva, M. P. A. Jones and C. S. Adams, 'Contactless nonlinear optics mediated by long-range Rydberg interactions', Nat. Phys. **13**, 655–658 (2017).

[31] A. MacRae, T. Brannan, R. Achal and A. I. Lvovsky, 'Tomography of a High-Purity Narrowband Photon from a Transient Atomic Collective Excitation', Phys. Rev. Lett. **109**, 033601 (2012).

[32] C. W. Chou, S. V. Polyakov, A. Kuzmich and H. J. Kimble, 'Single-Photon Generation from Stored Excitation in an Atomic Ensemble', Phys. Rev. Lett. **92**, 213601 (2004).

[33] R. Bettles, *Cooperative Interactions in Lattices of Atomic Dipoles*, Springer Theses (Springer International Publishing, Cham, 2017).

[34] R. J. Bettles, S. A. Gardiner and C. S. Adams, 'Cooperative ordering in lattices of interacting two-level dipoles', Phys. Rev. A **92**, 063822 (2015).

[35] R. J. Bettles, S. A. Gardiner and C. S. Adams, 'Enhanced Optical Cross Section via Collective Coupling of Atomic Dipoles in a 2D Array', Phys. Rev. Lett. **116**, 103602 (2016).

[36] D. Sarkisyan, T. Becker, A. Papoyan, P. Thoumany and H. Walther, 'Sub-Doppler fluorescence on the atomic D 2 line of a submicron rubidium-vapor layer', Appl. Phys. B **76**, 625–631 (2003).

[37] J. Keaveney, A. Sargsyan, U. Krohn, I. G. Hughes, D. Sarkisyan and C. S. Adams, 'Cooperative Lamb Shift in an Atomic Vapor Layer of Nanometer Thickness', Phys. Rev. Lett. **108**, 173601 (2012).

[38] J. Keaveney, I. G. Hughes, A. Sargsyan, D. Sarkisyan and C. S. Adams, 'Maximal Refraction and Superluminal Propagation in a Gaseous Nanolayer', Phys. Rev. Lett. **109**, 233001 (2012).

[39] F. Ripka, H. Kübler, R. Löw and T. Pfau, 'A room-temperature single-photon source based on strongly interacting Rydberg atoms', Science **362**, 446–449 (2018).

[40] S. Briaudeau, D. Bloch and M. Ducloy, 'Detection of slow atoms in laser spectroscopy of a thin vapor film', Europhys. Lett. **35**, 337–342 (1996).

[41] T. Peyrot, N. Šibalić, Y. R. P. Sortais, A. Browaeys, A. Sargsyan, D. Sarkisyan, I. G. Hughes and C. S. Adams, 'Measurement of the atom-surface van der Waals interaction by transmission spectroscopy in a wedged nanocell', Phys. Rev. A **100**, 022503 (2019).

[42] K. A. Whittaker, J. Keaveney, I. G. Hughes, A. Sargsyan, D. Sarkisyan and C. S. Adams, 'Optical Response of Gas-Phase Atoms at Less than $\lambda/80$ from a Dielectric Surface', Phys. Rev. Lett. **112**, 253201 (2014).

[43] M. Fichet, G. Dutier, A. Yarovitsky, P. Todorov, I. Hamdi, I. Maurin, S. Saltiel, D. Sarkisyan, M.-P. Gorza, D. Bloch and M. Ducloy, 'Exploring the van der Waals atom-surface attraction in the nanometric range', Europhys. Lett. **77**, 54001 (2007).

[44] E. G. Lima, M. Chevrollier, O. Di Lorenzo, P. C. Segundo and M. Oriá, 'Long-range atom-surface bound states', Phys. Rev. **62**, 013410 (2000).

[45] E. Vetsch, D. Reitz, G. Sagué, R. Schmidt, S. T. Dawkins and A. Rauschenbeutel, 'Optical Interface Created by Laser-Cooled Atoms Trapped in the Evanescent Field Surrounding an Optical Nanofiber', Phys. Rev. Lett. **104**, 203603 (2010).

[46] F. Le Kien, V. I. Balykin and K. Hakuta, 'Atom trap and waveguide using a two-color evanescent light field around a subwavelength-diameter optical fiber', Phys. Rev. A **70**, 063403 (2004).

[47] F. Le Kien, V. I. Balykin and K. Hakuta, 'Scattering of an evanescent light field by a single cesium atom near a nanofiber', Phys. Rev. A **73**, 013819 (2006).

[48] R. Garcia-Fernandez, W. Alt, F. Bruse, C. Dan, K. Karapetyan, O. Rehband, A. Stiebeiner, U. Wiedemann, D. Meschede and A. Rauschenbeutel, 'Optical nanofibers and spectroscopy', Appl. Phys. B **105**, 3–15 (2011).

[49] G. Epple, K. S. Kleinbach, T. G. Euser, N. Y. Joly, T. Pfau, P. S. J. Russell and R. Löw, 'Rydberg atoms in hollow-core photonic crystal fibres', Nat. Commun. **5**, 4132 (2014).

[50] R. Zektzer, E. Talker, Y. Barash, N. Mazurski and U. Levy, 'Chiral light–matter interactions in hot vapor-cladded waveguides', Optica **6**, 15 (2019).

[51] R. Ritter, N. Gruhler, W. Pernice, H. Kübler, T. Pfau and R. Löw, 'Atomic vapor spectroscopy in integrated photonic structures', Appl. Phys. Lett. **107**, 041101 (2015).

[52] R. Ritter, N. Gruhler, W. H. Pernice, H. Kübler, T. Pfau and R. Löw, 'Coupling thermal atomic vapor to an integrated ring resonator', New J. Phys. **18**, 1–5 (2016).

[53] R. Ritter, N. Gruhler, H. Dobbertin, H. Kübler, S. Scheel, W. Pernice, T. Pfau and R. Löw, 'Coupling Thermal Atomic Vapor to Slot Waveguides', Phys. Rev. X **8**, 021032 (2018).

[54] L. Stern, R. Zektzer, N. Mazurski and U. Levy, 'Enhanced light-vapor interactions and all optical switching in a chip scale micro-ring resonator coupled with atomic vapor', Laser Photon. Rev. **10**, 1016–1022 (2016).

[55] S. Liron, D. G. Bopp, S. A. Schima, V. N. Maurice and J. E. Kitching, 'Chip-scale atomic diffractive optical elements', Nat. Commun. **10**, 3156 (2019).

[56] U. Volz and H. Schmoranzer, 'Precision lifetime measurements on alkali atoms and on helium by beam–gas–laser spectroscopy', Phys. Scr. **T65**, 48–56 (1996).

[57] J. Keaveney, *Collective Atom–Light Interactions in Dense Atomic Vapours*, Springer Theses (Springer International Publishing, Cham, 2014).

[58] C. B. Alcock, V. P. Itkin and M. K. Horrigan, 'Vapour Pressure Equations for the Metallic Elements: 298–2500K', Can. Metall. Q. **23**, 309–313 (1984).

[59] J. E. Lennard-Jones, 'Processes of adsorption and diffusion on solid surfaces', Trans. Faraday Soc. **28**, 333 (1932).

[60] G. Comsa and R. David, 'Dynamical parameters of desorbing molecules', Surf. Sci. Rep **5**, 145–198 (1985).

[61] D. Grischkowsky, 'Angular and velocity distribution of desorbed sodium atoms', Appl. Phys. Lett. **36**, 711–713 (1980).

[62] U. Leuthäusser, 'Kinetic theory of desorption: Energy and angular distributions', Z. Phys. B **50**, 65–69 (1983).

[63] A. D. Slepkov, A. R. Bhagwat, V. Venkataraman, P. Londero and A. L. Gaeta, 'Diffusion and Redistribution of Rubidium in Hollow-Core Photonic Bandgap Fibers', in Conf. lasers electro-optics (May 2013), p. IMC2.

[64] J. Ma, A. Kishinevski, Y.-Y. Jau, C. Reuter and W. Happer, 'Modification of glass cell walls by rubidium vapor', Phys. Rev. A **79**, 042905 (2009).

[65] K. Kitagami, K. Hosumi, K. Goto and A. Hatakeyama, 'Quantitative measurements of light-induced desorption of rubidium atoms from quartz substrates', Phys. Rev. A **85**, 062901 (2012).

[66] E. Talker, P. Arora, M. Dikopoltsev, U. Levy and U. Levy, 'Realization of optical isolator at room temperature in miniaturized vapor cell using light induced atomic desorption', in Conf. lasers electro-optics (May 2019), JTu2A.39.

[67] C. Foot, *Atomic physics* (Oxford University Press, 2005).

[68] M. H. Anderson, J. R. Ensher, M. R. Matthews, C. E. Wieman and E. A. Cornell, 'Observation of Bose-Einstein Condensation in a Dilute Atomic Vapor', Science **269**, 198–201 (1995).

[69] V. Jacques, B. Hingant, A. Allafort, M. Pigeard and J. F. Roch, 'Nonlinear spectroscopy of rubidium: an undergraduate experiment', Eur. J. Phys. **30**, 921–934 (2009).

[70] F. Nez, F. Biraben, R. Felder and Y. Millerioux, 'Optical frequency determination of the hyperfine components of the two-photon transitions in rubidium', Opt. Commun. **102**, 432–438 (1993).

[71] D. Sheng, A. Pérez Galván and L. A. Orozco, 'Lifetime measurements of the 5d states of rubidium', Phys. Rev. A **78**, 062506 (2008).

[72] A. R. Bhagwat and A. L. Gaeta, 'Nonlinear optics in hollow-core photonic bandgap fibers', Opt. Express **16**, 5035 (2008).

[73] F. Le Kien and A. Rauschenbeutel, 'Nanofiber-mediated chiral radiative coupling between two atoms', Phys. Rev. A **95**, 023838 (2017).

[74] K. F. Zhao and Z. Wu, 'Evanescent wave magnetometer', Appl. Phys. Lett. **89**, 261113 (2006).

[75] I. K. Kominis, T. W. Kornack, J. C. Allred and M. V. Romalis, 'A subfemtotesla multichannel atomic magnetometer', Nature **422**, 596–599 (2003).

[76] S. Knappe, O. Alem, D. Sheng and J. Kitching, 'Microfabricated Optically-Pumped Magnetometers for Biomagnetic Applications', J. Phys. Conf. Ser. **723**, 012055 (2016).

[77] T. Peyrot, Y. R. P. Sortais, A. Browaeys, A. Sargsyan, D. Sarkisyan, J. Keaveney, I. G. Hughes and C. S. Adams, 'Collective Lamb Shift of a Nanoscale Atomic Vapor Layer within a Sapphire Cavity', Phys. Rev. Lett. **120**, 243401 (2018).

[78] J. H. Xu, A. Gozzini, F. Mango, G. Alzetta and R. A. Bernheim, 'Photoatomic effect: Light-induced ejection of Na and Na_2 from polydimethylsiloxane surfaces', Phys. Rev. A **54**, 3146–3150 (1996).

[79] N. Bouras, M. Madjoubi, M. Kolli, S. Benterki and M. Hamidouche, 'Thermal and mechanical characterization of borosilicate glass', Phys. Procedia **2**, 1135–1140 (2009).

[80] T. A. Hahn, R. K. Kirby, H. C. Wolfe, M. G. Graham and H. E. Hagy, 'Thermal Expansion of Fused Silica from 80 to 1000 K - Standard Reference Material 739', in Aip conf. proc. Vol. 3, 1 (July 2010), pp. 13–24.

[81] J. Petersen, J. Volz and A. Rauschenbeutel, 'Chiral nanophotonic waveguide interface based on spin-orbit interaction of light', Science **346**, 67–71 (2014).

[82] D. Jukic, A. Moqanaki, P. Walther, A. Szameit, T. Pohl and J. B. Götte, 'Trapping atoms in the evanescent field of laser written wave guides', http://arxiv.org/abs/1605.00332 (2016).

[83] L. Stern, B. Desiatov, I. Goykhman and U. Levy, 'Nanoscale light–matter interactions in atomic cladding waveguides', Nat. Commun. **4**, 1548 (2013).

[84] K. P. Nayak, P. N. Melentiev, M. Morinaga, F. L. Kien, V. I. Balykin and K. Hakuta, 'Optical nanofiber as an efficient tool for manipulating and probing atomic Fluorescence', Opt. Express **15**, 5431 (2007).

[85] R. J. Bettles, J. Minář, C. S. Adams, I. Lesanovsky and B. Olmos, 'Topological properties of a dense atomic lattice gas', Phys. Rev. A **96**, 041603 (2017).

[86] M. Greiner and S. Fölling, 'Optical lattices', Nature **453**, 736–738 (2008).

[87] D. Meschede and A. Rauschenbeutel, 'Manipulating Single Atoms', Adv. At. Mol. Opt. Phys. **53**, 75–104 (2006).

[88] S. Weber, S. D. Léséleuc, V. Lienhard, D. Barredo, T. Lahaye, A. Browaeys and H. P. Büchler, 'Topologically protected edge states in small Rydberg systems', Quantum Sci. Technol. **3**, 044001 (2018).

[89] D. Barredo, S. de Léséleuc, V. Lienhard, T. Lahaye and A. Browaeys, 'An atom-by-atom assembler of defect-free arbitrary two-dimensional atomic arrays', Science **354**, 1021–1023 (2016).

[90] D. Barredo, V. Lienhard, S. de Léséleuc, T. Lahaye and A. Browaeys, 'Synthetic three-dimensional atomic structures assembled atom by atom', Nature **561**, 79–82 (2018).

[91] F. Nogrette, H. Labuhn, S. Ravets, D. Barredo, L. Béguin, A. Vernier, T. Lahaye and A. Browaeys, 'Single-atom trapping in holographic 2D arrays of microtraps with arbitrary geometries', Phys. Rev. X **4**, 021034 (2014).

[92] J. Camparo, 'The rubidium atomic clock and basic research', Phys. Today **60**, 33–39 (2007).

[93] V. Maurice, J. Rutkowski, E. Kroemer, S. Bargiel, N. Passilly, R. Boudot, C. Gorecki, L. Mauri and M. Moraja, 'Microfabricated vapor cells filled with a cesium dispensing paste for miniature atomic clocks', Appl. Phys. Lett. **110**, 164103 (2017).

[94] J. Javanainen, J. Ruostekoski, Y. Li and S. M. Yoo, 'Shifts of a resonance line in a dense atomic sample', Phys. Rev. Lett. **112**, 113603 (2014).

[95] S. J. Roof, K. J. Kemp, M. D. Havey and I. M. Sokolov, 'Observation of Single-Photon Superradiance and the Cooperative Lamb Shift in an Extended Sample of Cold Atoms', Phys. Rev. Lett. **117**, 073003 (2016).

[96] T. G. Tiecke, J. D. Thompson, N. P. De Leon, L. R. Liu, V. Vuletić and M. D. Lukin, 'Nanophotonic quantum phase switch with a single atom', Nature **508**, 241–244 (2014).

[97] S. P. Yu, J. D. Hood, J. A. Muniz, M. J. Martin, R. Norte, C. L. Hung, S. M. Meenehan, J. D. Cohen, O. Painter and H. J. Kimble, 'Nanowire photonic crystal waveguides for single-atom trapping and strong light-matter interactions', Appl. Phys. Lett. **104**, 111103 (2014).

[98] D. Axelrod, T. P. Burghardt and N. L. Thompson, 'Total Internal Reflection Fluorescence', Annu. Rev. Biophys. Bioeng. **13**, 247–268 (1984).

[99] G. S. Agarwal, A. C. Brown, L. M. Narducci and G. Vetri, 'Collective atomic effects in resonance fluorescence', Phys. Rev. A **15**, 1613–1624 (1977).

[100] I. H. Malitson, 'Interspecimen Comparison of the Refractive Index of Fused Silica', J. Opt. Soc. Am. **55**, 1205 (1965).

[101] J. Keaveney, C. S. Adams and I. G. Hughes, 'ElecSus: Extension to arbitrary geometry magneto-optics', Comput. Phys. Commun. **224**, 311–324 (2018).

[102] S. Scheel, S. Y. Buhmann, C. Clausen and P. Schneeweiss, 'Directional spontaneous emission and lateral Casimir-Polder force on an atom close to a nanofiber', Phys. Rev. A **92**, 043819 (2015).

[103] C. I. Sukenik, M. G. Boshier, D. Cho, V. Sandoghdar and E. A. Hinds, 'Measurement of the Casimir-Polder force', Phys. Rev. Lett. **70**, 560–563 (1993).

[104] E. A. Hinds and V. Sandoghdar, 'Cavity QED level shifts of simple atoms', Phys. Rev. A **43**, 398–403 (1991).

[105] W. Van Willigen, 'Angular distribution of hydrogen molecules desorbed from metal surfaces', Phys. Lett. A **28**, 80–81 (1968).

[106] I. G. Hughes, 'Velocity selection in a Doppler-broadened ensemble of atoms interacting with a monochromatic laser beam', J. Mod. Opt. **65**, 640–647 (2018).

[107] H. Failache, S. Saltiel, M. Fichet, D. Bloch and M. Ducloy, 'Resonant van der Waals Repulsion between Excited Cs Atoms and Sapphire Surface', Phys. Rev. Lett. **83**, 5467–5470 (1999).

[108] L. Weller, K. S. Kleinbach, M. A. Zentile, S. Knappe, I. G. Hughes and C. S. Adams, 'An optical isolator using an atomic vapor in the hyperfine Paschen-Back regime', Opt. Lett. **37**, 3405 (2012).

[109] M. A. Zentile, D. J. Whiting, J. Keaveney, C. S. Adams and I. G. Hughes, 'Atomic Faraday filter with equivalent noise bandwidth less than 1 GHz', Opt. Lett. **40**, 2000 (2015).

[110] R. Hanbury Brown and R. Q. Twiss, 'A Test of a New Type of Stellar Interferometer on Sirius', Nature **178**, 1046–1048 (1956).

[111] G. Scarcelli, V. Berardi and Y. Shih, 'Can Two-Photon Correlation of Chaotic Light Be Considered as Correlation of Intensity Fluctuations?', Phys. Rev. Lett. **96**, 063602 (2006).

[112] L. A. Ngah, O. Alibart, L. Labonté, V. D'Auria and S. Tanzilli, 'Ultra-fast heralded single photon source based on telecom technology', Laser Photon. Rev. **9**, L1–L5 (2015).

[113] C. Jurczak, K. Sengstock, R. Kaiser, N. Vansteenkiste, C. Westbrook and A. Aspect, 'Observation of intensity correlations in the fluorescence from laser cooled atoms', Opt. Commun. **115**, 480–484 (1995).

[114] S. Bali, D. Hoffmann, J. Simán and T. Walker, 'Measurements of intensity correlations of scattered light from laser-cooled atoms', Phys. Rev. A **53**, 3469–3472 (1996).

[115] R. Stites, M. Beeler, L. Feeney, S. Kim and S. Bali, 'Sensitive measurement of radiation trapping in cold-atom clouds by intensity correlation detection', Opt. Lett. **29**, 2713 (2004).

[116] K. Nakayama, Y. Yoshikawa, H. Matsumoto, Y. Torii and T. Kuga, 'Precise intensity correlation measurement for atomic resonance fluorescence from optical molasses', Opt. Express **18**, 6604 (2010).

[117] J. Kong, R. Jiménez-Martínez, C. Troullinou, V. G. Lucivero and M. W. Mitchell, 'Measurement-induced nonlocal entanglement in a hot, strongly-interacting atomic system', http://arxiv.org/abs/1804.07818 (2018).

[118] D. J. Whiting, N. Šibalić, J. Keaveney, C. S. Adams and I. G. Hughes, 'Single-Photon Interference due to Motion in an Atomic Collective Excitation', Phys. Rev. Lett. **118**, 253601 (2017).

[119] A. Dussaux, T. Passerat de Silans, W. Guerin, O. Alibart, S. Tanzilli, F. Vakili and R. Kaiser, 'Temporal intensity correlation of light scattered by a hot atomic vapor', Phys. Rev. A **93**, 043826 (2016).

[120] M. M. Müller, A. Kölle, R. Löw, T. Pfau, T. Calarco and S. Montangero, 'Room-temperature Rydberg single-photon source', Phys. Rev. A **87**, 053412 (2013).

[121] H. J. Kimble, M. Dagenais and L. Mandel, 'Photon antibunching in resonance fluorescence', Phys. Rev. Lett. **39**, 691–695 (1977).

[122] N. Piro, F. Rohde, C. Schuck, M. Almendros, J. Huwer, J. Ghosh, A. Haase, M. Hennrich, F. Dubin and J. Eschner, 'Heralded single-photon absorption by a single atom', Nat. Phys. **7**, 17–20 (2011).

[123] J. D. Cohen, S. M. Meenehan, G. S. MacCabe, S. Gröblacher, A. H. Safavi-Naeini, F. Marsili, M. D. Shaw and O. Painter, 'Phonon counting and intensity interferometry of a nanomechanical resonator', Nature **520**, 522–525 (2015).

[124] M. Fox, *Quantum Optics: An Introduction* (Oxford University Press, New York, 2006).

[125] R. Loudon, *The quantum theory of light* (Clarendon Press, 1973).

[126] J. Mika, L. Podhora, L. Lachman, P. Obšil, J. Hloušek, M. Ježek, R. Filip and L. Slodička, 'Generation of ideal thermal light in warm atomic vapor', New J. Phys. **20**, 093002 (2018).

[127] M. Gross and S. Haroche, 'Superradiance: An essay on the theory of collective spontaneous emission', Phys. Rep. **93**, 301–396 (1982).

[128] C. Skornia, J. von Zanthier, G. S. Agarwal, E. Werner and H. Walther, 'Nonclassical interference effects in the radiation from coherently driven uncorrelated atoms', Phys. Rev. A **64**, 063801 (2001).

[129] V. Marshall, 'Experimental studies of the D2 line of 87 Rb vapour at 1.5 Tesla', Durham e-Theses (2017).

[130] J. Park, T. Jeong and H. S. Moon, 'Temporal intensity correlation of bunched light from a warm atomic vapor with a ladder-type two-photon transition', Sci. Rep. **8**, 10981 (2018).

[131] D. Bloch and M. Ducloy, 'Atom-wall interaction', in *Advances in atomic, molecular and optical physics*, Vol. 50 (Academic Press, 2005), pp. 91–154.

[132] U. D. Jentschura, M. Janke and M. Dekieviet, 'Theory of noncontact friction for atom-surface interactions', Phys. Rev. A **94** (2016).

[133] J. Naber, S. Machluf, L. Torralbo-Campo, M. L. Soudijn, N. J. van Druten, H. B. v. L. van den Heuvell and R. J. C. Spreeuw, 'Adsorbate dynamics on a silica-coated gold surface measured by Rydberg Stark spectroscopy', J. Phys. B: At. Mol. Opt. Phys. **49**, 094005 (2016).

[134] I. N. Abramova, E. B. Aleksandrov, A. M. Bonch-Bruevich and V. V. Khromov, 'Photostimulated desorption of metal atoms from surfaces of transparent insulators', JETP Lett. **39**, 203 (1984).

[135] A. Gozzini, F. Mango, J. H. Xu, G. Alzetta, F. Maccarrone and R. A. Bernheim, 'Light-induced ejection of alkali atoms in polysiloxane coated cells', Il Nuovo Cimento D **15**, 709–722 (1993).

[136] M. Meucci, E. Mariotti, P. Bicchi, C. Marinelli and L. Moi, 'Light-induced atom desorption', EPL **25**, 639–643 (1994).

[137] T. E. Madey, B. V. Yakshinskiy, V. N. Ageev and R. E. Johnson, 'Desorption of alkali atoms and ions from oxide surfaces: Relevance to origins of Na and K in atmospheres of Mercury and the Moon', J. Geophys. Res. Planets **103**, 5873–5887 (1998).

[138] L. Torralbo-Campo, G. D. Bruce, G. Smirne and D. Cassettari, 'Light-induced atomic desorption in a compact system for ultracold atoms', Sci. Rep. **5**, 1–10 (2015).

[139] D. S. Barker, E. B. Norrgard, J. Scherschligt, J. A. Fedchak and S. Eckel, 'Light-induced atomic desorption of lithium', Phys. Rev. A **98**, 043412 (2018).

[140] C. Klempt, T. van Zoest, T. Henninger, O. Topic, E. Rasel, W. Ertmer and J. Arlt, 'Ultraviolet light-induced atom desorption for large rubidium and potassium magneto-optical traps', Phys. Rev. A **73**, 013410 (2006).

[141] A. Bogi, A. Burchianti, C. de Mauro, S. Gozzini, A. Lucchesini, C. Marinelli, E. Mariotti, L. Marmugi and L. Moi, 'Atomic sources controlled by light: main features and applications', in 16th international school on quantum electronics: laser physics and applications, Vol. 7747 (Oct. 2011).

[142] P. A. Petrov, A. S. Pazgalev, M. A. Burkova and T. A. Vartanyan, 'Photodesorption of rubidium atoms from a sapphire surface', Opt. and Spectrosc. **123**, 574–577 (2017).

[143] F. Schuller, G. Nienhuis and M. Ducloy, 'Selective reflection from an atomic vapor in a pump-probe scheme', Phys. Rev. A **43**, 443–454 (1991).

[144] M. Ducloy and M. Fichet, 'General theory of frequency modulated selective reflection. Influence of atom surface interactions', J. Phys. II **1**, 1429–1446 (1991).

[145] B. Zambon and G. Nienhuis, 'Reflection and transmission of light by thin vapor layers', Opt. Commun. **143**, 308–314 (1997).

[146] G. Dutier, S. Saltiel, D. Bloch and M. Ducloy, 'Revisiting optical spectroscopy in a thin vapor cell: mixing of reflection and transmission as a Fabry–Perot microcavity effect', J. Opt. Soc. Am. B **20**, 793 (2003).

[147] K. R. Rusimova, D. Slavov, F. Pradaux-Caggiano, J. T. Collins, S. N. Gordeev, D. R. Carbery, W. J. Wadsworth, P. J. Mosley and V. K. Valev, 'Atomic dispensers for thermoplasmonic control of alkali vapor pressure in quantum optical applications', Nat. Commun. **10**, 2328 (2019).